COMPLEX HAMILTONIAN DYNAMICS

Tassos BOUNTIS

Department of Mathematics and Center for Research and Applications of Nonlinear

Systems (CRANS),

University of Patras, GR–26500, Rion, Patras, Greece

Lecture 1:

Introduction to Hamiltonian Dynamics: Stability and Chaos

Workshop and Latin–American School on "Foundations of Complexity"

Rio de Janeiro, Brasil, October 4–30, 2015

Contents

Dynamical Systems and Stability of Equilibrium Points

Dynamical systems in continuous time are described by systems of Ordinary Differential Equations (ODEs), in n real dependent variables $(x_k(t), k = 1, 2, \ldots, n$, which constitute a state $\vec{x}(t) = (x_1(t), \ldots, x_n(t))$ in the phase space of the system $D \subseteq \mathbb{R}^n$ and are functions of the single independent variable of the problem: the time $t \in \mathbb{R}$. Their dynamics is described by the system of first order ODEs

$$\frac{dx_k}{dt} = f_k(x_1, x_2, \ldots, x_n), \quad k = 1, 2, \ldots, n \tag{1}$$

Since the f_k do not explicitly depend on t the system is called autonomous. The functions f_k are defined everywhere in D and are assumed analytic in all their variables, meaning that they can be expressed as convergent series expansions in the x_k (with non-zero radius of convergence) near one of their equilibrium (or fixed) points, located at the origin of phase space $\vec{0} = (0, \ldots, 0) \in D$, where

$$f_k(\vec{0}) = 0, \quad k = 1, 2, \ldots, n. \tag{2}$$

What can we say now about the solutions of these equations in a small neighborhood of the equilibrium point (2), where the series expansions of the f_k converge? Is the motion "regular" or "predictable" there? This is the question of stability of motion first studied systematically by the great Russian mathematician A. M. Lyapunov, more than 110 years ago.

The first and simplest notion of stability is called asymptotic stability and refers to the case where all solutions $x_k(t)$ of (1), starting near the origin, tend to 0 as $t \to \infty$. A less restrictive situation arises when we can prove that for every $0 < \varepsilon < \varepsilon_0$, no matter how small, all solutions starting at $t = t_0$ within a neighborhood of the origin $K(\varepsilon) \subseteq B(\varepsilon)$, where $B(\varepsilon)$ is a "ball" of radius ε around the origin, remain inside $B(\varepsilon)$ for all $t \geq t_0$.

This so-called neutral or conditional stability will be of great importance to us, as it frequently occurs in conservative dynamical systems, among which are the Hamiltonian systems. These conserve phase space volume and hence cannot come to a complete rest at any value of t, finite or infinite. As we shall discuss later, conditional stability characterizes precisely the systems for which Lyapunov could prove the existence of families of periodic solutions around the origin.

To discuss the question of stability of the motion near an equilibrium point, we need to know something about the behavior of the solutions of the linearized equations about that point. Thus one might try to compare these solutions to an exponential function of time, with the purpose of identifying a particular exponent, which we call today the Lyapunov characteristic exponent (LCE).

Let us identify the meaning of these exponents for our problem. Indeed, they are directly related to the eigenvalues of the $n \times n$ matrix $J = (p_{jk}), j, k = 1, 2, \ldots, n$, obtained as the roots of the characteristic equation

$$\det(J - \lambda I_n) = 0, \tag{3}$$

$\lambda_1, \lambda_2, \ldots, \lambda_n, I_n$ being the $n \times n$ identity matrix.

In modern terminology, therefore, consider a dynamical system (1), with an equilibrium point at $(0, 0, \ldots, 0)$ and a constant Jacobian matrix

$$J_{k,j} = p_{kj} = \frac{\partial f_k}{\partial x_j}(0, \ldots, 0) / \ j, k = 1, 2, \ldots, n, \tag{4}$$

The above analysis translates to the following well-known result:

Theorem (see p. 181 Hirsch and Smale, 1974) If all eigenvalues of the matrix J have negative real part less than $-c$, $c > 0$, there is a compact neighborhood U of the origin, such that, for all $(x_1(0), x_2(0), \ldots, x_n(0)) \in U$, all solutions $x_k(t) \to 0$, as $t \to \infty$. Furthermore, one can show that this approach to the fixed point is exponential: Indeed, if we denote by $|\cdot|$ the Euclidean norm in $\mathbb{R}^n$ and define $\vec{x}(t) = (x_1(t), x_2(t), \ldots, x_n(t))$, it can be proved that for all $\vec{x}(0)$ in U, $|\vec{x}(t)| \leq |\vec{x}(0)|e^{-ct}$, and $|\vec{x}(t)|$ is in U for all $t \geq 0$.

Lyapunov paid particular attention to the case where one (or more) of the eigenvalues of the linearized equations have zero real part. This was the beginning of what we now call bifurcation theory, as it constitutes the turning point between stability of the fixed point (all eigenvalues have negative real part) and instability, where at least one eigenvalue has positive real part.

This theory can be found, not only in Lyapunov's treatise "Stability of Motion" but also in a many textbooks on the qualitative theory of ODEs (Hirsch, Smale and Devaney, 2004, Perko, 1995 and Wiggins, 1990). One more result of Lyapunov's theory, concerning simple periodic solutions of Hamiltonian systems, will be described in the next section.

Hamiltonian Systems of N=1 and 2 Degrees of Freedom

Let us now apply the above theory to the case of Hamiltonian dynamical systems of N degrees of freedom (dof), where $n = 2N$ and the equations of motion are

$$\frac{dq_k}{dt} = \frac{\partial H}{\partial p_k}, \ \ \frac{dp_k}{dt} = -\frac{\partial H}{\partial q_k}, \ \ k = 1, 2, \ldots, N, \tag{5}$$

where $q_k(t)$, $p_k(t)$, $k = 1, 2, \ldots, 2N$ are the position and momentum coordinates and H is the Hamiltonian. If H does not explicitly depend on t, it is a first integral (or constant of the motion), whose value equals the total energy of the system E.

We now assume that our Hamiltonian can be expanded in power series as a sum of homogeneous polynomials H_m of degree $m \geq 2$

$$H = H_2(q_1, \ldots, q_N, p_1, \ldots, p_N) + H_3(q_1, \ldots, q_N, p_1, \ldots, p_N) + \ldots = E, \tag{6}$$

so that the origin is always an equilibrium point of the system. $H(q_k(t), p_k(t)) = E$ thus defines the so-called constant energy surface, on which our Hamiltonian dynamics evolves.

If the linear equations resulting from (5) and (6), with $H_m = 0$ for all $m > 2$, yield a matrix, whose eigenvalues all occur in conjugate imaginary pairs, $\pm i\omega_k$, these provide the frequencies of the normal mode oscillations of the linearized system.

We can then change to normal mode coordinates and write our Hamiltonian in the form of N *uncoupled* harmonic oscillators

$$H^{(2)} = \frac{\omega_1}{2}(x_1{}^2 + y_1{}^2) + \frac{\omega_2}{2}(x_2^2 + y_2^2) + \ldots + \frac{\omega_N}{2}(x_N^2 + y_N^2) = E, \qquad (7)$$

where x_k, y_k, $k = 1, 2, \ldots, N$ are the new position and momentum coordinates and ω_k represent the normal mode frequencies of the system.

Theorem (Lyapunov) If none of the ratios of these eigenvalues, ω_j/ω_k, is an integer, for any $j, k = 1, 2, \ldots, N$, $j \neq k$, the linear normal modes continue to exist as periodic solutions of the nonlinear system (5) when higher order terms $H_3, H_4, \ldots$ etc. are taken into account in (6).

These solutions have frequencies close to those of the linear modes and are examples of what we call simple periodic orbits (SPOs), where all variables oscillate with the same frequency $\omega_k = 2\pi/T_k$, returning to the same values after a single maximum (and minimum).

These are also called nonlinear normal modes, or NNMs. As we vary the total energy E in (6) their stability under small perturbations of their initial conditions changes and although a local property, is often relevant for the more global stability properties of the system!

# The case of $N = 1$ degree of freedom

One of the first physical systems that we encounters in our studies is the harmonic oscillator shown in Fig. 9 described by Newton's second order differential equation

$$m\frac{d^2q}{dt^2} = -kq, \tag{8}$$

where $k > 0$ is a constant representing the hardness (or softness) of the spring. Equation (8) can be easily solved to yield the displacement $q(t)$ as an oscillatory function of time of the form

$$q(t) = A\sin(\omega t + \alpha), \quad \omega = \sqrt{k/m}, \tag{9}$$

where A and α are free constants corresponding to the amplitude and phase of oscillations and ω is the frequency.
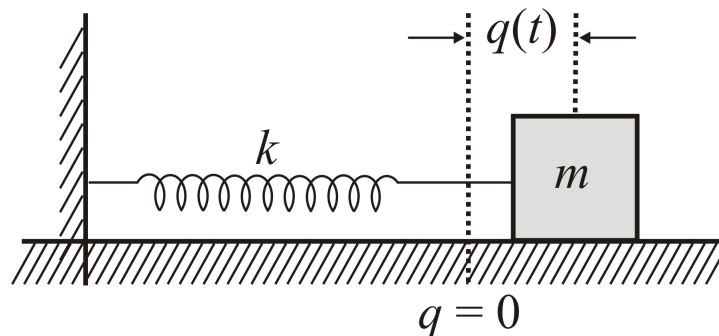
If we now recall that $p = mdq/dt$ represents the momentum of the mass m, we rewrite (8) in the form of two first order ODEs

$$\frac{dq}{dt} = \frac{p}{m} = \frac{\partial H}{\partial p}, \quad \frac{dp}{dt} = -kq = -\frac{\partial H}{\partial q}, \tag{10}$$

derived from the $N = 1$ dof Hamiltonian function

$$H(q, p) = \frac{p^2}{2m} + k\frac{q^2}{2} = E, \tag{11}$$

which represents the total (kinetic plus potential) energy. If we plot the solutions as orbits in the (q, p) phase space we obtain the curves shown below, where $q(t)$ and $p(t)$ oscillate periodically with the same frequency ω.
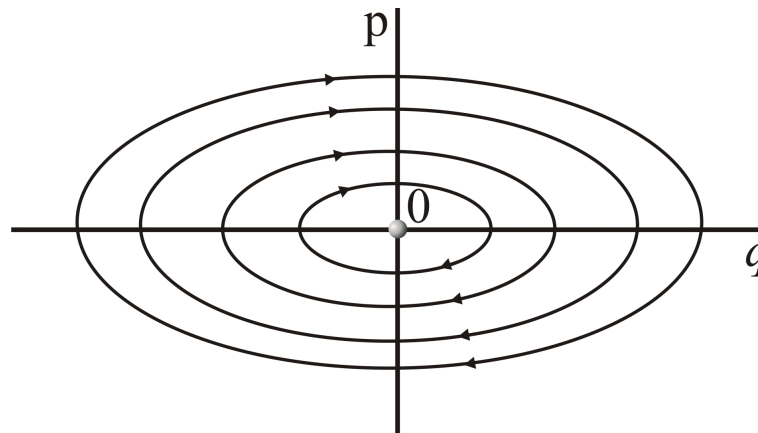
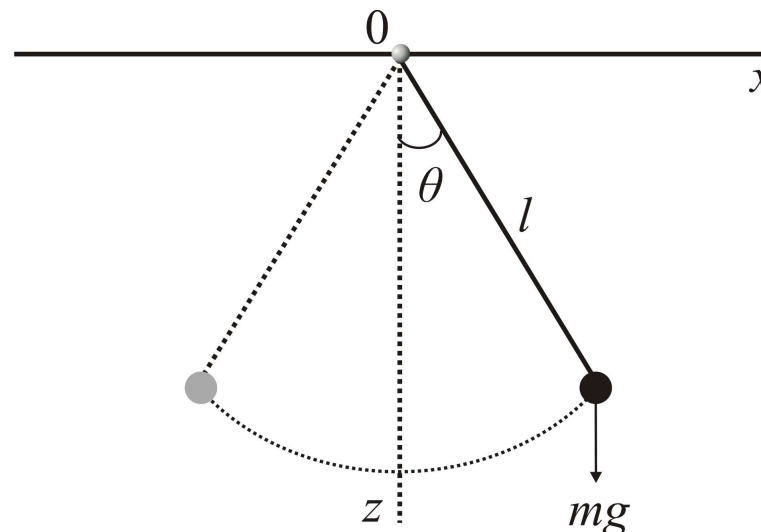# A nonlinear system of N=1 degrees of freedom

A more interesting one dof Hamiltonian system representing the motion of a simple pendulum shown in Fig. 11. Its equation of motion is

$$ml^2 \frac{d^2\theta}{dt^2} = -mlg \sin\theta, \tag{12}$$

If we now write this equation as a system of two first order ODEs, we find again that they can be cast in Hamiltonian form

$$\frac{dq}{dt} = p = \frac{\partial H}{\partial p}, \quad \frac{dp}{dt} = -\frac{g}{l}\sin q = -\frac{\partial H}{\partial q}, \tag{13}$$
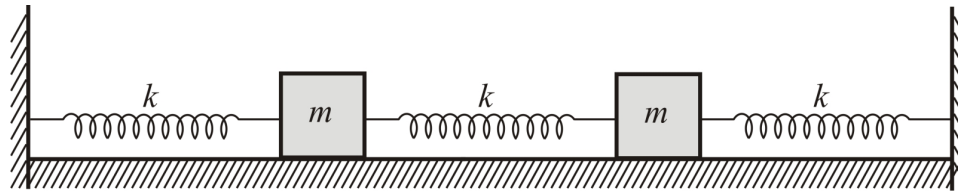
where $q = \theta$.

In this case, the energy integral is

$$H(q, p) = \frac{p^2}{2} + \frac{g}{l}(1 - \cos q) = E. \tag{14}$$

Plotting this family of curves in the (q, p) phase space for different values of E we now obtain a much more interesting picture than Fig. 10 depicted in Fig. 12 below. Observe that, besides the elliptic fixed point at the origin, there are two new equilibria located at the points $(\pm\pi, 0)$. These points A and B are called saddle points and are unstable in contrast to the $(0, 0)$ fixed point, which is stable characterized by what we called conditional (or neutral) stability.
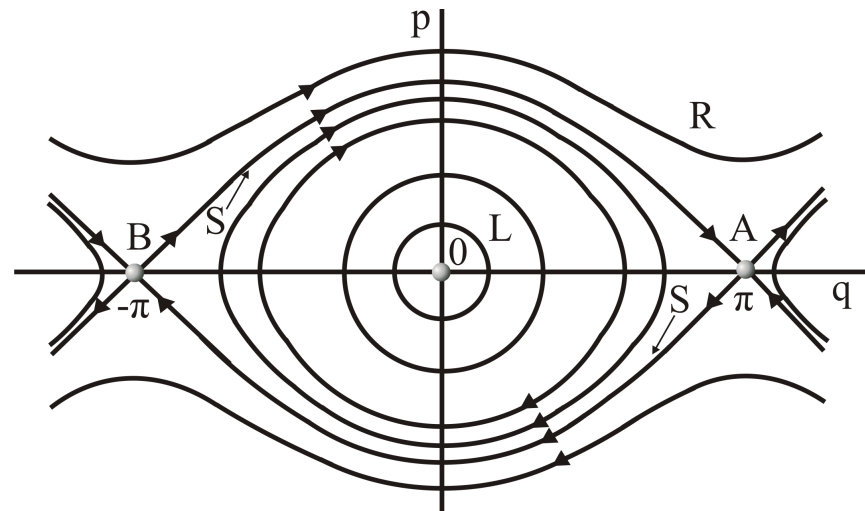
The case of N=2 degrees of freedom: Integrability and chaos

Let us extend our study to Hamiltonian systems of two dof, joining at first two harmonic oscillators, as shown in Fig. 13. We shall assume that our oscillators have equal masses $m_1 = m_2 = m$ and spring constants $k_1 = k_2 = k$ and impose fixed boundary conditions to their endpoints.

Newton's equations of motion give in this case:

$$m\frac{d^2 q_1}{dt^2} = -kq_1 - k(q_1 - q_2), \quad m\frac{d^2 q_2}{dt^2} = -kq_2 + k(q_1 - q_2), \qquad (15)$$

where $q_i(t)$ are the particles' displacements from their equilibrium positions at $q_i = 0$, $i = 1, 2$. If we also introduce the momenta $p_i(t)$ of the two particles in terms of their velocities, we obtain the Hamiltonian function

$$H(q_1, p_1, q_2, p_2) = \frac{p_1^2}{2m} + \frac{p_2^2}{2m} + k\frac{q_1^2}{2} + k\frac{q_2^2}{2} + k\frac{(q_1 - q_2)^2}{2} = E \qquad (16)$$

If we now change variables

$$Q_1 = \frac{q_1 + q_2}{\sqrt{2}}, \quad Q_2 = \frac{q_1 - q_2}{\sqrt{2}}, \quad P_1 = \frac{p_1 + p_2}{\sqrt{2}}, \quad P_2 = \frac{p_1 - p_2}{\sqrt{2}} \tag{17}$$

we see that, adding and subtracting by sides the two equations in (15) (dividing also by m and introducing $\omega = \sqrt{k/m}$), splits the problem into two uncoupled harmonic oscillators

$$\frac{dQ_i}{dt} = \frac{P_i}{m}, \quad \frac{dP_i}{dt} = -\omega_i^2 Q_i, \quad i = 1, 2, \quad \omega_1 = \omega, \quad \omega_2 = \sqrt{3}\omega, \tag{18}$$

with frequencies ω_1, ω_2. The new Hamiltonian of the system

$$K(Q_1, P_1, Q_2, P_2) = \frac{P_1^2}{2m} + \frac{P_2^2}{2m} + k\frac{Q_1^2}{2} + 3k\frac{Q_2^2}{2} = E. \tag{19}$$

is expressed as the sum of the Hamiltonians of these oscillators. Thus, changing variables we have performed a canonical coordinate transformation and realize that our system possesses two integrals of the motion

$$F_i(Q_1, P_1, Q_2, P_2)) = \frac{P_i^2}{2m} + k_i\frac{Q_i^2}{2} = E_i, \quad i = 1, 2, \tag{20}$$

with $k_1 = k$, $k_2 = 3k$, while E_i are two free parameters of the system to be fixed by the initial conditions $q_i(0)$, $p_i(0)$, $i = 1, 2$.

The solutions of this system are, in general, linear combinations of trigonometric functions with frequencies $\omega_1 = \sqrt{k}$, $\omega_2 = \sqrt{3k}$. If these were rationally dependent, i.e. if their ratio were a rational number $\omega_1/\omega_2 = m_1/m_2$ (m_1, m_2 all orbits close on 2-dimensional invariant tori and the motion would be periodic. In our example, this could only happen for initial conditions such that E_1 or E_2 is zero.

For E_1 and E_2 both non-zero the oscillations are quasiperiodic, as they are the superposition of trigonometric terms whose frequencies are rationally independent, since the ratio $\omega_2/\omega_1 = \sqrt{3}$ is irrational. Hence, the orbits in the 4-dimensional phase space are never closed, i.e. they never pass by the same point and eventually cover uniformly a 2-dimensional torus specified by the values of E_1 and E_2.
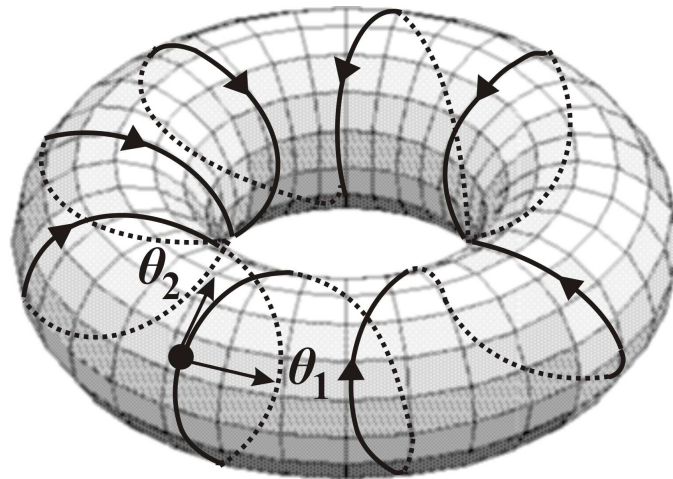
A nonlinear system of N=2 degrees of freedom

We now turn to a system of two coupled nonlinear oscillators connected with the famous Hénon and Heiles Hamiltonian

$$H = \frac{1}{2}(p_1^2 + p_2^2) + \frac{1}{2}(\omega_1^2 q_1^2 + \omega_2^2 q_2^2) + q_1^2 q_2 - \frac{C}{3} q_2^3. \tag{21}$$

describing the motion of a star of mass m in the axisymmetric potential of a galaxy. Introducing the more convenient variables $q_1 = x$, $q_2 = y$, $p_1 = p_x$, $p_2 = p_y$, we rewrite the above Hamiltonian in the form

$$H = \frac{1}{2}(p_x^2 + p_y^2) + V(x,y) = \frac{1}{2}(p_x^2 + p_y^2) + \frac{1}{2}(Ax^2 + By^2) + x^2 y - \frac{C}{3} y^3 = E, \tag{22}$$

where E is the total energy and we have set $\omega_1^2 = A > 0$ and $\omega_2^2 = B > 0$. Newton's equations of motion associated with this system are

$$\frac{d^2 x}{dt^2} = -\frac{\partial V}{\partial x} = -Ax - 2xy, \quad \frac{d^2 y}{dt^2} = -\frac{\partial V}{\partial y} = -By - x^2 + Cy^2. \tag{23}$$

Note that (22) represents a first integral of this system. If we could also find a second one, the problem would be completely integrable and could be integrated by quadratures. This, however, is highly unlikely in general!

The surprising result is there are only 3 known cases in which a second integral exists, allowing one to solve the Hénon-Heiles equations completely:

$$\text{Case} \ \ 1: \ \ A = B, \ \ C = -1,$$

$$\text{Case} \ \ 2: \ \ A, B \ \text{ free}, \ \ C = -6,$$

$$\text{Case} \ \ 3: \ \ B = 16A, \ \ C = -16. \tag{24}$$

In these cases, most orbits (in phase space domains of bounded motion) would be quasiperiodic and lie on 2-dimensional tori rendering the dynamics perfectly regular and predictable. For all other parameter values, one finds (besides periodic and quasiperiodic orbits), a new kind of solution that appears "irregular" and "unpredictable", which we call chaotic. These solutions tend to occupy densely 3-dimensional regions in the 4-dimensional phase space and depend very sensitively on initial conditions, in the sense that almost all other orbits in their vicinity deviate exponentially from the chaotic orbit as time increases.
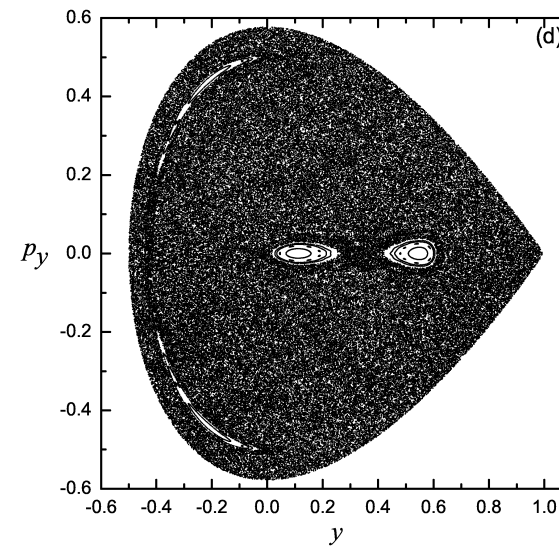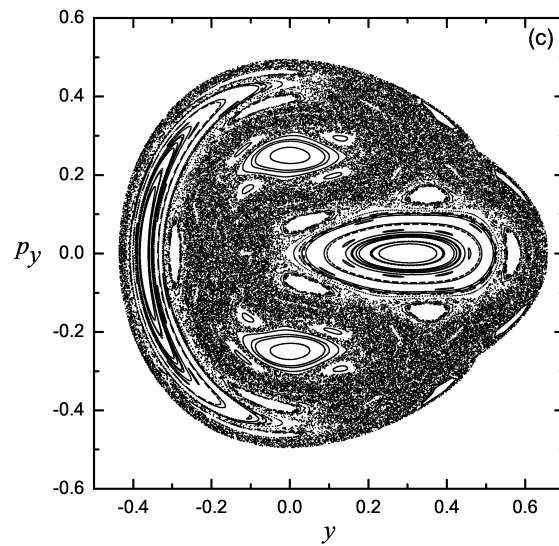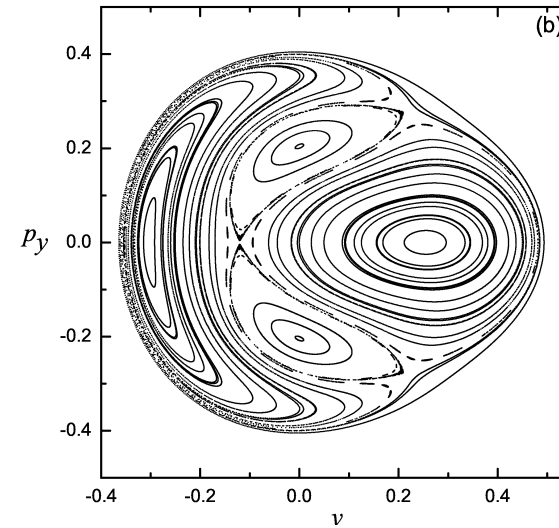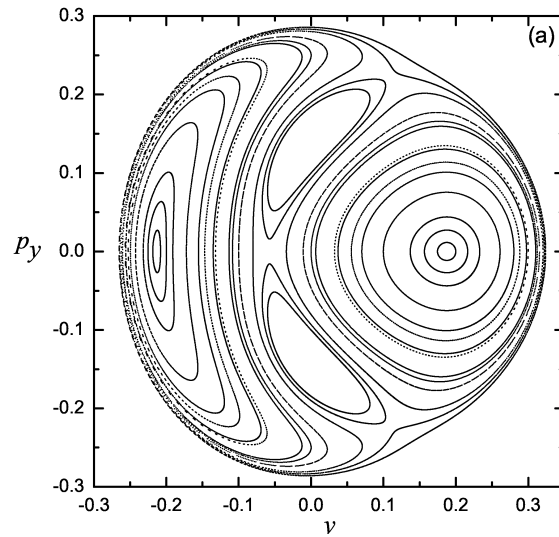
Figure 1: On the Poincare Surface of Section (y, p_y) for (a) $E = 1/24$ and (b) $E = 1/12$, no chaotic orbits are visible. At (c) $E = 1/8$, we observe islands of order surrounded by chaos. In (d), where $E = 1/6$, chaotic motion extends over most of phase space.

Stability Analysis of Periodic Orbits

To discuss the stability of periodic orbits, we need two fundamental concepts: The first is more analytical and is provided by Floquet theory and the second is more numerical and refers to the so-called Poincaré map and its associated surfaces of section (PSS).
In particular, we will assume that our n-dimensional dynamical system, cast in the general form $\dot{\vec{x}} = \vec{f}(\vec{x})$ (see (1)) has a periodic solution $\hat{\vec{x}}(t) = \hat{\vec{x}}(t+T)$ of period T. Let us choose an arbitrary point along this orbit $\hat{\vec{x}}(t_0)$ and define a PSS at that point as follows

$$\Sigma_{t_0} = \left\{ \vec{x}(t) \ / \ (\vec{x}(t) - \hat{\vec{x}}(t_0)) \cdot \vec{f}(\hat{\vec{x}}(t_0)) = 0 \right\}. \tag{25}$$

Thus, Σ_{t_0} is a $(n-1)$-dimensional plane which intersects the given periodic orbit at $\hat{\vec{x}}(t_0)$ and is vertical to the direction of the flow at that point. Clearly now a Poincaré map can be defined on that plane, by

$$P : \Sigma_{t_0} \to \Sigma_{t_0}, \quad \vec{x}_{k+1} = P\vec{x}_k, \quad k = 0, 1, 2, \ldots \tag{26}$$

for which $\vec{x}_0 = \hat{\vec{x}}(t_0)$ is a fixed point, since $\vec{x}_0 = P\vec{x}_0$.

We now examine small deviations about this point,

$$\vec{x}_k = \hat{\vec{x}}_0 + \vec{\eta}_k, \quad ||\vec{\eta}_k|| \ll \varepsilon, \tag{27}$$

(where ε is of the same magnitude as $||\hat{\vec{x}}_0||$), substitute (27) in (26) and linearize the Poincaré map to obtain

$$\vec{\eta}_{k+1} = DP(\hat{\vec{x}}_0)\vec{\eta}_k, \tag{28}$$

where we have neglected higher order terms in $\vec{\eta}$ and $DP(\hat{\vec{x}}_0)$ denotes the Jacobian of P evaluated at $\hat{\vec{x}}_0$.

To determine P we may use the *variational equations* of the original differential equations derived by writing $\vec{x}(t) = \hat{\vec{x}}(t) + \vec{\xi}(t)$, whence linearizing (1) about this periodic orbit leads to the system

$$\dot{\vec{\xi}}(t) = A(t)\vec{\xi}(t), \quad A(t) = A(t + T), \tag{29}$$

where $A(t)$ is the Jacobian matrix of $\vec{f}(\vec{x})$ evaluated at the periodic orbit $\vec{x}(t) = \hat{\vec{x}}$. The crucial question, of course, we must face now is: How are the two linear systems (28) and (29) related to each other?

Observe that we have used different notations for the small deviations about the periodic orbit: $\vec{\xi}(t)$ in continuous time (for the differential equations) and $\vec{\eta}_k$ in discrete time (for the Poincaré map). Furthermore, their dimensionality as vectors in the n-dimensional phase space $\mathbb{R}^n$ ($n = 2N$ for a Hamiltonian system) is different: $\vec{\xi}(t)$ is n-dimensional, while $\vec{\eta}_k$ is $(n-1)$-dimensional! How are we to match these two vectors of small deviations?

The answer comes from what is called Floquet theory (see Perko, 1995,Wiggins, 1990). First we realize that since (29) is a linear system of ODEs it must possess, in general, n linearly independent solutions, forming the columns of the $n \times n$ *fundamental solution* matrix $M(t, t_0)$ in

$$\vec{\xi}(t) = M(t, t_0)\vec{\xi}(0), \quad M(t, t_0) = M(t + T, t_0) \tag{30}$$

Now, if we change our basis at the point $\hat{\vec{x}}(t_0)$ so that one of the directions of motion is along the direction *vertical* to the PSS (25), we will observe that the nth column of the matrix $M(T, t_0)$ has zero elements except at the last entry which is 1. Thus, if we eliminate from this matrix its nth row and nth column, it turns out that its $(n-1) \times (n-1)$ submatrix is none other than the Poincaré map (26) itself!

This means that if we could compute the so-called monodromy matrix $M(T, t_0)$ numerically we could evaluate its eigenvalues, $\mu_1, \ldots, \mu_{n-1}$ (the last one being $\mu_n = 1$), which are those of the Poincaré map and determine the stability of our periodic orbit as follows: If they are all on the unit circle, i.e. $|\mu_i| = 1$, $i = 1, \ldots, n - 1$, the periodic orbit is (linearly) stable, while if (at least) one of them satisfies $|\mu_j| > 1$ the periodic solution is unstable.

But how do we compute the monodromy matrix $M(T, t_0)$? It is not so difficult. Let us first set $t_0 = 0$ for convenience and observe from (30) that $M(0, 0) = I_n$. All we have to do is integrate numerically the variational equations (30) from $t = 0$ to $t = T$, n times, each time for a *different* initial vector $(0, \ldots, 0, 1, 0, \ldots, 0)$ with 1 placed in the ith position, $i = 1, 2, \ldots, n$.

Note that since these equations are linear numerical integration can be performed to *arbitrary accuracy* and is also not too-time consuming for reasonable values of the period T. Once we have calculated $M(T, 0)$, we may proceed to compute its eigenvalues and determine the stability of the periodic orbit according to whether at least one of these eigenvalues has magnitude greater than 1.

Local Dynamics of N–Degree– of–Freedom Hamiltonians

The Fermi–Pasta–Ulam (FPU)-β model

The FPU -β one-dimensional lattice is described by the Hamiltonian

$$H = \frac{1}{2} \sum_{j=1}^{N} \dot{x}_j^2 + \sum_{j=0}^{N} \left(\frac{1}{2}(x_{j+1} - x_j)^2 + \frac{1}{4}\beta(x_{j+1} - x_j)^4 \right) = E \quad (31)$$

Let us focus on **Simple Periodic Orbits**(SPOs), where all variables oscillate in or out of phase and return to their initial state after only one maximum and one minimum in their oscillation. The SPOs we consider here are:

I. The FPU π-mode under periodic boundary conditions:

$$x_{N+k}(t) = x_k(t), \ \forall t, k \quad (32)$$

where the particles execute out-of-phase motion (OPM) with N even

$$\hat{x}_j(t) = -\hat{x}_{j+1}(t) \equiv \hat{x}(t), \ j = 1, \ldots, N. \quad (33)$$

II. For the FPU model and fixed boundary conditions:

$$x_0(t) = x_{N+1}(t) = 0, \ \forall t \tag{34}$$

(a) **The SPO1 mode**, with N odd,

$$\hat{x}_{2j}(t) = 0, \ \hat{x}_{2j-1}(t) = -\hat{x}_{2j+1}(t) \equiv \hat{x}(t), \ j = 1, \ldots, \frac{N-1}{2}. \tag{35}$$

(b) **The SPO2 mode**, with $N = 5 + 3m, \ m = 0, 1, 2, \ldots$ particles,

$$
\begin{aligned}
x_{3j}(t) &= 0, \ j = 1, 2, 3 \ldots, \frac{N-2}{3}, \tag{36} \\
x_j(t) &= -x_{j+1}(t) = \hat{x}(t), \ j = 1, 4, 7, \ldots, N-1. \tag{37}
\end{aligned}
$$

Let us see some of these solutions graphically in the figure of the next page:

FPU N=4 OPM with fixed boundary conditions

FPU N=7 SPO1 with fixed boundary conditions

FPU N=8 SPO2 with fixed boundary conditions
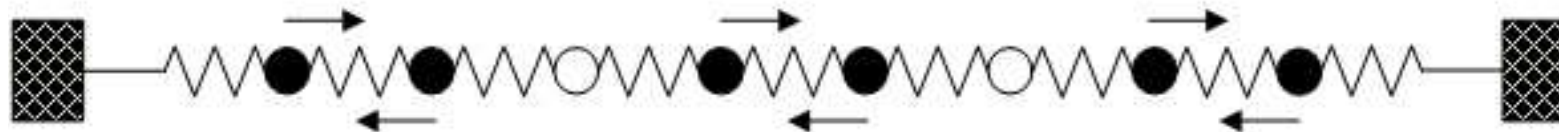
An application of Floquet stability analysis

Stability analysis of SPOs is performed by studying the eigenvalues of the monodromy matrix. To see how this is done consider the SPO1 mode of FPU, for which the equations of motion collapse to a single second order ODE:

$$\ddot{\hat{x}}(t) = -2\hat{x}(t) - 2\beta\hat{x}^3(t) \tag{38}$$

Its solution is well–known in terms of Jacobi elliptic functions

$$\hat{x}(t) = \mathcal{C}\,\mathrm{cn}(\lambda t, \kappa^2) \tag{39}$$

with modulus κ^2. Linearizing about this solution $x_j = \hat{x}_j + \xi_j$, by keeping up to linear terms in ξ_j, we get the variational equations

$$\ddot{\xi}_j = (1 + 3\beta\hat{x}^2)(\xi_{j-1} - 2\xi_j + \xi_{j+1}), \ j = 1, \ldots, N \tag{40}$$

which are equivalent to (30). In our case here, these separate into N uncoupled Lamé equations

$$\ddot{z}_j(t) + 4(1 + 3\beta\hat{x}^2)\sin^2\left(\frac{\pi j}{2(N+1)}\right)z_j(t) = 0, \ j = 1, \ldots, N \tag{41}$$

where the z_j variations are simple linear combinations of the ξ_j's.

Changing variables to $u = \lambda t$, the above equation takes the form

$$z_j''(u) + 2\big(1 + 4\kappa^2 - 6\kappa^2 \text{sn}^2(u, \kappa^2)\big)\sin^2\left(\frac{\pi j}{2(N+1)}\right)z_j(u) = 0, \; j = 1, \ldots, N \qquad (42)$$

where primes denote differentiation with respect to u. According to Floquet theory, its solution is bounded (or unbounded) depending on whether the eigenvalues of the monodromy matrix are **on or off the unit circle**.

These periodic solutions all experience **a first destabilization at energy densities**:

$$\frac{E_c}{N} \propto N^{-\alpha}, \; \alpha = 1, \; or, \; 2, \; N \to \infty. \qquad (43)$$

More specifically, the first variation $z_j(u)$ to become unbounded as κ^2 (or, the energy E) increases is $j = \frac{N-1}{2}$ and the energy values $E_c/N \propto 1/N$ at which this happens are plotted below.
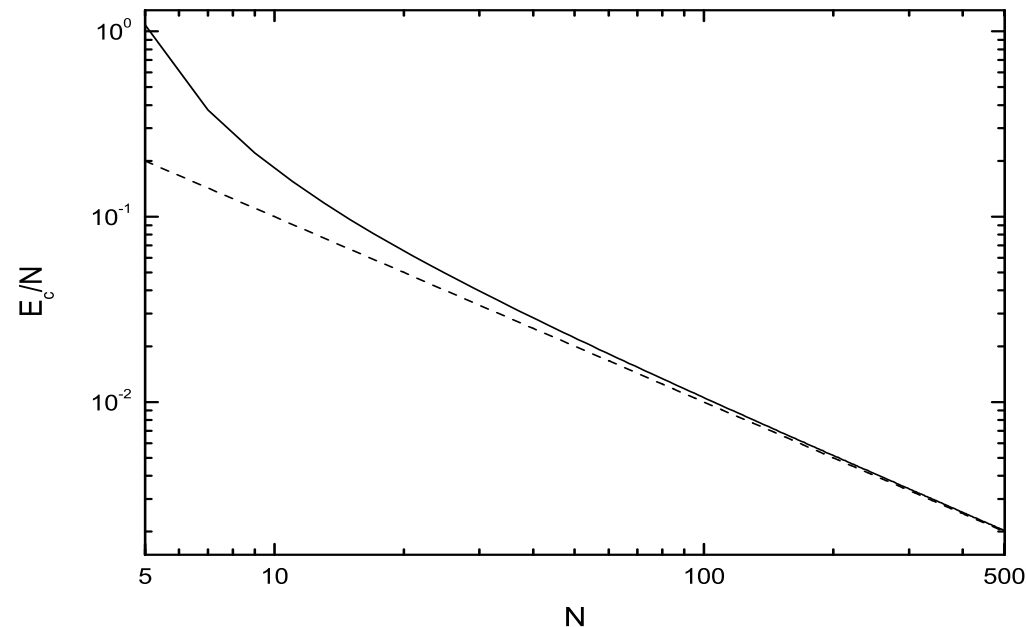
Figure 2: $\frac{E_c}{N}$ of **the first destabilization of the SPO1 solution** of the FPU system (**the** $k = (N+1)/2$ **mode**) obtained by the monodromy eigenvalues. The dashed line is the function $\propto \frac{1}{N}$.

The OPM (or π-mode) on the other hand, becomes unstable, as the eigenvalues of their monodromy matrix exit the unit circle on the real axis at -1, giving rise to a sequence of period–doubling bifurcations. It is associated with chaos over a wide region of phase space, since **its first destabilization occurs at a relatively high value of the total energy**.

An Analytical Criterion for "Weak" Chaos

As was shown recently by Flach et al. (2005), the linear modes of the FPU β – model can be continued as SPOs of the corresponding lattice. In fact, the energy threshold for the destabilization of the **low k - modes** ($k = 1, 2, 3, ..$) coincides with the "weak" chaos threshold shown by de Luca and Lichtenberg (1995) to be associated with the **breakup of the famous FPU recurrences**. By k–modes, we refer here to the linear normal modes of the FPU lattice

$$Q_k = \sqrt{\frac{2}{N+1}} \sum_{i=1}^{N} q_i \sin \frac{ki\pi}{N+1}, \qquad P_k = \dot{Q}_k \tag{44}$$

with energies and frequencies

$$E_k = \frac{1}{2} \left[P_k^2 + \omega_k{}^2 Q_k^2 \right], \quad \omega_k = 2\sin \frac{k\pi}{2(N+1)} \tag{45}$$

Using linear stability analysis, Flach et al. (2005) reported an approximate formula for the destabilization energy of the **low $k = 1, 2, 3, ..$ modes** given by

$$E_c \approx \frac{\pi^2}{6\beta(N+1)}. \tag{46}$$

Evidently, this destabilization occurs at **much lower energies than the π-mode, or the SPO1 mode** since $E_c/N \propto N^{-2}$ for large N and and is thus associated with **"thin" chaotic layers (or "weak chaos") in phase space**. In fact, this energy threshold **coincides with the instability threshold of our SPO2 mode** (see Figure 3 below)!
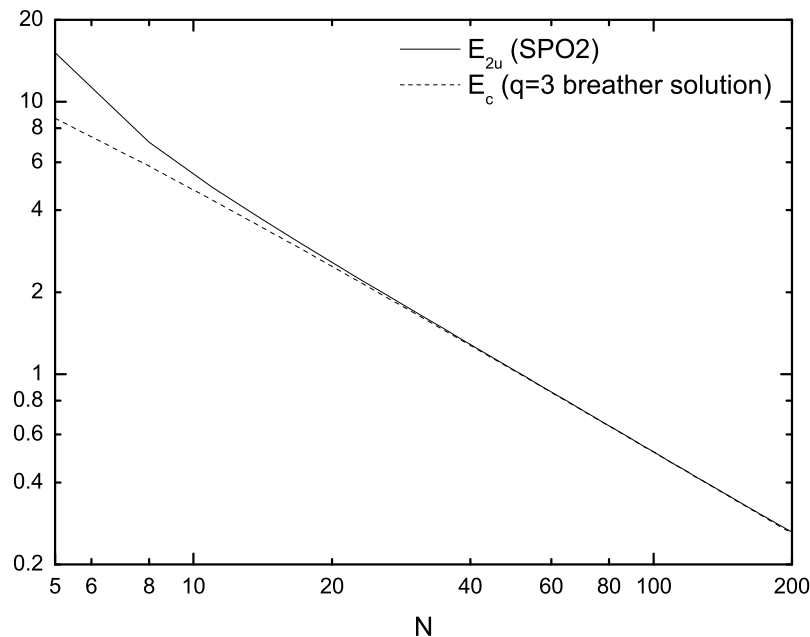

Figure 3: The solid curve is the energy E_c/N of the first destabilization of the SPO2 (**the $k = 2(N + 1)/3$ mode**) for $\beta = 0.0315$ obtained from the eigenvalues of the monodromy matrix and the dashed line is the approximate formula.

Spectrum of Lyapunov Exponents and "Strong" Chaos

Convergence of Lyapunov Spectra

We now evaluate, in the neighborhood of our SPOs the **Lyapunov spectra**:

$$L_i, \ i = 1, \ldots, 2N, \ L_1 \equiv L_{\max} > L_2 > \ldots > L_{2N}. \tag{47}$$

If the largest one, $L_1 \equiv L_{\max} > 0$, the orbit is chaotic. In particular, we compute in the limit $t \to \infty$ the quantities

$$K_t^i = \frac{1}{t} \ \ln \frac{\| \ \vec{w}_i(t) \ \|}{\| \ \vec{w}_i(0) \ \|}, \tag{48}$$

where $\vec{w}_i(0)$ and $\vec{w}_i(t), \ i = 1, \ldots, 2N$ are deviation vectors from the given orbit $\vec{x}(t)$. After every T_j, following the Bennetin et al.(1980) algorithm, we ortho–normalize the vectors $\vec{w}_i(t)$ and obtain finally L_i by

$$L_i = \lim_{t \to \infty} \frac{1}{n} \sum_{j=1}^{n} K_{T_j}^i, \ n \to \infty. \tag{49}$$

Observe that in the figure below we have plotted the Lyapunov spectrum of **both the OPM and the SPO1 mode** of the FPU Hamiltonian for $N = 16$ and **periodic boundary conditions** at the energy $E = 6.82$ where both of them are unstable. We see that the two Lyapunov spectra are very close to each other suggesting that the chaotic regions are **"connected"**.
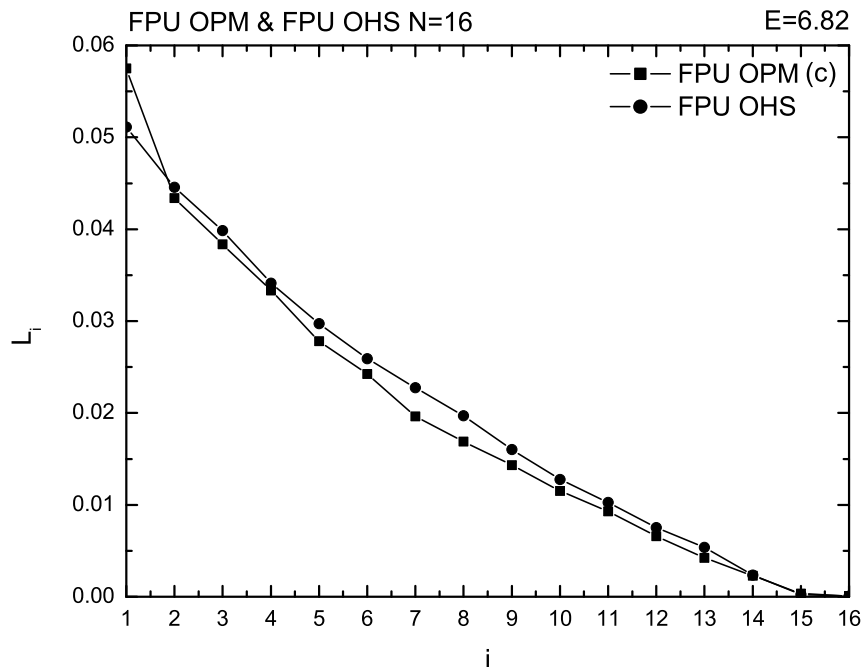

Figure 4: Lyapunov spectra of the OPM and the SPO1 modes of FPU, for $N = 16$ and periodic boundary conditions practically coincide at $E = 6.82$ where both are unstable.

More systematically, let us plot the Lyapunov spectra near the SPO1 and SPO2 modes, of the FPU system, for $N = 11$, **fixed boundary conditions** and energy values $E_1 = 1.94$ and $E_2 = 0.155$ respectively, where the SPOs have just destabilized.
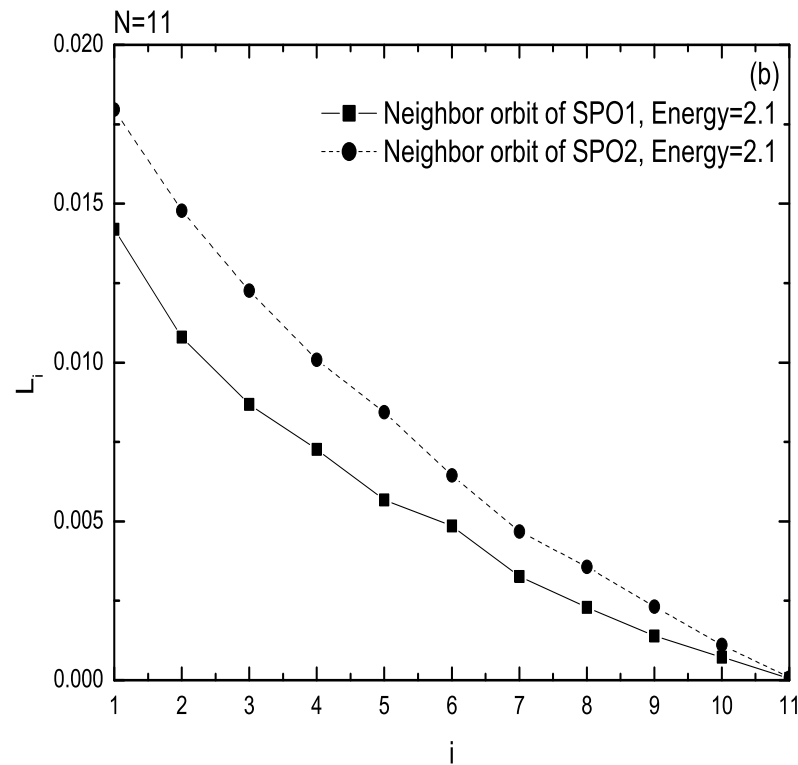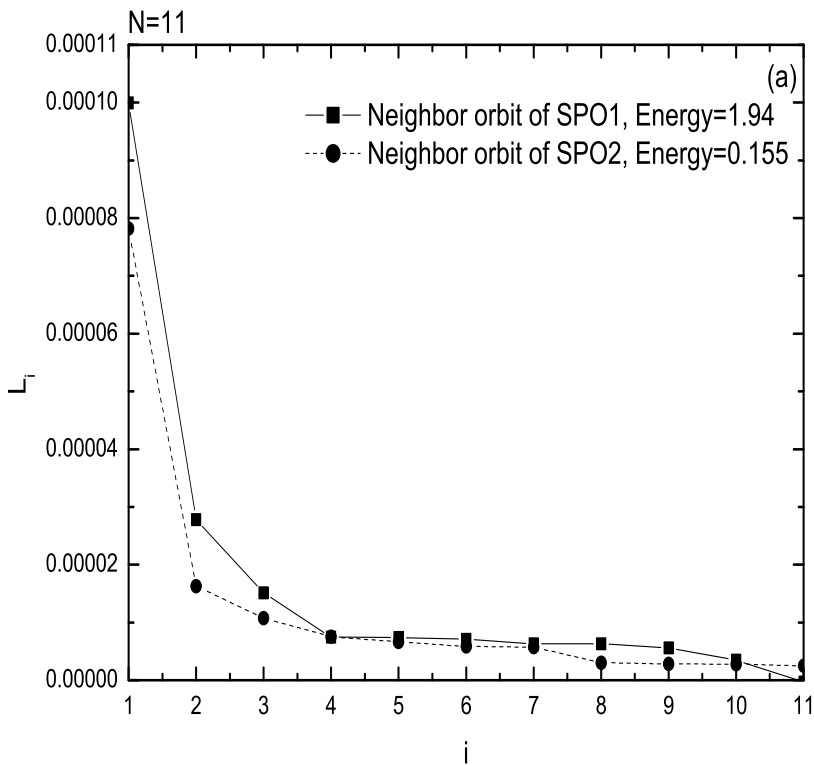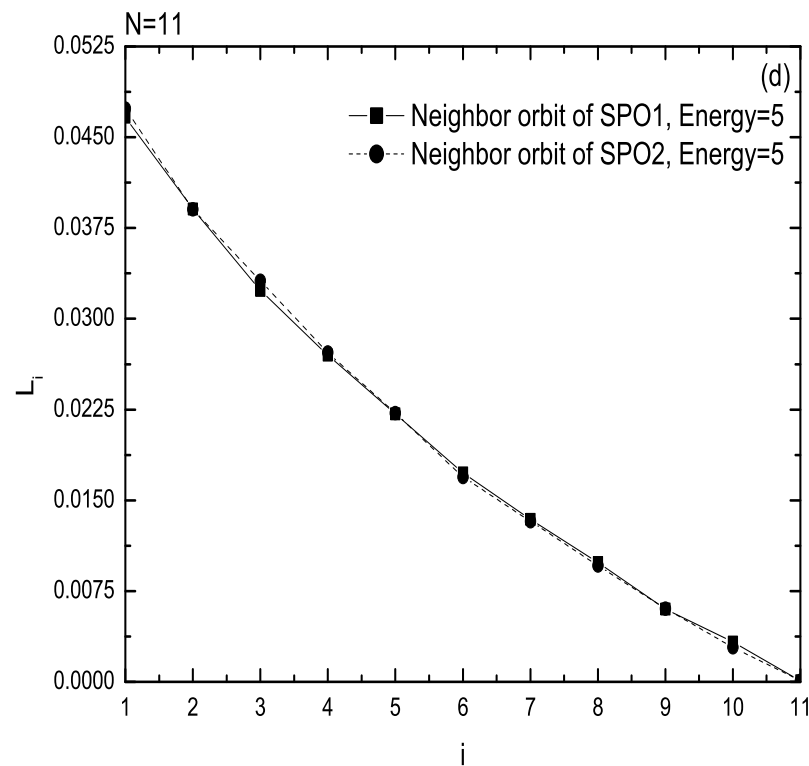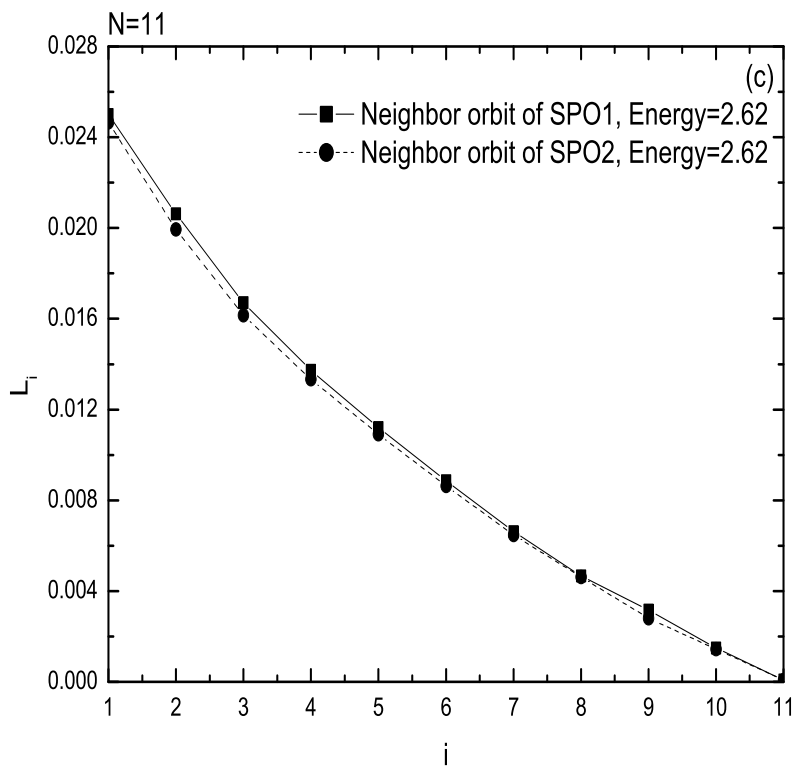
Figure 5: Lyapunov spectra near SPO1 and SPO2 for $N = 11$ at energies $E = 1.94$ and $E = 0.155$, where they have just destabilized. (b) Same as (a) at energy $E = 2.1$. (c) **Convergence of the Lyapunov spectra** near the two SPOs at energy $E = 2.62$. (d) Coincidence of Lyapunov spectra continues at higher energy $E = 4$.

Conclusions

1) We defined dynamical systems of continuous time and concentrated in particular on Hamiltonian systems of N degrees of freedom. Focusing on linear and nonlinear Hamiltonians of $N = 1$ and $N = 2$ degrees of freedom we described the concept of equilibrium points and discussed their stability analysis.

2) We then examined the important notions of periodic and quasiperiodic orbits and introduced the topics of integrability (related to regular or predictable behavior) and chaos (connected with unpredictable dynamics). We mentioned Floquet theory as the main tool for studying the stability of periodic orbits.

3) We studied local and global dynamics of N dof Hamiltonian systems, focusing on simple periodic orbits (SPOs) and showed that their first destabilization typically decays as

$$E_c/N \propto N^{-\alpha}, \ \alpha = 1, \ or, \ 2. \tag{50}$$

4) We explained on the FPU $\beta-$ model how **low k normal modes** of the linear lattice (but also relatively higher ones like $k = 2(N + 1)/3$), are important for the global dynamics, since their destabilization threshold obeys

$$E_c \approx \frac{\pi^2}{6\beta(N+1)}, \tag{51}$$

which is of the form $E_c/N \propto 1/N^2$ and is thus connected with **the onset of"weak" chaos**.

5) On the other hand, there are other linear modes, like the π-mode of the FPU lattice under periodic boundary condition, which when continued in the nonlinear regime **destabilize at higher energies**, at thresholds obeying

$$\frac{E_c}{N} \propto \frac{1}{N}, \quad N \to \infty. \tag{52}$$

and are thus related to **the onset of "strong chaos"** in these models.

6) We calculated the Lyapunov spectra in the vicinity of our SPOs solutions and observed that, as E increases, they attain same functional form,

$$L_i(N) \propto e^{-\alpha \frac{i}{N}}, i = 1, 2, \ldots, K(N) \tag{53}$$

and eventually converge, implying that the corresponding chaotic regions have "merged" and large scale chaos has spread in the system.

References

1. Skokos, Ch. [2001], "Alignment Indices: A New, Simple Method for Determining the Ordered or Chaotic Nature of Orbits", *J. Phys. A*, **34**, pp. 10029 – 10043.

2. Skokos, Ch., Antonopoulos, Ch., Bountis, T. C. and Vrahatis, M. N. [2003], "How does the Smaller Alignment Index (SALI) Distinguish Order from Chaos?", *Prog. Theor. Phys. Supp.*, **150**, pp. 439 – 443

3. Skokos, Ch., Antonopoulos, Ch., Bountis, T. C. and Vrahatis, M. N. [2004], "Detecting Order and Chaos in Hamiltonian Systems by the SALI Method", *J. Phys. A*, **37**, pp. 6269 – 6284.

4. Antonopoulos, Ch., Bountis, T. C. and Skokos, Ch., [2006], "Chaotic Dynamics of N–Degree–of–Freedom Hamiltonian Systems", International Journal of Bifurcation and Chaos, vol.**16**(6), 1777-1793 , June 2006.

5. Antonopoulos, Ch. and Bountis, T., [2006], "Stability of Simple Periodic Orbits and Chaos in an FPU Lattice", PRE**73**, 056206, 1-8 (2006).

6. T. Bountis, "Stability of Motion: From Lyapunov to N - Degree of Freedom Hamiltonian Systems", [2006], "Nonlinear Phenomena and Complex Systems", vol. **9**(3) ,209 -239, 2006.

7. Skokos, Ch., Bountis, T. and Antonopoulos, Ch. [2007], "Geometrical properties of local dynamics in Hamiltonian systems: the Generalized Alignment Index (GALI) method", Physica D **231**, 30.

COMPLEX DYNAMICS OF MULTIDIMENSIONAL HAMILTONIAN SYSTEMS

Tassos BOUNTIS, Haris Skokos, Chris Antonopoulos and Thanos Manos

Department of Mathematics and Center for Research and Applications of Nonlinear Systems (CRANS),

University of Patras, GR–26500, Rion, Patras, Greece

Lecture 2:

Order and Chaos in Multi-Dimensional Hamiltonian Systems

Workshop and Latin–American School on "Foundations of Complexity"
Rio de Janeiro, Brasil, October 4–30, 2015

Contents

1. The Method of Lyapunov Exponents

2. $\text{GALI}_k(t)$: Chaos and Order in Multidimensions

3. Analytical Estimates for the $\text{GALI}_k(t)$ Indices

4. Numerical Verification and Applications

5. Low - Dimensional Tori and Weak Diffusion

6. Conclusions

Complex Hamiltonian Dynamics

Tassos Bountis and Haris Skokos
Springer Synergetics series, April 2012

Foreword by Sergej Flach

Chaotic Dynamics of N–Degree– of–Freedom Hamiltonian Systems

We consider conservative systems described by the N - degree - of freedom Hamiltonian:

$$H \equiv H(q_1(t), \ldots, q_N(t), p_1(t), \ldots, p_N(t)) = E \qquad (1)$$

where E is the total (constant) energy and the positions $q_j(t)$, $j = 1, \ldots, N$ and momenta $p_j(t)$, $j = 1, \ldots, N$ are solutions of Hamilton's equations:

$$\frac{dq_j(t)}{dt} = \frac{\partial H}{\partial p_j(t)}, \quad \frac{dp_j(t)}{dt} = -\frac{\partial H}{\partial q_j(t)}, \ j = 1, \ldots, N. \qquad (2)$$

which are 2N first order ODEs which describe the orbits of the system in the 2N–dimensional phase space. One particular example we will be concerned with here is the **famous $\beta-$FPU 1–dimensional lattice** described by the Hamiltonian

$$H = \frac{1}{2} \sum_{j=1}^{N} \dot{x}_j^2 + \sum_{j=0}^{N} \left(\frac{1}{2}(x_{j+1} - x_j)^2 + \frac{1}{4}\beta(x_{j+1} - x_j)^4 \right) = E \qquad (3)$$

where $q_j = x_j, p_j = \dot{x}_j$.

Distinguishing Order from Chaos in Many Dimensions

The Method of Lyapunov Exponents

Perhaps the most popular method for identifying solutions of dynamical systems as **chaotic** is to evaluate, in the neighborhood of a solution the **spectrum of Lyapunov exponents**:

$$L_i, \ i = 1, \ldots, 2N, \ L_1 \equiv L_{\max} > L_2 > \ldots > L_{2N}. \tag{4}$$

If the largest one, $L_1 \equiv L_{\max} > 0$, the orbit is chaotic. In particular, we compute for large time intervals $t = T_j$ the quantities

$$K_t^i = \frac{1}{t} \ \ln \frac{\| \ \vec{w}_i(t) \ \|}{\| \ \vec{w}_i(0) \ \|}, \tag{5}$$

where $\vec{w}_i(t), \ i = 1, \ldots, 2N$ are deviation vectors **orthogonal to the vector tangent to the given orbit** $\vec{x}(t)$. Since orbits in chaotic regions rapidly deviate from each other, we need to repeat the calculation over many time intervals T_j, ortho–normalizing the vectors $\vec{w}_i(t)$ and choosing new $\vec{w}_i(0)$ every time to obtain **Lyapunov spectrum** L_i averaging over these intervals

$$L_i = \lim_{n \to \infty} \frac{1}{n} \sum_{j=1}^{n} K_{T_j}^i. \tag{6}$$

$\mathbf{GALI}_k(t)$: Chaos and Order in Multidimensions

So, to see if an orbit is chaotic, we monitor the evolution of **only one deviation vector** and wait to see whether **it will align with the direction corresponding to the $L_{max} > 0$**. This process, however, **has notorious convergence problems** and fails to provide a clear answer especially if L_{max} is very close to 0.

Thus, instead of following one deviation vector, we choose to study the **mutual relation of many of them** taken together. For example, note that the 'wedge' product of k **such unit vectors**, $\hat{w}_1 \wedge \hat{w}_2 \wedge ... \wedge \hat{w}_k$, yields **the 'volume' of a parallelepiped formed by these k vectors** as vertices. If the orbits are chaotic they will align in the $L_{max} > 0$-direction and **the volume would vanish**. If, on the other hand, there is no such direction the vectors will remain linearly independent and **the volume will be bounded away from zero**.

Now, all such normalized deviation vectors $\hat{w}_i$, $i = 1, 2, \ldots, 2N$, can be written as

$$\hat{w}_i = \sum_{j=1}^{2N} w_{ij} \hat{e}_j \quad , \quad i = 1, 2, \ldots, k \tag{7}$$

in terms of the usual orthonormal basis of the n–dimensional Euclidean space.

The wedge product of these k deviation vectors can be written with respect to the basis $\hat{e}_{i_k}$

$$\hat{w}_1 \wedge \hat{w}_2 \wedge \cdots \wedge \hat{w}_k = \sum_{1 \le i_1 < i_2 < \cdots < i_k \le 2N} \begin{vmatrix} w_{1i_1} & w_{1i_2} & \cdots & w_{1i_k} \\ w_{2i_1} & w_{2i_2} & \cdots & w_{2i_k} \\ \vdots & \vdots & & \vdots \\ w_{ki_1} & w_{ki_2} & \cdots & w_{ki_k} \end{vmatrix} \hat{e}_{i_1} \wedge \hat{e}_{i_2} \wedge \cdots \wedge \hat{e}_{i_k} \quad (8)$$

If **at least two** of the normalized deviation vectors $\hat{w}_i$, $i = 1, 2, \ldots, k$ are **linearly dependent**, all the $k \times k$ determinants will become zero **making the 'volume' vanish**. We define the norm of this quantity, $\|\hat{w}_1(t) \wedge \hat{w}_2(t) \wedge \cdots \wedge \hat{w}_k(t)\|$, as **the generalized alignment index**

$$GALI_k(t) = \left\{ \sum_{1 \le i_1 < i_2 < \cdots < i_k \le 2N} \begin{vmatrix} w_{1i_1} & w_{1i_2} & \cdots & w_{1i_k} \\ w_{2i_1} & w_{2i_2} & \cdots & w_{2i_k} \\ \vdots & \vdots & & \vdots \\ w_{ki_1} & w_{ki_2} & \cdots & w_{ki_k} \end{vmatrix}^2 \right\}^{1/2} \quad (9)$$

Analytical Estimates for the $\mathbf{GALI}_k(t)$ Indices

If at least one of the deviation vectors **becomes linearly dependent** on the remaining ones, $\text{GALI}_k(t)$ **will tend to zero** as the volume of the parallelepiped having the vectors $\hat{w}_i$ as edges shrinks to zero. On the other hand, if $\text{GALI}_k(t)$ **remains far from zero**, this would indicate the **linear independence** of the deviation vectors.

Theoretical results for the Time Evolution of GALI

Exponential decay of GALI for chaotic orbits

Let us first investigate the dynamics in the vicinity of a chaotic orbit of a Hamiltonian system, with N degrees of freedom. Let $\sigma_1 \geq \sigma_2 \geq \cdots \geq \sigma_{2N}$ be the **'local Lyapunov exponents'** oscillating about their time averaged values

$$\sigma_1 \geq \sigma_2 \geq \cdots \geq \sigma_{N-1} \geq \sigma_N = \sigma_{N+1} = 0 \geq \sigma_{N+2} \geq \cdots \geq \sigma_{2N}. \qquad (10)$$

which are the 'global' LCEs. Assuming that the σ_i, $i = 1, 2, \ldots, 2N$ do not fluctuate significantly, the evolution of any initial deviation vector $\vec{w}_i$ may be written as

$$\vec{w}_i(t) = \sum_{j=1}^{2N} c_j^i \, e^{\sigma_j t} \, \hat{e}_j \,, \qquad (11)$$

Consequently, the matrix **C** of coefficients of the k **normalized deviation vectors** $\hat{w}_i(t) = \vec{w}_i(t)/\|\vec{w}_i(t)\|$, $i = 1, 2, \ldots, k$ expressed in terms of the basis $\{\hat{e}_1, \hat{e}_2, \ldots, \hat{e}_{2N}\}$ becomes

$$
\mathbf{C}(t) = [c_{ij}] = \begin{bmatrix}
s_1 & \frac{c_2^1}{|c_1^1|}e^{-(\sigma_1-\sigma_2)t} & \frac{c_3^1}{|c_1^1|}e^{-(\sigma_1-\sigma_3)t} & \ldots & \frac{c_{2N}^1}{|c_1^1|}e^{-(\sigma_1-\sigma_{2N})t} \\
s_2 & \frac{c_2^2}{|c_1^2|}e^{-(\sigma_1-\sigma_2)t} & \frac{c_3^2}{|c_1^2|}e^{-(\sigma_1-\sigma_3)t} & \ldots & \frac{c_{2N}^2}{|c_1^2|}e^{-(\sigma_1-\sigma_{2N})t} \\
\vdots & \vdots & \vdots & & \vdots \\
s_k & \frac{c_2^k}{|c_1^k|}e^{-(\sigma_1-\sigma_2)t} & \frac{c_3^k}{|c_1^k|}e^{-(\sigma_1-\sigma_3)t} & \ldots & \frac{c_{2N}^k}{|c_1^k|}e^{-(\sigma_1-\sigma_{2N})t}
\end{bmatrix},
$$

(12)

with $s_i = \text{sign}(c_1^i)$ and $i = 1, 2, \ldots, k$, $j = 1, 2, \ldots, 2N$.

This has been accomplished using the fact that a leading order estimate of the deviation vector's Euclidean norm, for long enough times, is

$$
\|\vec{w}_i(t)\| \approx |c_1^i|e^{\sigma_1 t} .
$$

(13)

The determinants appearing in the definition of $GALI_k$ (see equation (9)) can be divided in two categories depending on **whether or not they contain the first column of matrix C**. Indeed, we see that those that do contain the first column yield

$$
D_{1,j_1,j_2,\ldots,j_{k-1}} =
\begin{vmatrix}
s_1 & \dfrac{c_{j_1}^1}{|c_1^1|}e^{-(\sigma_1-\sigma_{j_1})t} & \cdots & \dfrac{c_{j_{k-1}}^1}{|c_1^1|}e^{-(\sigma_1-\sigma_{j_{k-1}})t} \\
s_2 & \dfrac{c_{j_1}^2}{|c_1^2|}e^{-(\sigma_1-\sigma_{j_1})t} & \cdots & \dfrac{c_{j_{k-1}}^2}{|c_1^2|}e^{-(\sigma_1-\sigma_{j_{k-1}})t} \\
\vdots & \vdots & & \vdots \\
s_k & \dfrac{c_{j_1}^k}{|c_1^k|}e^{-(\sigma_1-\sigma_{j_1})t} & \cdots & \dfrac{c_{j_{k-1}}^k}{|c_1^k|}e^{-(\sigma_1-\sigma_{j_{k-1}})t}
\end{vmatrix} =
$$

$$
=
\begin{vmatrix}
s_1 & \dfrac{c_{j_1}^1}{|c_1^1|} & \cdots & \dfrac{c_{j_{k-1}}^1}{|c_1^1|} \\
s_2 & \dfrac{c_{j_1}^2}{|c_1^2|} & \cdots & \dfrac{c_{j_{k-1}}^2}{|c_1^2|} \\
\vdots & \vdots & & \vdots \\
s_k & \dfrac{c_{j_1}^k}{|c_1^k|} & \cdots & \dfrac{c_{j_{k-1}}^k}{|c_1^k|}\cdot
\end{vmatrix}
e^{-\left[(\sigma_1-\sigma_{j_1})+(\sigma_1-\sigma_{j_2})+\cdots+(\sigma_1-\sigma_{j_{k-1}})\right]t}
\tag{14}
$$

Thus, the time evolution of $D_{1,j_1,j_2,\ldots,j_{k-1}}$ is mainly determined by the exponential law

$$D_{1,j_1,j_2,\ldots,j_{k-1}} \propto e^{-\left[(\sigma_1-\sigma_{j_1})+(\sigma_1-\sigma_{j_2})+\cdots+(\sigma_1-\sigma_{j_{k-1}})\right]t}. \tag{15}$$

The determinants that **do not contain the first column** of the transformation matrix **tend to zero following an exponential law that decays faster**.

Clearly, from all determinants **the one that decreases the slowest** is the one containing the first k columns of matrix **C**, yielding the approximation that GALI$_k$ tends to zero as

$$\text{GALI}_k(t) \propto e^{-[(\sigma_1-\sigma_2)+(\sigma_1-\sigma_3)+\cdots+(\sigma_1-\sigma_k)]t}. \tag{16}$$

The evaluation of GALI for ordered orbits

As is well–known, ordered orbits typically lie on N–dimensional tori, which can be described by a local transformation to action–angle variables, satisfying

$$
\begin{aligned}
\dot{J}_i &= 0 \\
\dot{\theta}_i &= \omega_i(J_1, J_2, \ldots, J_N)
\end{aligned}
\qquad i = 1, 2, \ldots, N.
\tag{17}
$$

These can be easily integrated to give

$$
\begin{aligned}
J_i(t) &= J_{i0} \\
\theta_i(t) &= \theta_{i0} + \omega_i(J_{10}, J_{20}, \ldots, J_{N0})\,t
\end{aligned}
\qquad i = 1, 2, \ldots, N,
\tag{18}
$$

By denoting as ξ_i, η_i, $i = 1, 2, \ldots, N$ small deviations of J_i and θ_i respectively, the variational equations of system (18), can be solved to yield:

$$
\begin{aligned}
\xi_i(t) &= \xi_i(0) \\
\eta_i(t) &= \eta_i(0) + \left[\sum_{j=1}^{N} \omega_{ij}\xi_j(0) \right] t
\end{aligned}
\qquad i = 1, 2, \ldots, N.
\tag{19}
$$

This implies a **linear increase** of the norm of the deviation vector

$$\|\vec{w}(t)\| = \left\{ 1 + \left[\sum_{i=1}^{N} \left(\sum_{j=1}^{N} \omega_{ij} \xi_j(0) \right) \right] t^2 + \left[2 \sum_{i=1}^{N} \left(\eta_i(0) \sum_{j=1}^{N} \omega_{ij} \xi_j(0) \right) \right] t \right\}^{1/2}, \quad (20)$$

since $\|\vec{w}_i(t)\| \propto t$ as $t \to \infty$. Therefore, **the normalized deviation vector** $\vec{w}_i(t)/\|\vec{w}_i(t)\|$ tends to **fall on the tangent space of the torus**, since its coordinates perpendicular to the torus vanish following a t^{-1} law.

Let us now study the case of k, general, linearly independent unit deviation vectors $\{\hat{w}_1, \hat{w}_2, \ldots, \hat{w}_k\}$ with $2 \leq k \leq 2N$. Using as vector basis the set $\{\hat{e}_1, \hat{e}_2, \ldots, \hat{e}_{2N}\}$ we get:

$$\begin{bmatrix} \hat{w}_1 & \hat{w}_2 & \ldots & \hat{w}_k \end{bmatrix}^{\mathrm{T}} = \mathbf{D}(t) \cdot \begin{bmatrix} \hat{e}_1 & \hat{e}_2 & \ldots & \hat{e}_{2N} \end{bmatrix}^{\mathrm{T}} \quad (21)$$

If *no* deviation vector is initially located in the tangent space of the torus, matrix **D** has the form

$$\mathbf{D}(t) = [d_{ij}] = \frac{1}{\prod_{m=1}^{k} \|\vec{w}_m(t)\|} \cdot \mathbf{D}^{0,k}(t). \quad (22)$$

where $i = 1, 2, \ldots, k$ and $j = 1, 2, \ldots, 2N$. Recalling our earlier discussion, the norm of vector $\vec{w}_i(t)$ for long times, grows linearly with t as

$$\|\vec{w}_i(t)\| \propto t. \tag{23}$$

Hence, the matrix **D** assumes the much simpler form

$$\mathbf{D}(t) = \frac{1}{t^k} \cdot \mathbf{D}^k(t). \tag{24}$$

The Case of N-Dimensional Tori

If k is lower than the dimension of the tangent space of the torus, i. e. $2 \leq k \leq N$, the fastest increasing determinants in this case are $\propto t^k$. Thus, we conclude that the contribution to the behavior of $GALI_k$ **is to provide constant terms**.
All other determinants introduce terms that **grow at a rate slower** than t^k, proportional to $t^{k-m}/t^k = 1/t^m$. So we arrive at the important result

$$\text{GALI}_k(t) \approx \text{constant} \quad \text{for} \ \ 2 \leq k \leq N. \tag{25}$$

In the important case of $N < k \leq 2N$ deviation vectors, the fastest growing determinants have the time evolution

$$Determinants \propto t^{2N-k}. \tag{26}$$

and contribute to the time evolution of $GALI_k$ terms proportional to

$$\mathsf{GALI}_k(t) \propto t^{2N-k}/t^k = 1/t^{2(k-N)}. \tag{27}$$

All other determinants introduce terms that tend to zero faster than $1/t^{2(k-N)}$.

The Case of Tori with Dimension Lower than N

In the case of an s–dimensional torus, the k deviation vectors eventually fall on its s–dimensional tangent space spanned by $\hat{e}_{N+1}, \ldots, \hat{e}_{N+s}$. If we start with $2 \leq k \leq s$ deviation vectors, the GALI_k indices will oscillate about **a nonzero constant**. However, for $s < k \leq 2N$ deviation vectors, some of them will become linearly dependent and the GALI_k will **tend to zero by a power law**.

Next, let us turn to the case of $s < k \leq 2N - s$. The fastest growing determinants are those containing the s columns of the matrix $\mathbf{D}^k$, having as many columns proportional to t as possible. Since t appears at most s times and GALI_k is proportional to $t^s / t^k = 1/t^{(k-s)}$, we conclude that $\text{GALI}_k(t) \sim t^{(s-k)}$ for $s < k \leq 2N - s$.

Finally, we consider the behavior of GALI_k when $2N - s < k \leq 2N$. The fastest growing determinants here have t appearing $2N - k$ times and the GALI_k is proportional to $t^{2N-k}/t^k = 1/t^{2(k-N)}$.
In conclusion, we have shown that **for chaotic orbits**:

$$\text{GALI}_k(t) \propto e^{-[(\sigma_1 - \sigma_2) + (\sigma_1 - \sigma_3) + \cdots + (\sigma_1 - \sigma_k)]t} . \tag{28}$$

while **for regular orbits lying on an s–dimensional torus**:

$$\text{GALI}_k(t) \sim \begin{cases} \text{constant} & \text{if } 2 \leq k \leq s \\ \dfrac{1}{t^{k-s}} & \text{if } s < k \leq 2N - s \\ \dfrac{1}{t^{2(k-N)}} & \text{if } 2N - s < k \leq 2N \end{cases} . \tag{29}$$

Fast Numerical Computation of the GALI$_k$ volumes:

We can write equations (7) in matrix form as:

$$
\begin{bmatrix} \hat{w}_1 \\ \hat{w}_2 \\ \vdots \\ \hat{w}_k \end{bmatrix} = \begin{bmatrix} w_{11} & w_{12} & \cdots & w_{1\,2N} \\ w_{21} & w_{22} & \cdots & w_{2\,2N} \\ \vdots & \vdots & & \vdots \\ w_{k1} & w_{k2} & \cdots & w_{k\,2N} \end{bmatrix} \cdot \begin{bmatrix} \hat{e}_1 \\ \hat{e}_2 \\ \vdots \\ \hat{e}_{2N} \end{bmatrix} = \mathbf{A} \cdot \begin{bmatrix} \hat{e}_1 \\ \hat{e}_2 \\ \vdots \\ \hat{e}_{2N} \end{bmatrix} . \tag{30}
$$

Since GALI$_k$ measures the volume of the k–parallelepiped P_k having as edges the k unitary deviation vectors $\hat{w}_i$, $i = 1, \ldots, k$, given by:

$$
\text{vol}(P_k) = \text{GALI}_k = \sqrt{\det(\mathbf{A} \cdot \mathbf{A}^{\mathrm{T}})} , \tag{31}
$$

(where $(^{\mathrm{T}})$ denotes transpose) and only the multiplication of two matrices and the square root of one determinant is required for its computation.

Numerical verification and applications

We shall use two examples with 2 (2D) and 3 (3D) degrees of freedom: the **2D Hénon–Heiles Hamiltonian**

$$H_2 = \frac{1}{2}(p_x^2 + p_y^2) + \frac{1}{2}(x^2 + y^2) + x^2 y - \frac{1}{3}y^3, \tag{32}$$

and **the 3D Hamiltonian system**:

$$H_3 = \sum_{i=1}^{3} \frac{\omega_i}{2}(q_i^2 + p_i^2) + q_1^2 q_2 + q_1^2 q_3, \tag{33}$$

for the parameters $H_2 = 0.125$ and $H_3 = 0.09$, with $\omega_1 = 1$, $\omega_2 = \sqrt{2}$ and $\omega_3 = \sqrt{3}$.

A 2D Hamiltonian system

Let us consider first **a chaotic orbit** of the 2D Hamiltonian (32), with initial conditions $x = 0$, $y = -0.25$, $p_x = 0.42$, $p_y = 0$. In the figure below, we see the time evolution of $L_1(t)$ of this orbit, which is a good approximation of the maximal LCE, σ_1. Actually, for $t \approx 10^5$, we find $\sigma_1 \approx 0.047$.
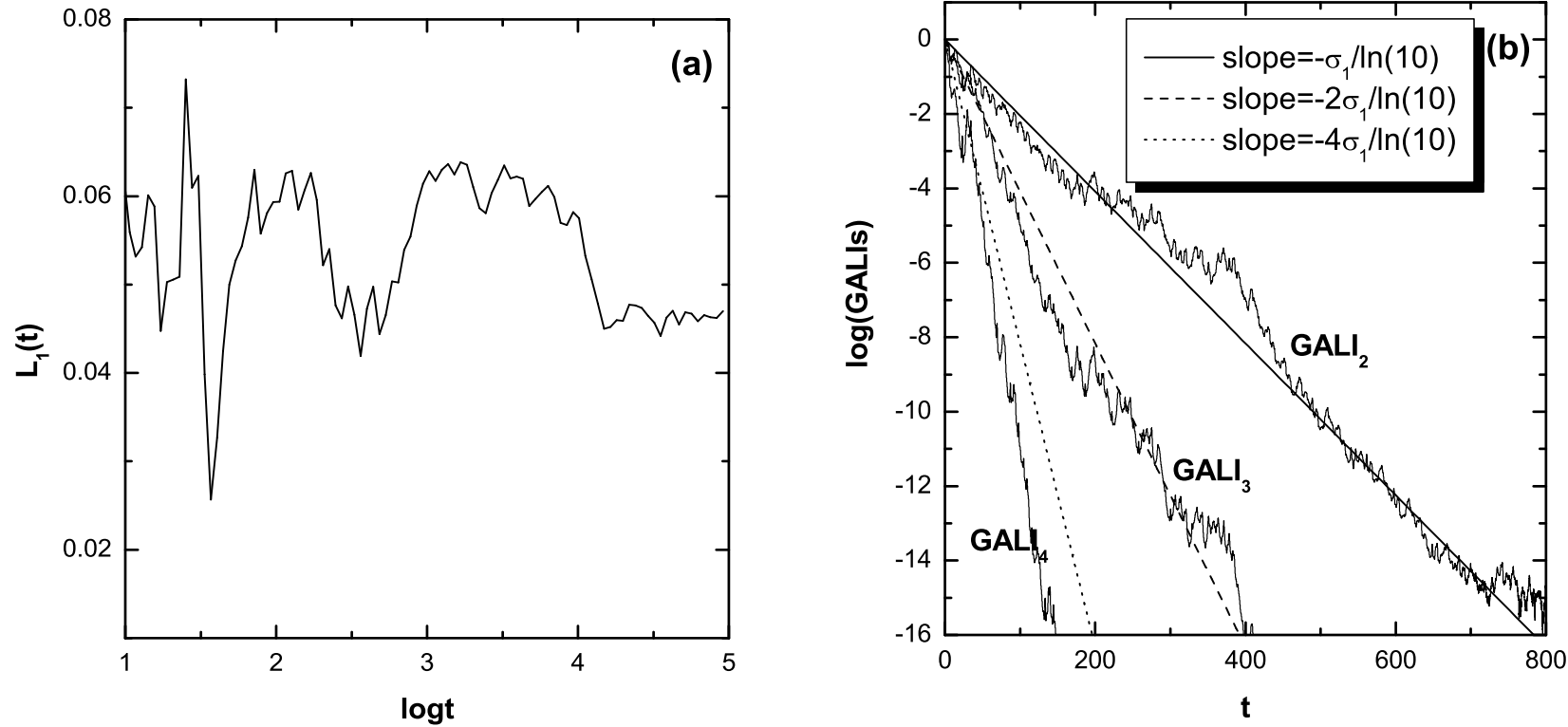
Figure 1:(a) $L_1(t)$ for **a chaotic orbit** of the 2D system. (b) The evolution of $GALI_2$, $GALI_3$ and $GALI_4$ for the same orbit. We find $\sigma_1 \approx 0.047$, and we know $\sigma_2 = 0$ and $\sigma_3 = -\sigma_2$ and $\sigma_4 = -\sigma_1$. So, $GALI_k$ behaves as

$$GALI_2(t) \propto e^{-\sigma_1 t}, \quad GALI_3(t) \propto e^{-2\sigma_1 t}, \quad GALI_4(t) \propto e^{-4\sigma_1 t}. \tag{34}$$

Now, **for an ordered orbit** of our 2D Hamiltonian and a random choice of initial deviation vectors, we expect the GALI indices to behave as

$$\text{GALI}_2(t) \propto \text{constant}, \quad \text{GALI}_3(t) \propto \frac{1}{t^2}, \quad \text{GALI}_4(t) \propto \frac{1}{t^4}. \tag{35}$$
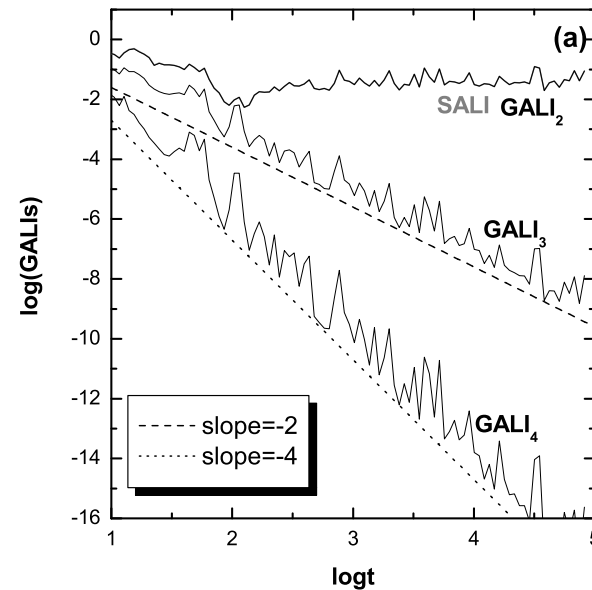
Figure 2: Time evolution of SALI (gray curves), GALI_2, GALI_3 and GALI_4 for an ordered orbit. Note that the curves of SALI and GALI_2 are very close to each other and thus cannot be distinguished. Dashed lines corresponding to particular power laws are also plotted.

A 3D Hamiltonian system

Let us now study the behavior of the GALIs in the case of the 3D Hamiltonian (33). The initial conditions of the orbits of this system are defined by assigning arbitrary values to the positions q_1, q_2, q_3, as well as the so–called 'harmonic energies' E_1, E_2, E_3 related to the momenta through $p_i = \sqrt{\frac{2E_i}{\omega_i}}$, $i = 1, 2, 3$.

Chaotic orbits of 3D Hamiltonian systems generally have **two positive Lyapunov exponents**, σ_1 and σ_2, while $\sigma_3 = 0$. So, for approximating the behavior of GALIs according to (41), both σ_1 and σ_2 are needed. In particular, (41) gives

$$\text{GALI}_2(t) \propto e^{-(\sigma_1 - \sigma_2)t}, \quad \text{GALI}_3(t) \propto e^{-(2\sigma_1 - \sigma_2)t}, \quad \text{GALI}_4(t) \propto e^{-(3\sigma_1 - \sigma_2)t},$$
$$\text{GALI}_5(t) \propto e^{-4\sigma_1 t}, \quad \text{GALI}_6(t) \propto e^{-6\sigma_1 t}. \tag{36}$$

Let us consider the chaotic orbit with initial conditions $q_1 = q_2 = q_3 = 0$, $E_1 = E_2 = E_3 = 0.03$ of the 3D system (33) and compute σ_1, σ_2 for this orbit. For $t \approx 10^5$ we find $\sigma_1 \approx 0.03$ and $\sigma_2 \approx 0.008$. Using these values as good approximations of σ_1, σ_2 we see that the slopes of all GALIs are well reproduced by the analytical formulas.
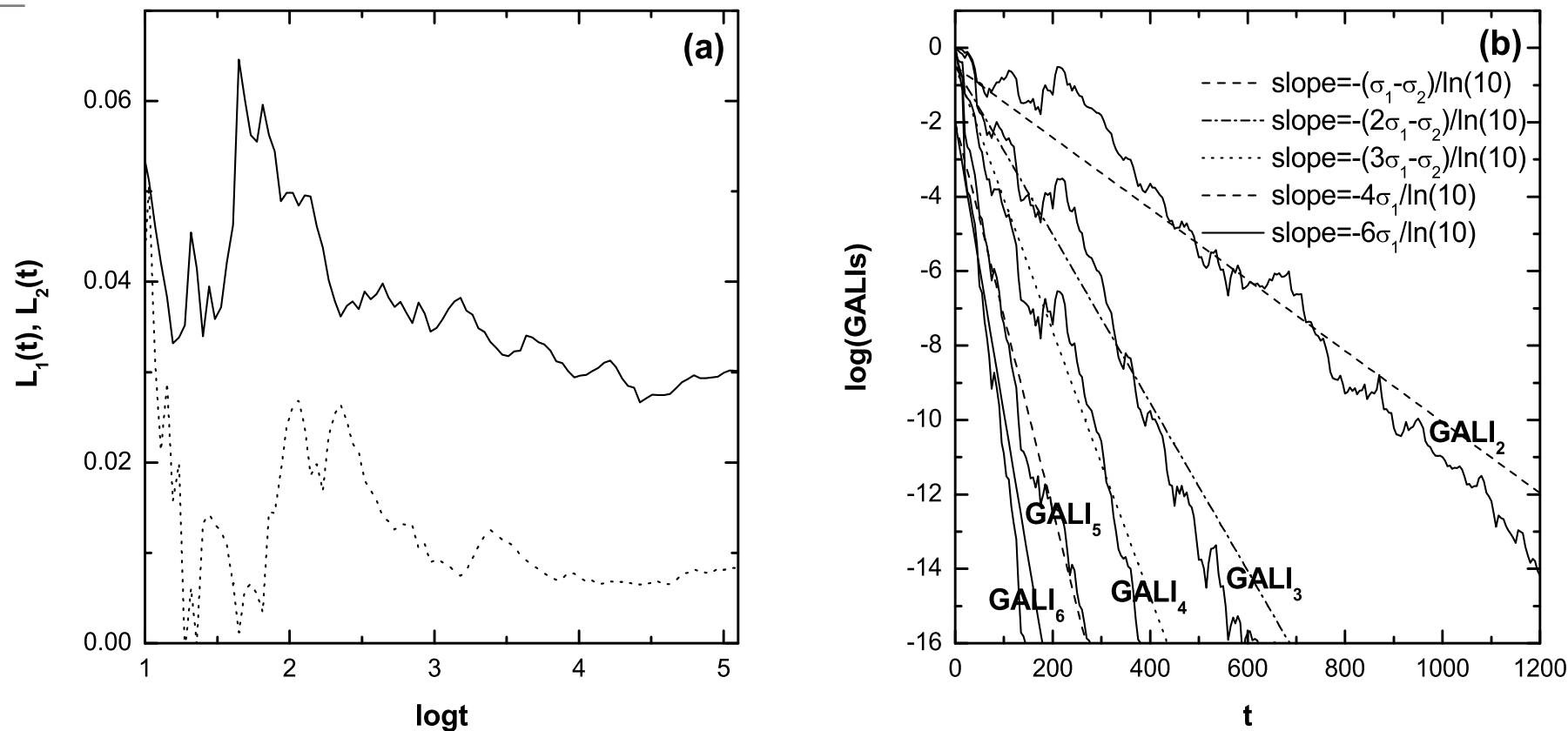
Figure 3: (a) The evolution of $L_1(t)$, $L_2(t)$ for the chaotic orbit of the 3D system. (b) The evolution of GALI$_k$ with $k = 2, \ldots, 6$. The plotted lines correspond to functions proportional to $e^{-(\sigma_1 - \sigma_2)t}$, $e^{-(2\sigma_1 - \sigma_2)t}$, $e^{-(3\sigma_1 - \sigma_2)t}$, $e^{-4\sigma_1 t}$ and $e^{-6\sigma_1 t}$ for $\sigma_1 = 0.03$, $\sigma_2 = 0.008$.

Next, we consider the case of **ordered orbits in our 3D Hamiltonian system**. In general, the GALIs should behave as: $\mathrm{GALI}_2(t) \propto$ constant, $\mathrm{GALI}_3(t) \propto$ constant, $\mathrm{GALI}_4(t) \propto \frac{1}{t^2}$, $\mathrm{GALI}_5(t) \propto \frac{1}{t^4}$, $\mathrm{GALI}_6(t) \propto \frac{1}{t^6}$.
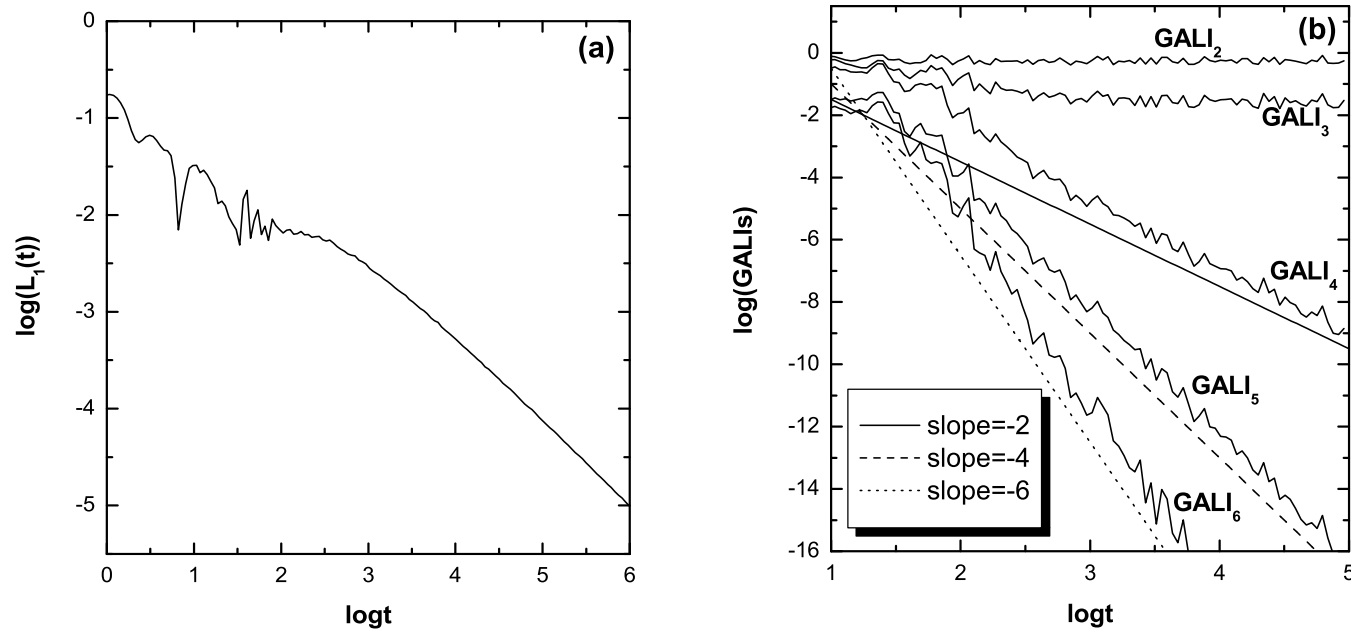
Figure 4: (a) $L_1(t)$ for the ordered orbit of the 3D system and (b) The GALI_k with $k = 2, \ldots, 6$ of the same orbit. The dashed lines are the slopes of $\frac{1}{t^2}$, $\frac{1}{t^4}$ and $\frac{1}{t^6}$.

Low - Dimensional Tori and Weak Diffusion

In their famous paper in 1955, Fermi, Pasta and Ulam studied **energy transport in one – dimensional lattices**, like the so – called β – FPU lattice described by the Hamiltonian

$$H = \frac{1}{2} \sum_{j=1}^{N} \dot{x}_j^2 + \sum_{j=0}^{N} \left(\frac{1}{2}(x_{j+1} - x_j)^2 + \frac{1}{4}\beta(x_{j+1} - x_j)^4 \right) = E \qquad (37)$$

When β is small, the dynamics can described by the linear normal modes

$$Q_k = \sqrt{\frac{2}{N+1}} \sum_{i=1}^{N} q_i \sin \frac{ki\pi}{N+1}, \qquad P_k = \dot{Q}_k \qquad (38)$$

with energies and ("phonon") frequencies

$$E_k = \frac{1}{2} \left[P_k^2 + \omega_k{}^2 Q_k^2 \right], \quad \omega_k = 2\sin \frac{k\pi}{2(N+1)} \qquad (39)$$

Fermi, Pasta and Ulam observed that, for low values of E, if the initial conditions are chosen such that one or more of the **low k - modes** ($k = 1, 2, 3, ..$) are excited, one observes the famous **FPU recurrences**!

This means that the energy returns periodically to the initial state, instead of leading to energy sharing and equipartition as expected from Statistical Mechanics. Let us see what the $GALI_k$ give when only the $k = 1$ and $k = 3$ modes modes are excited:
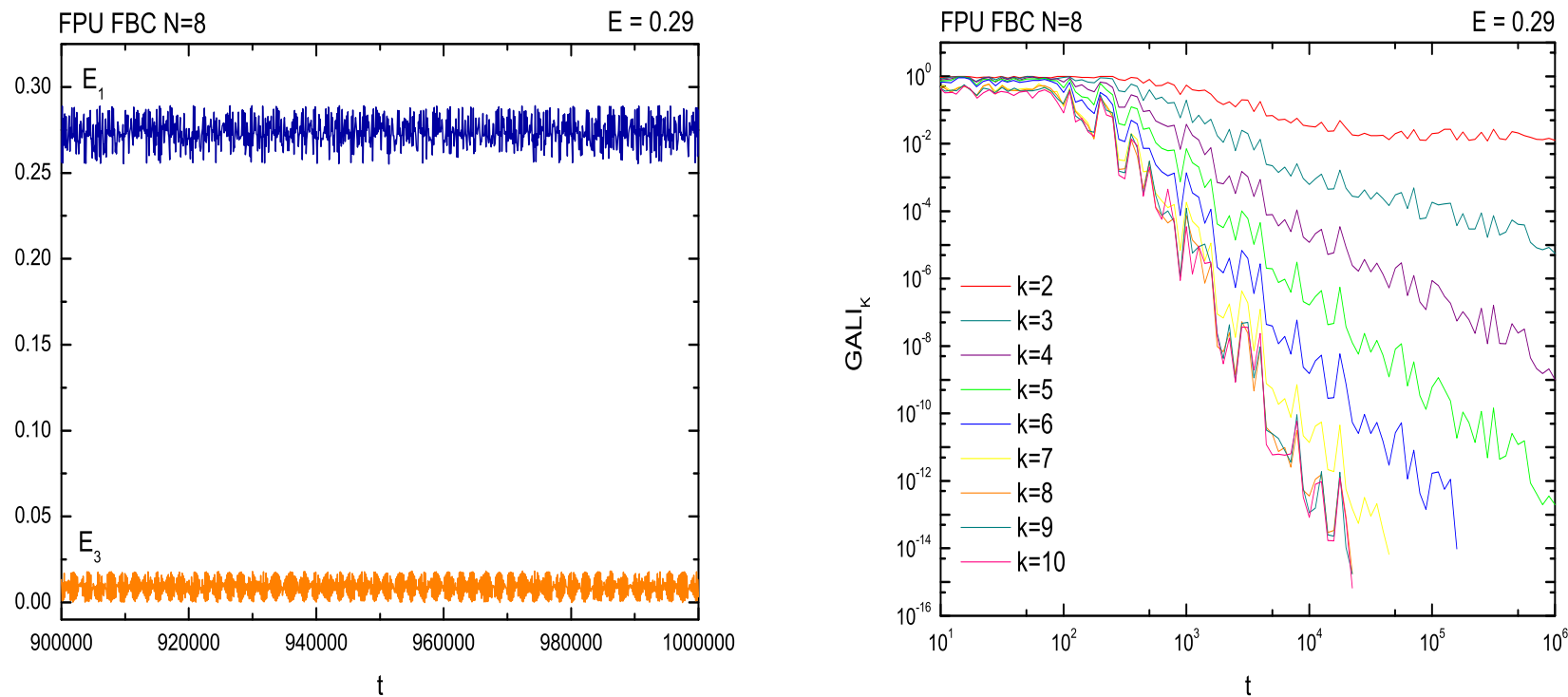
Figure 5: FPU with 8 particles:(a) Only the E_1 and E_3 modes are excited and the torus is 2-dimensional, since (b) only $GALI_2$=const. and all other $GALI_k$ decay by power laws.

Next we start by putting all the energy in the 4 modes $k = 1, 3, 5, 7$ and observe that the motion lies on a 4–dimensional torus
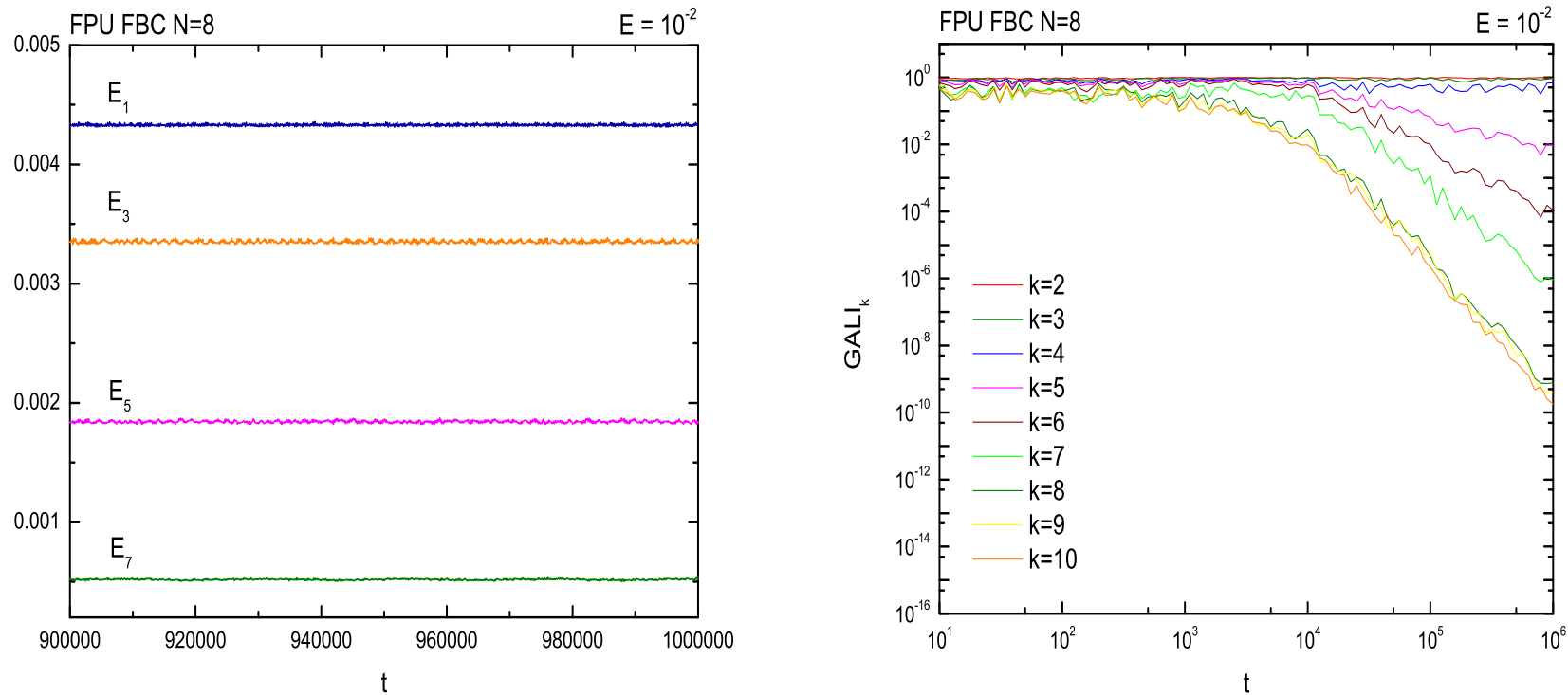
Figure 6: FPU with 8 particles:(a) When the E_1, E_3, E_5 and E_7 modes are excited the torus is 4-dimensional and (b) only the GALI$_k$=const. for $k = 2, 3, 4$, while all others, with $k = 5, \ldots, 10$ decay by power laws.

Finally we may put all energy in 8 modes and obtain a generic 8–dimensional torus:
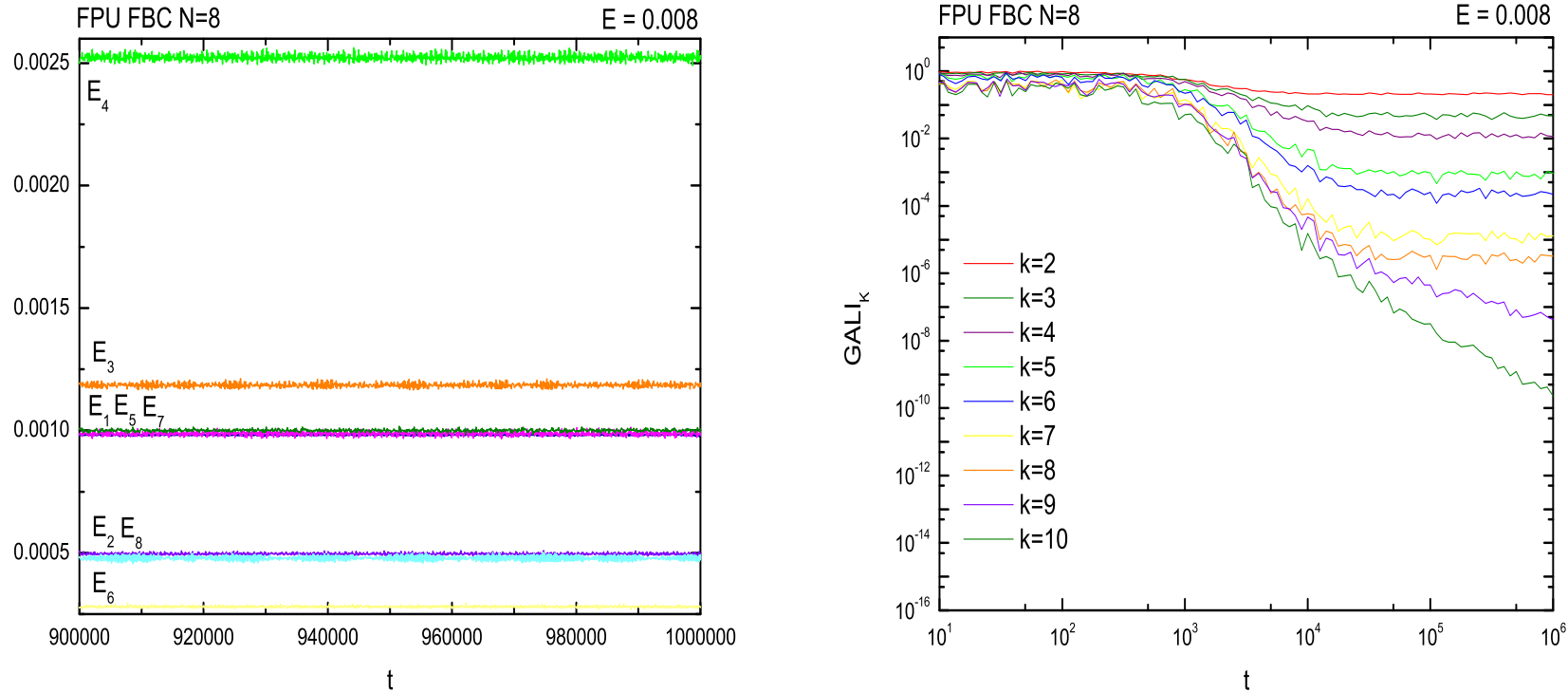
Figure 7: FPU with 8 particles:(a) When 8 modes, $k = 1, 2, ..., 8$, are excited the torus is 8-dimensional and (b) GALI$_k$=const.,for $k = 2, \dots, 8$, while the other two with $k = 9, 10$ decay by power laws.

Predicting the onset of weak diffusion

For initial conditions **slightly off a torus** leading to slow diffusive motion away from quasiperiodicity, $GALI_2$ predicts it quickly by falling to zero exponentially:
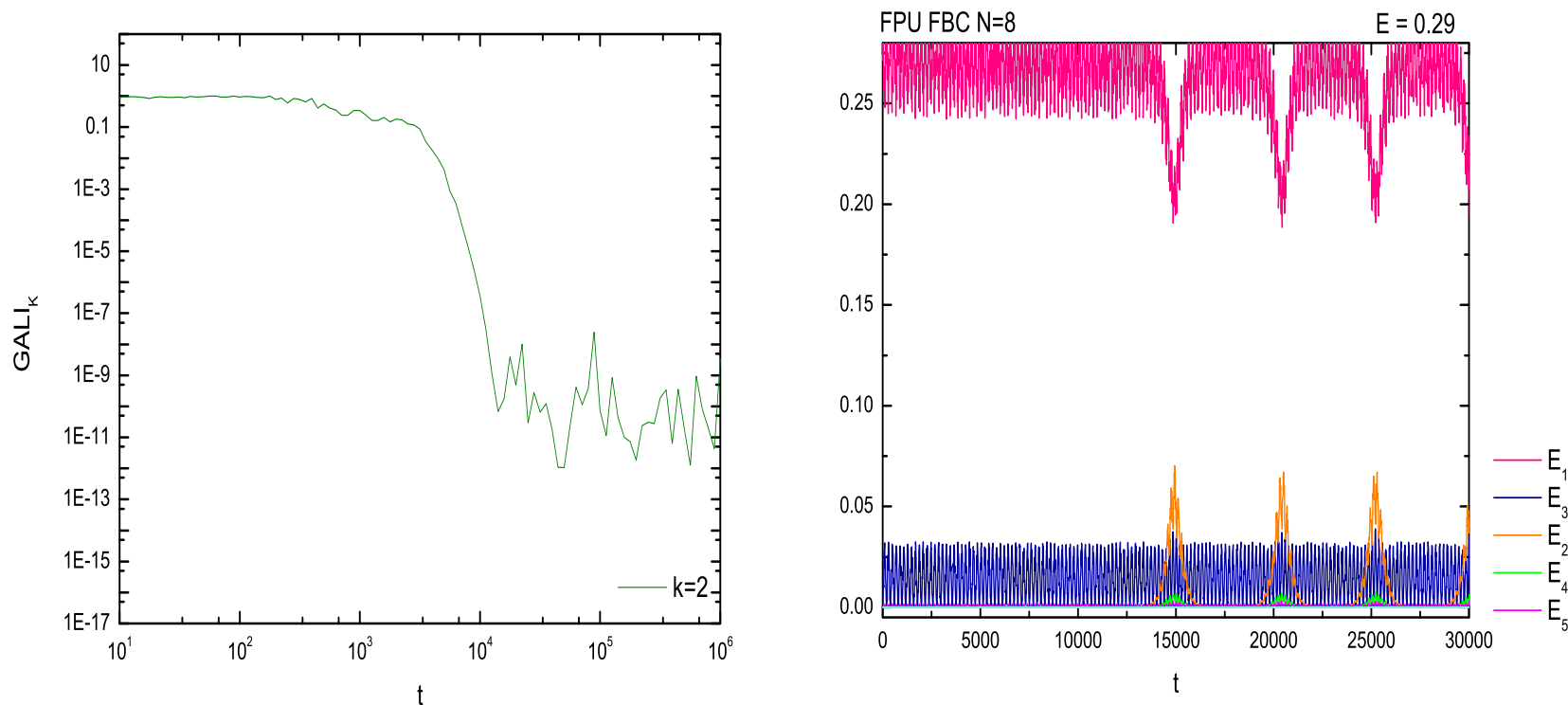
Figure 8: FPU with 8 particles:(a) The evolution of $GALI_2$ shows already at $t \approx 500$ that the orbit diffuses away from the torus and is not quasiperiodic. (b) This becomes visible in the oscillations **much later**, when the recurrences break down at $t \approx 14000$.
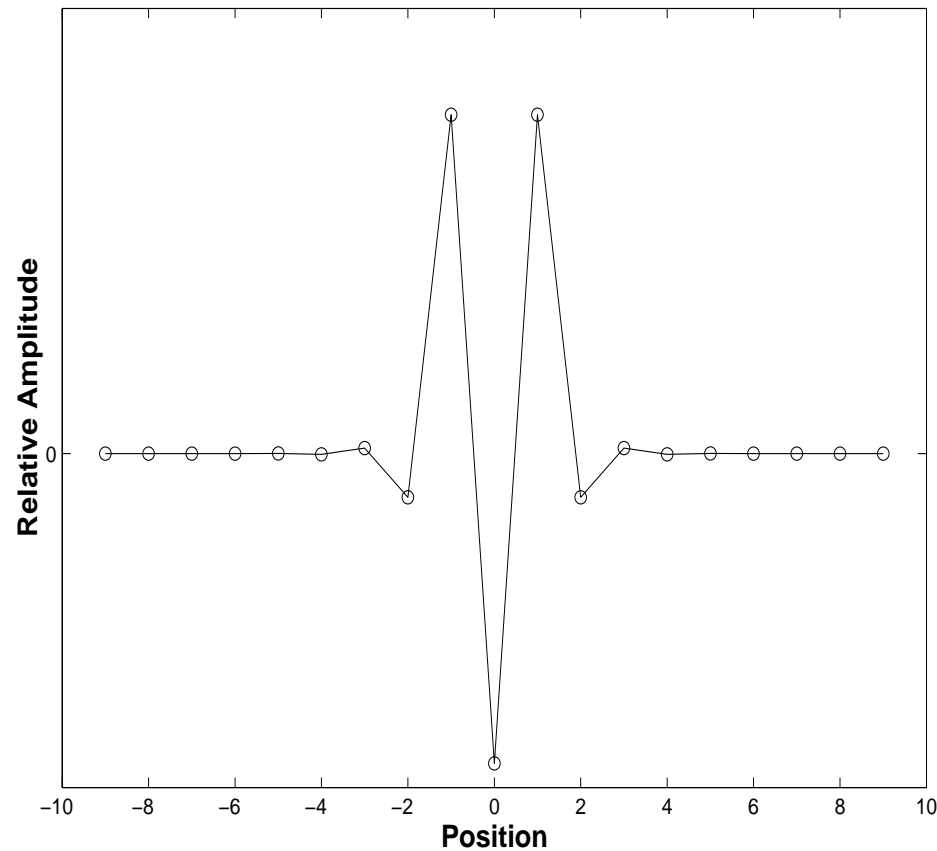
Figure 9. Let us now consider **discrete (periodic) breathers**, like the one above, representing **localization in configuration space**, in contrast to the FPU recurrences, which are **localized in Fourier space**.

Quasiperiodic Breathers and their Breakdown

Finally we study a quartic Hamiltonian lattice with on site quartic potential and no linear dispersion, described by the Hamiltonian

$$H_{NL} = \frac{1}{2} \sum_{i=1}^{N} p_i^2 + \sum_{i=1}^{N} \left[\frac{1}{2}(q_{i+1} - q_i)^4 + \frac{1}{2}q_i^2(1 - \epsilon cos(\omega_d t)) - \frac{1}{4}q_i^4 \right] \qquad (40)$$

with fixed boundary conditions, i.e. $q_0 = q_N = p_0 = p_N = 0$. We select parameter values at which we know that the Hamiltonian (40) has a stable **discrete breather**.

Now, around this (periodic) breather, due to the **absence of quadratic nearest neighbor interactions**–and hence no linear spectrum to generate resonances–**quasiperiodic breathers** exist. GALI$_2$ oscillates about a constant and thus identifies the presence of a torus. And since **all higher order** GALI$_k$, with $k > 2$, decay the torus is 2–dimensional!
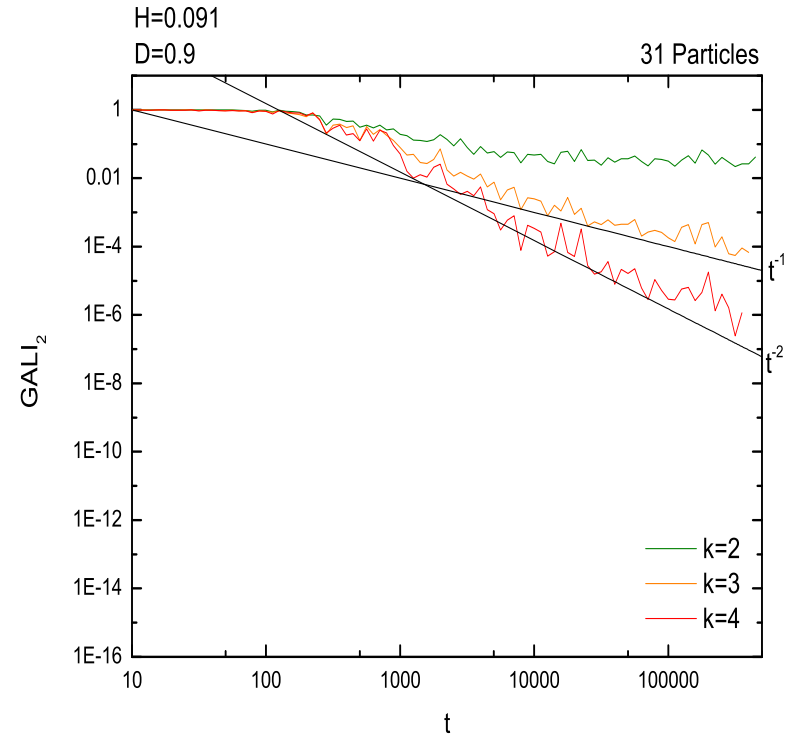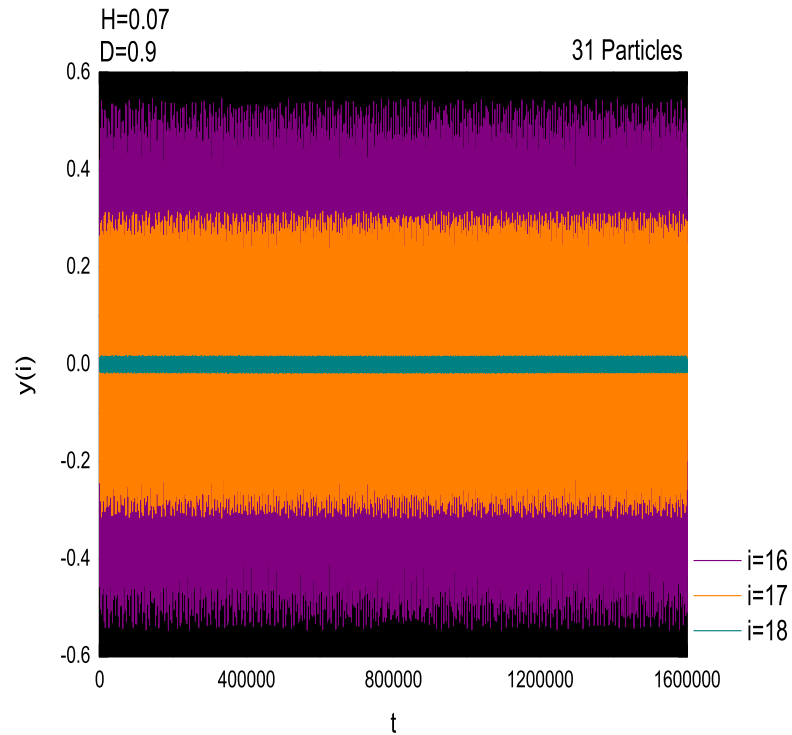
Figure 10:(a) The oscillations of the central three particles of this with $N = 31$ particles do **not break down**, forming a quasiperiodic breather. (b) The corresponding torus is 2–dimensional, as evidenced by the fact that only GALI$_2$ remains nearly constant, while all other GALI$_k$, with $k > 2$ decrease by power laws.

However, at initial conditions further away from the periodic breather, GALI$_2$ **predicts slow chaotic diffusion** by falling to zero exponentially:
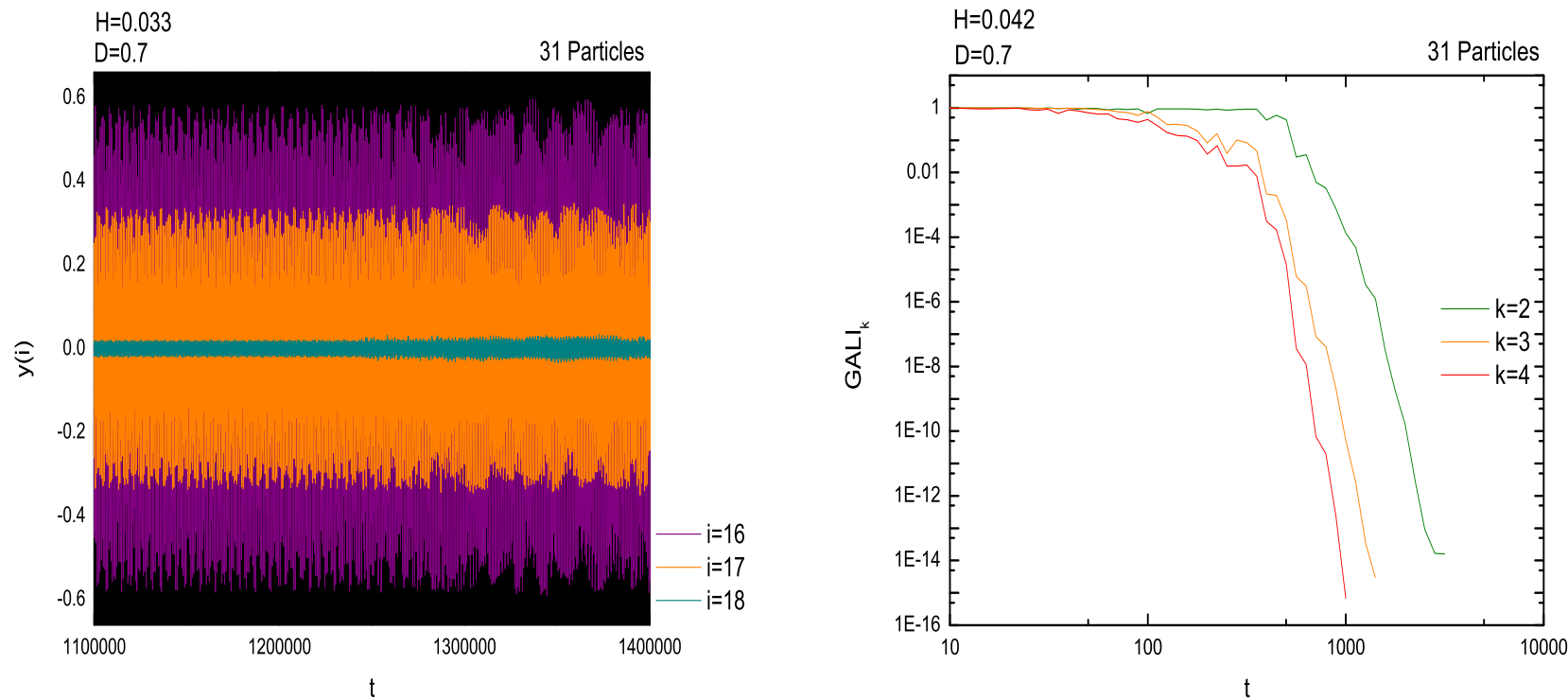
Figure 11:(a) The oscillations of the central particles of (40) with $N = 31$, **appear quasiperiodic** for very long times. (b) The solution, however, is **not on a torus and diffuses slowly away**, since even GALI$_2$ decays exponentially after about $t = 5000$.

Conclusions

1) We introduced the so-called **Generalized Alignment Indices**, GALI$_k$, where GALI$_k$ is the 'norm' of the 'exterior' or wedge product of k normalized deviation vectors and hence represents the 'volume' of a parallelepiped having as edges $k > 2$ initially independent deviation vectors.

We have shown that **for chaotic orbits**:

$$\text{GALI}_k(t) \propto e^{-[(\sigma_1 - \sigma_2) + (\sigma_1 - \sigma_3) + \cdots + (\sigma_1 - \sigma_k)]t} . \tag{41}$$

while **for ordered ones**:

$$\text{GALI}_k(t) \sim \begin{cases} \text{constant} & \text{if } 2 \leq k \leq s \\ \dfrac{1}{t^{k-s}} & \text{if } s < k \leq 2N - s \\ \dfrac{1}{t^{2(k-N)}} & \text{if } 2N - s < k \leq 2N \end{cases} . \tag{42}$$

where s is the dimension of the torus and no deviation vectors are initially tangent to the torus.

2) The GALI$_k$s has been successfully applied to:

a) Distinguish very rapidly **chaotic orbits**, for $2 \leq k \leq N$, **from ordered orbits** (GALI$_k$ decays exponentially or fluctuates around a constant)

b) Determine from the GALI$_k$ power law decays the **dimensionality $d \leq N$ of the subspace of ordered motion**, identifying **low - dimensional tori**

c) Locate initial conditions leading to **very slow diffusion** of the orbits toward a larger chaotic "sea", near nonlinear normal modes of the FPU lattice and quasiperiodic breathers.

c) Efficiently **chart large domains of phase space**, identifying various degrees of order and chaos, by different behaviors of the indices.

d) Obtain analogous results also for $2N$–dimensional **symplectic maps.**

References

1. Skokos, Ch. [2001], "Alignment Indices: A New, Simple Method for Determining the Ordered or Chaotic Nature of Orbits", *J. Phys. A*, **34**, pp. 10029 – 10043.

2. Skokos, Ch., Antonopoulos, Ch., Bountis, T. C. and Vrahatis, M. N. [2003], "How does the Smaller Alignment Index (SALI) Distinguish Order from Chaos?", *Prog. Theor. Phys. Supp.*, **150**, pp. 439 – 443

3. Skokos, Ch., Antonopoulos, Ch., Bountis, T. C. and Vrahatis, M. N. [2004], "Detecting Order and Chaos in Hamiltonian Systems by the SALI Method", *J. Phys. A*, **37**, pp. 6269 – 6284.

4. Antonopoulos, Ch., Bountis, T. C. and Skokos, Ch., [2006], "Chaotic Dynamics of N–Degree–of–Freedom Hamiltonian Systems", International Journal of Bifurcation and Chaos, vol.**16**(6), 1777-1793 , June 2006.

5. Antonopoulos, Ch. and Bountis, T., [2006], "Stability of Simple Periodic Orbits and Chaos in an FPU Lattice", PRE**73**, 056206, 1-8 (2006).

6. T. Bountis, "Stability of Motion: From Lyapunov to N - Degree of Freedom Hamiltonian Systems", [2006], "Nonlinear Phenomena and Complex Systems", vol. **9**(3) ,209 -239, 2006.

7. Skokos, Ch., Bountis, T. and Antonopoulos, Ch. [2007], "Geometrical properties of local dynamics in Hamiltonian systems: the Generalized Alignment Index (GALI) method", Physica D **231**, 30.

COMPLEX HAMILTONIAN DYNAMICS AND STATISTICS

Tassos BOUNTIS

Work with Chris Antonopoulos, Vassilis Basios and Thanos Manos

Department of Mathematics and Center for Research and Applications of Nonlinear Systems (CRANS), University of Patras, GR–26500, Rion, Patras, Greece

Lecture 3:

Complex Statistics at the Edge of Chaos:

Applications to Statistical Mechanics and Galactic Dynamics

Workshop and Latin–American School on "Foundations of Complexity"

Rio de Janeiro, Brasil, October 4–30, 2015

Complex Hamiltonian Dynamics

Tassos Bountis and Haris Skokos
Springer Synergetics series, April 2012

Foreword by Sergej Flach

Contents

Sums of Random Variables and the Central Limit Theorem

The approach we shall follow is in the spirit of the Central Limit Theorem (CLT). In particular, we focus on chaotic regions of: (a) **area–preserving maps**

$$
\begin{cases}
x_{n+1} = f(x_n, y_n) \\
y_{n+1} = g(x_n, y_n)
\end{cases}
\tag{1}
$$

and (b) N**–degree–of–freedom Hamiltonian systems**

$$
\frac{dq_k}{dt} = \frac{\partial H}{\partial p_k}, \quad \frac{dp_k}{dt} = -\frac{\partial H}{\partial q_k}, \quad k = 1, 2, \ldots, N
\tag{2}
$$

and construct **distributions** of rescaled sums of M values of an observable $\eta_i = \eta(t_i)$, $i = 1, \ldots, M$, which is a linear combination of the variables (x_n, y_n), or $(q_n(t), p_n(t))$ of the problem. These are viewed as **independent random variables** in the **limit of large** $M(\to \infty)$ and we evaluate **their sums** for a **large number** N_{ic} of initial conditions:

$$
S_M^{(j)} = \sum_{i=1}^{M} \eta_i^{(j)}, \quad j = 1, \ldots, N_{\text{ic}}
\tag{3}
$$

We then study the **probability density functions (pdfs)** of the variables $S_M^{(j)}$, centered about their **mean value** $\langle S_M^{(j)} \rangle$ and rescaled by their **standard deviation** σ_M

$$s_M^{(j)} \equiv \frac{1}{\sigma_M}\left(S_M^{(j)} - \langle S_M^{(j)} \rangle\right) = \frac{1}{\sigma_M}\left(\sum_{i=1}^{M} \eta_i^{(j)} - \frac{1}{N_{\text{ic}}}\sum_{j=1}^{N_{\text{ic}}}\sum_{i=1}^{M} \eta_i^{(j)}\right) \tag{4}$$

where

$$\sigma_M^2 = \frac{1}{N_{\text{ic}}}\sum_{j=1}^{N_{\text{ic}}}\left(S_M^{(j)} - \langle S_M^{(j)} \rangle\right)^2 = \langle S_M^{(j)2} \rangle - \langle S_M^{(j)} \rangle^2. \tag{5}$$

If our variables are **random**, or **belong to uniformly ergodic regimes of deterministic systems**, when we plot the normalized distribution of probabilities $P(s_M^{(j)})$ as a function of $s_M^{(j)}$, , we expect to find **in the spirit of the classical CLT**:

$$P(s_M^{(j)}) = a e^{-\beta s_M^{(j)2}} \tag{6}$$

i.e a **Gaussian pdf**.

However, in regimes of **"weak chaos"** of many **conservative systems**, these distributions are well–approximated by different pdfs, the most ubiquitous of them being the q-**Gaussian**:

$$P(s_M^{(j)}) = ae_q^{-\beta s_M^{(j)2}} \equiv a\left(1 - (1-q)\beta s_M^{(j)2}\right)^{\frac{1}{1-q}} \tag{7}$$

where q is the **Tsallis entropy index**, β is **a free parameter** and a **a normalization constant**. Expression (7) is a generalization of the Gaussian, since in the limit $q \to 1$ we have $lim_{q\to1}e_q^{-\beta x^2} = e^{-\beta x^2}$. If $1 \leq q < 3$, (7) is normalized for an appropriate choice of $a(\beta)$.

As we shall demonstrate, there are **many interesting cases of conservative systems**, where chaotic orbits are strongly influenced by **"stickiness" phenomena** and produce **long–lived quasi–stationary states** (QSS), whose pdfs are well–approximated by q–Gaussians. These, however, **do not always converge to a q gaussian, but evolve, through a sequence of QSS**, which we seek to identify the limit $t \to \infty$.

Nonextensive Statistical Mechanics and q-Gaussians

Multi–particle systems belong to **different "universality" classes**, according to their thermostatistics. In the most widely studied **Boltzmann–Gibbs class**, if the system can be at any one of $i = 1, 2, ..., W$ states with probability p_i, its entropy is given by the famous formula

$$S_{BG} = -k \sum_{i=1}^{W} p_i ln p_i \tag{8}$$

where k is Boltzmann's constant, provided, of course,

$$\sum_{i=1}^{W} p_i = 1 \tag{9}$$

The BG entropy satisfies the property of **additivity**, i.e. if A and B are two statistically independent systems, the probability to be in their union is $p_{i,j}^{A+B} = p_i^A p_j^B$ and this necessitates that the entropy of the joint state obey

$$S_{BG}(A + B) = S_{BG}(A) + S_{BG}(B) \tag{10}$$

At thermal equilibrium, the p_i **that optimize the BG entropy**, subject to ((9)) and a given energy spectrum E_i and temperature T are:

$$p_i = \frac{e^{-\beta E_i}}{Z_{BG}}, \quad Z_{BG} = \sum_{i=1}^{W} e^{-\beta E_i} \tag{11}$$

where $\beta = 1/kT$ and Z_{BG} is the so–called partition function. For a **continuum set of states depending on one variable**, x, the optimal probability density function (pdf) corresponding to BG statistics subject to ((9)), zero mean and given variance V is, of course, the well–known Gaussian $p(x) = e^{-x^2/2V}/\sqrt{2V}$.

Another important property of the BG entropy is that it is **extensive**,

$$lim_{N \to \infty} \frac{S_{BG}}{N} < \infty \tag{12}$$

i.e. it grows **linearly** as a function of the number of degrees of freedom N of the system. But then, what about **many physically important systems** that are **not extensive**?

There are **many examples of non–extensive systems**, like: **self–gravitating systems of finitely many mass points**, interacting black holes, ferromagnetic models, systems with **long range forces**, in which **strong correlations and power laws** are dominant.

In deterministic dynamics, for instance, **chaos does not always mean exponential instability**, as there are regimes of **"weak chaos"**, where "stickiness phenomena" occur **on or near the boundary** of regions of regular motion called **'edge of chaos'**, where **Lyapunov exponents are zero** and orbits separate linearly from each other.

It is for these type of situations that Tsallis proposed a different form of entropy [Tsallis,2009]

$$S_q = k\frac{1 - \sum_{i=1}^{W} p_i^q}{q - 1} \text{ with } \sum_{i=1}^{W} p_i = 1 \tag{13}$$

depending on an index q, where $i = 1, \ldots, W$ counts the microstates of the system occurring with probability p_i and k is the Boltzmann constant.

Just as the Gaussian distribution represents an **extremal of the BG entropy** ((8)), so is the q–**Gaussian pdf** obtained as a **maximum** (for $q > 0$) or a **minimum** (q<0) of the Tsallis entropy ((13)).

$$p(x) = ae_q^{-\beta x^2} \equiv a\left(1 - (1-q)\beta x^2\right)^{\frac{1}{1-q}} \tag{14}$$

for a continuum set of states.

The Tsallis entropy is **not additive**, as

$$S_q(A+B) = S_q(A) + S_q(B) + k(1-q)S_q(A)S_q(B) \tag{15}$$

and **is in general not extensive**. It thus offers the possibility of studying cases where the A, B subsystems mentioned above are strongly correlated.

Systems characterized by these properties are said to have **complex statistics**, which is significantly different from BG systems.

Nonextensive Thermodynamics

If we have a discrete set of states $j = 1, 2, ..., W$, we define the escort probabilities

$$P_i = \frac{p_i^q}{\sum_{j=1}^{W} p_j^q} \tag{16}$$

Given the constraints (9) and

$$< E_i >_q = \sum_{j=1}^{W} P_i E_i = U_q \tag{17}$$

we find that **the distribution that extremizes the Tsallis entropy** S_q is the q-Gaussian

$$p_i = \frac{e_q^{-\beta_q(E_i - U_q)}}{\tilde{Z}_q} \tag{18}$$

where the partition function $\tilde{Z}_q$ is given by

$$\tilde{Z}_q = \sum_{i=1}^{W} e_q^{-\beta_q(E_i - U_q)} \tag{19}$$

and β_q is the Lagrange multiplier associated with constraint (11)

$$\beta_q = \frac{\beta}{\sum_{j=1}^{W} p_j^q} \tag{20}$$

From the above one can prove that **the fundamental thermodynamical equations have the same form as the corresponding BG expressions with all variables indexed by** q, and $\beta = 1/kT$:

$$S_q = k ln_q \tilde{Z}_q, \quad \frac{1}{T} = \frac{\partial S_q}{\partial U_q}, \quad F_q = U_q - TS_q = -\frac{1}{T} ln_q Z_q \tag{21}$$

and $ln Z_q = ln \tilde{Z}_q - \beta U_q$.

Pdfs of Chaotic States in Area–Preserving maps

Consider the perturbed MacMillan map, which occurs in the study of equilibrium configurations of Ablowitz–Ladik Discrete Nonlinear Schrodinger Equations:

$$
\begin{cases}
x_{n+1} = y_n \\
y_{n+1} = -x_n + 2\mu \frac{y_n}{1+y_n^2} + \epsilon y_n
\end{cases}
\tag{22}
$$

with parameters ϵ, μ. Since its Jacobian is 1, (22) is area-preserving.

We have analyzed the histogram of their normalized sums for a range of parameters (ϵ, μ) and have identified some generic classes of q-**Gaussians**, **exponentials**, $\sim e^{-k|z|}$ or **Gaussians**. Monitoring their time evolution for increasing number of iterations N, we observe the occurrence of different QSS, which we present with the corresponding phase space plots in the Figures below.

ϵ	0.2	0.5	0.9	1.2	1.6	1.8
L_{max}	0.0867	0.082	0.0875	0.0513	0.0495	0.05876

Table 1: Maximal Lyapunov exponents for $\mu = 0.6$ and $\epsilon = 0.2, 0.5, 0.9, 1.2, 1.6, 1.8$.
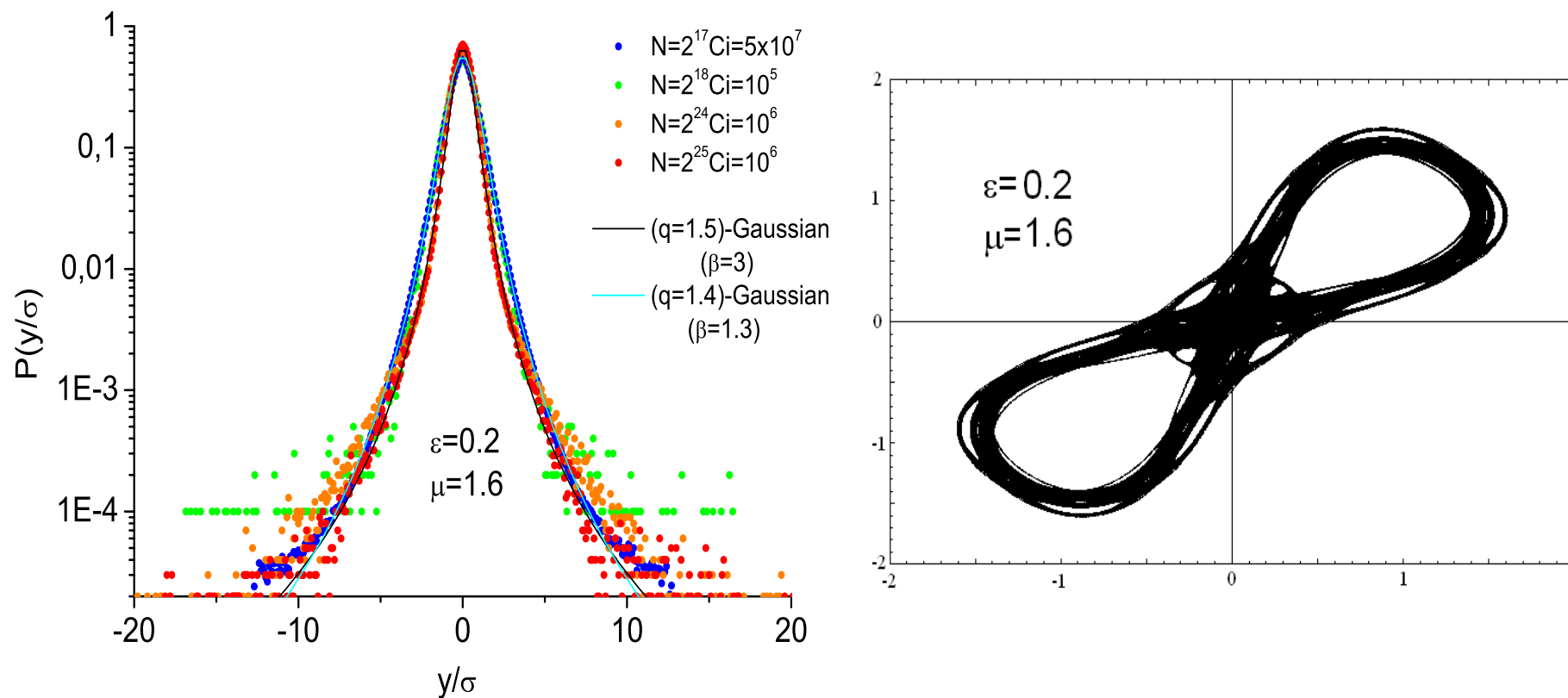
Figure 1. Tendency away from a Gaussian: Dynamical and statistical behavior of chaotic orbits of the MacMillan map for parameter values $\mu = 1.6$, and $\epsilon = 0.2$. Left: The pdfs of the normalized sums of iterates. Right: The corresponding phase space plot. N is the number of iterates and N_{ic} is the number of initial conditions randomly chosen from a square $(0, 10^{-6}) \times (0, 10^{-6})$.
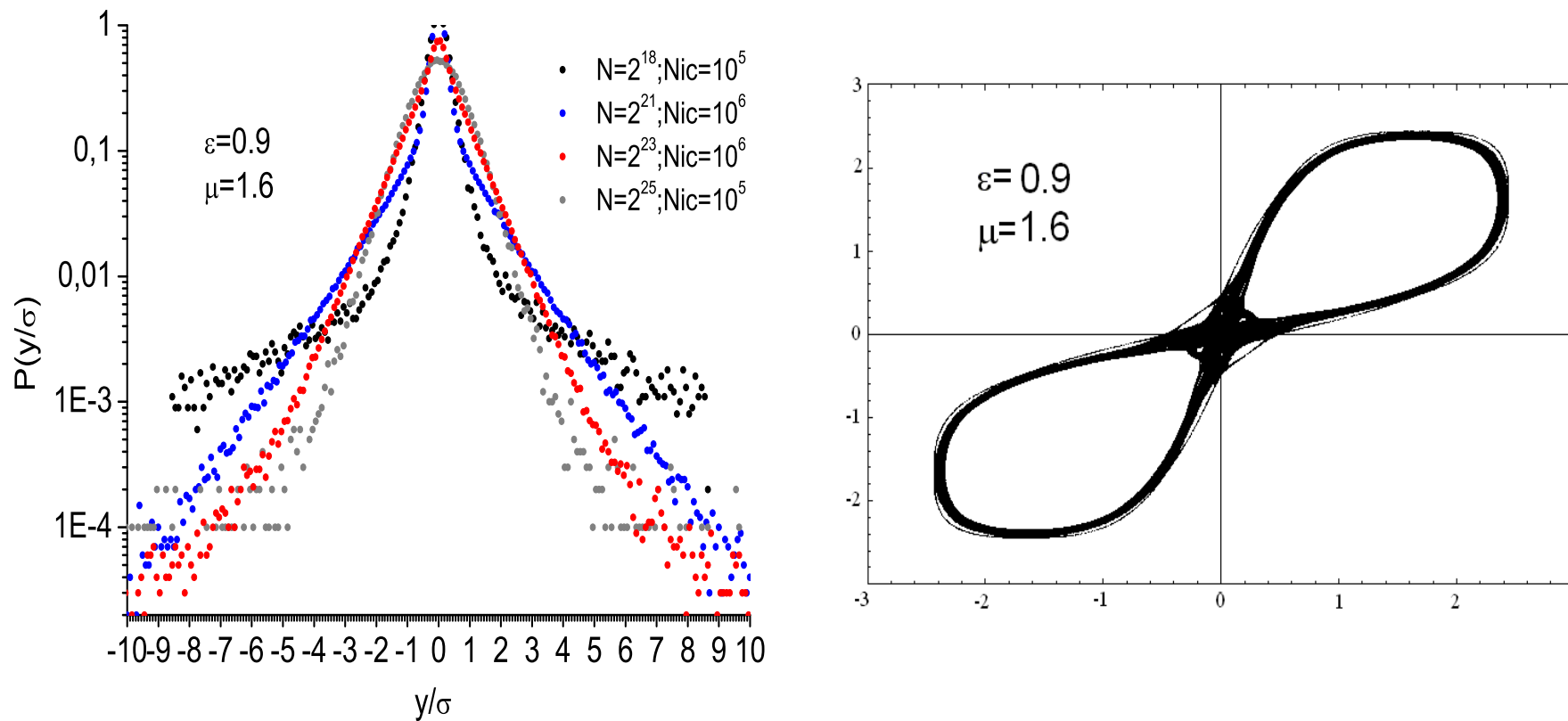
Figure 2. Tendency towards a Gaussian: Dynamical and statistical behavior of chaotic orbits of the MacMillan map for parameter values $\mu = 1.6$, and $\epsilon = 0.9$. Left: The pdfs of the normalized sums of iterates. Right: The corresponding phase space plot. N represents the number of (summed) iterates and N_{ic} is the number of initial conditions randomly chosen from a square $(0, 10^{-6}) \times (0, 10^{-6})$.

A. The $\epsilon = 0.9$, ($\mu = 1.6$) case: Towards a Gaussian

The $\epsilon = 0.9$ case is a typical example producing time–evolving pdfs. Figures 1 shows that the corresponding phase space plots yield a simple chaotic region in phase space around two islands, yet the corresponding pdfs do not converge to a single distribution, rather they pass from q-**Gaussians** to **triangular** to **Gaussian** distributions.

There exist at least **three long–lived QSS** whose iterates generate pdfs passing through different shapes. Consequently, for $i = 1 \ldots N = 2^{16}$, a QSS is produced whose pdf is a $(q = 1.6)$–Gaussian whose β increases with increasing N. This is most likely due to a **"stickiness"** effect around islands of regular motion.

Figures 3 and 4 below show phase space plots for a number of iterates N. Note that for $N = 1 \ldots 2^{16}$, a 'figure eight' chaotic region is formed around two islands. But for $N > 2^{16}$, a more complex structure emerges, as iterates stick around new islands, and **phase space statistics passes through a sequence of quasi-stationary states.**
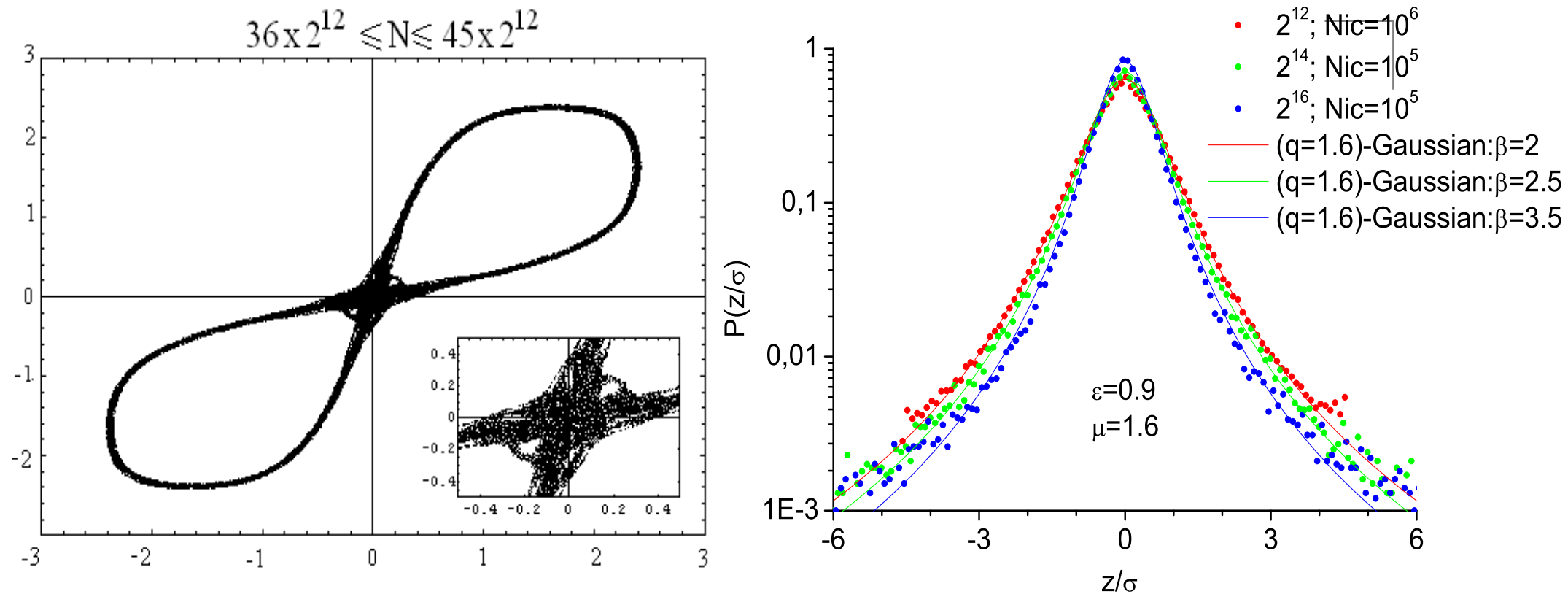
Figure 3. $\epsilon = 0.9$, $\mu = 1.6$ MacMillan map phase space plots (first panel) and the corresponding PDFs (second panel) of the re-normalized sums as the number of iterates $i = 1 \ldots N$, $N \leq 10^{16}$ increases, starting from a randomly chosen initial condition in a square $(0, 10^{-6}) \times (0, 10^{-6})$.
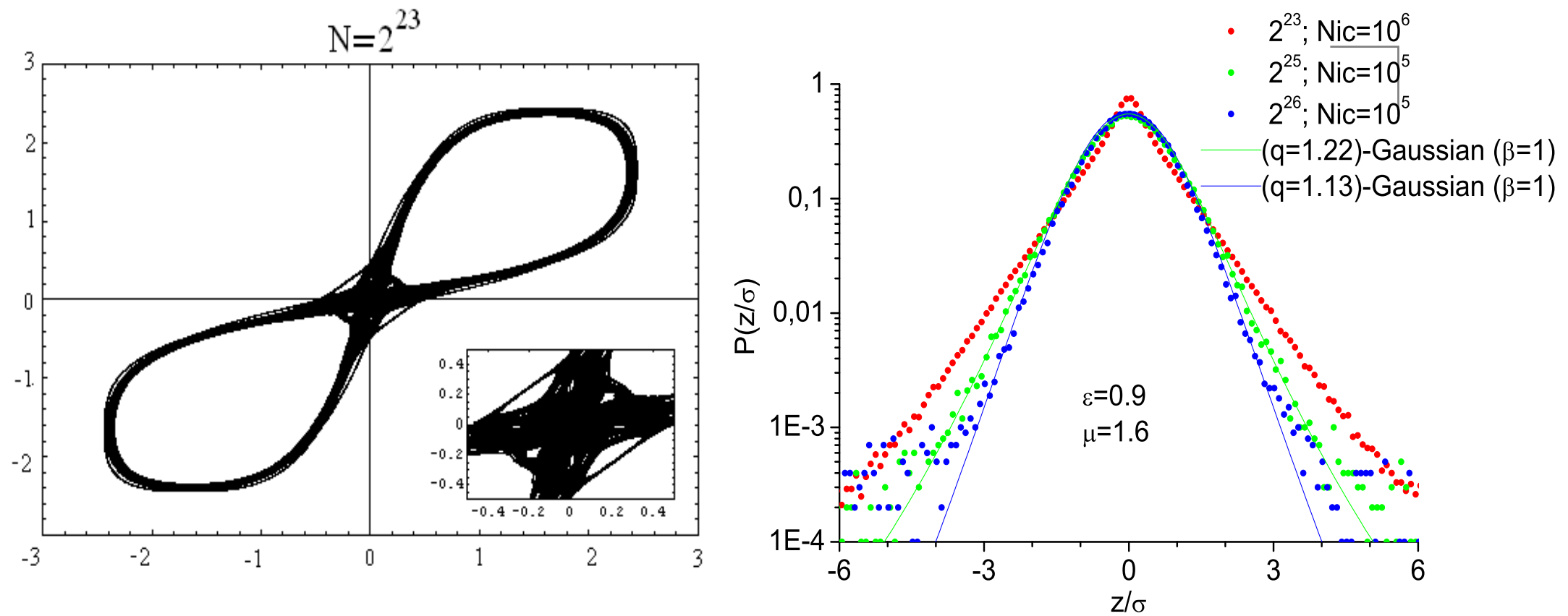
Figure 4. $\epsilon = 0.9$, $\mu = 1.6$ MacMillan map phase space for $i = 1 \ldots N, N \geq 2^{23}$ plot iterates, starting from a randomly chosen initial condition in a square $(0, 10^{-6}) \times (0, 10^{-6})$ and the corresponding pdfs (right panel).

Thus, more than one QSS coexist whose pdfs form a sequence of different $(q \neq 1)$–Gaussians. As we see in Figure 3 that this sequence of QSS for $N \leq 2^{21}$ produces a distribution where central part is still well–described by a $(q = 1.6)$–**Gaussian**.

However, as we continue to iterate the map to $N = 2^{23}$, this $(q = 1.6)$–Gaussian passes through a superposition of states characterized by **triangular distributions**. From here on, as $N > 2^{23}$, the central part of the pdfs become q–Gaussians with $q \to 1$ (see Figure 4) and a true **Gaussian** is expected in the limit $(N \to \infty)$.

B. The $\epsilon = 1.2$, ($\mu = 1.6$) cases: Towards a q Gaussian

Let us now analyze the cases $\epsilon = 1.2$, whose maximum Lyapunov exponent is $L_{max} \approx 0.05$. In Figure 5 iterates show a **diffusive behavior** that spreads around islands of a higher order resonance, as iterations reach $N = 2^{19}$.

The central part of the pdfs **converges to a** $(q = 1.6)$–**Gaussian** for $N \leq 2^{16}$ (left panel of Fig. 5). Then, orbits diffuse outward and even the tail of the pdf converges to a $(q = 1.6)$-Gaussian (right panel of Fig. 5). For larger N, diffusion ceases at the q–Gaussian of Figure 6.
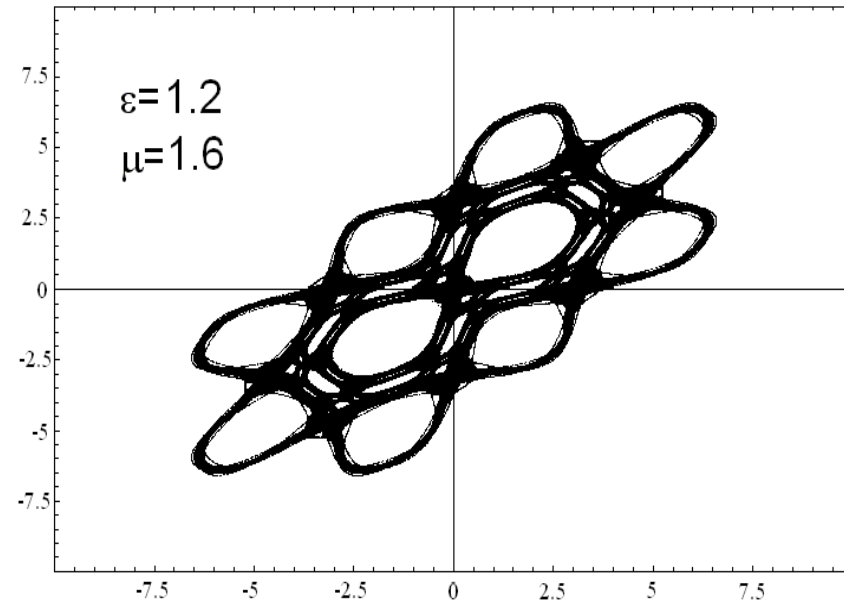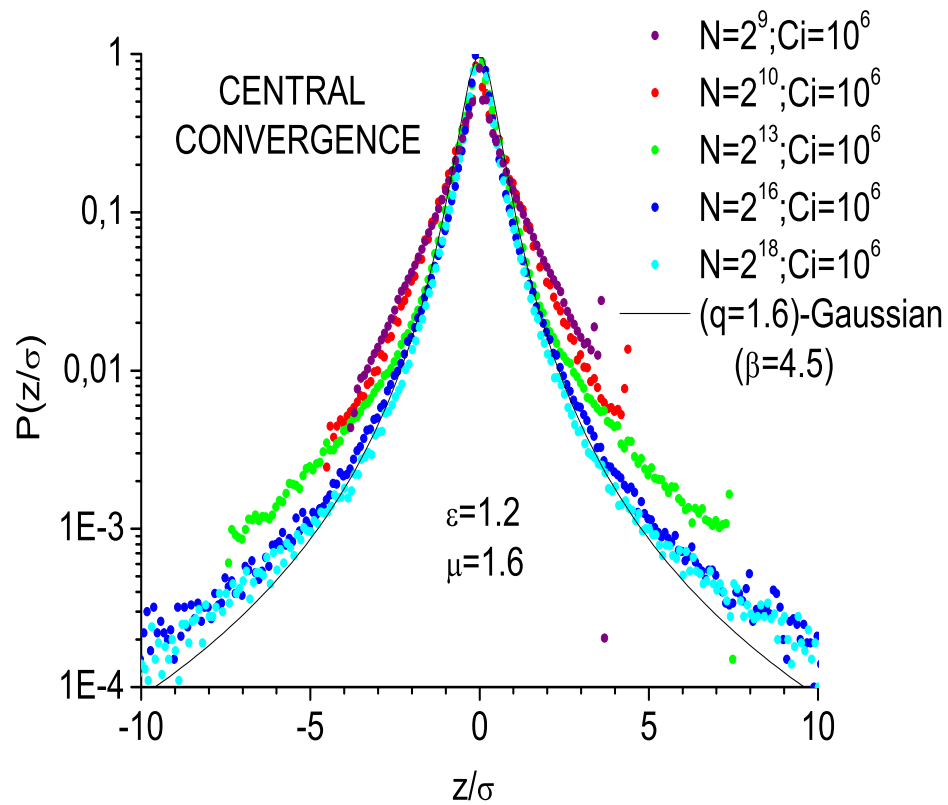
Figure 5. Dynamical and statistical behavior of chaotic orbits of the MacMillan map for $\mu = 1.6$, and $\epsilon = 1.2$. On the right the phase space plot and on the left the pdfs of the normalized sums of iterates.
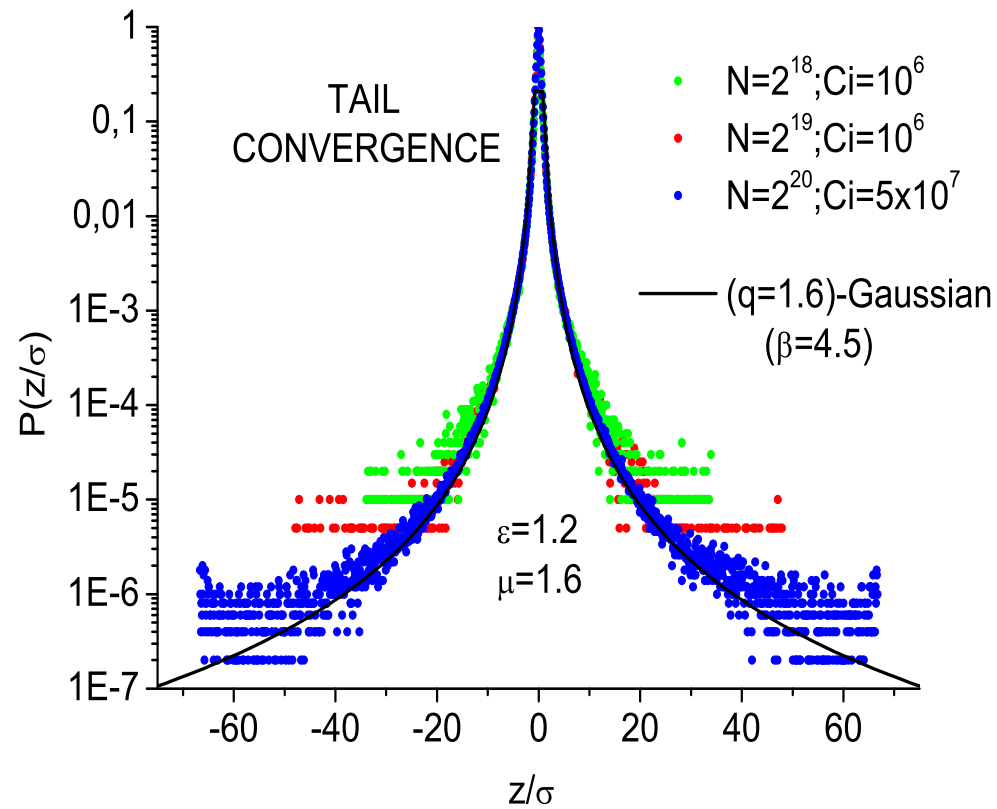
Figure 6. Tail convergence of the q–Gaussian for $\mu = 1.6$, and $\epsilon = 1.2$ depicting the pdfs for $N > 2^{18}$ numbers of iterates.
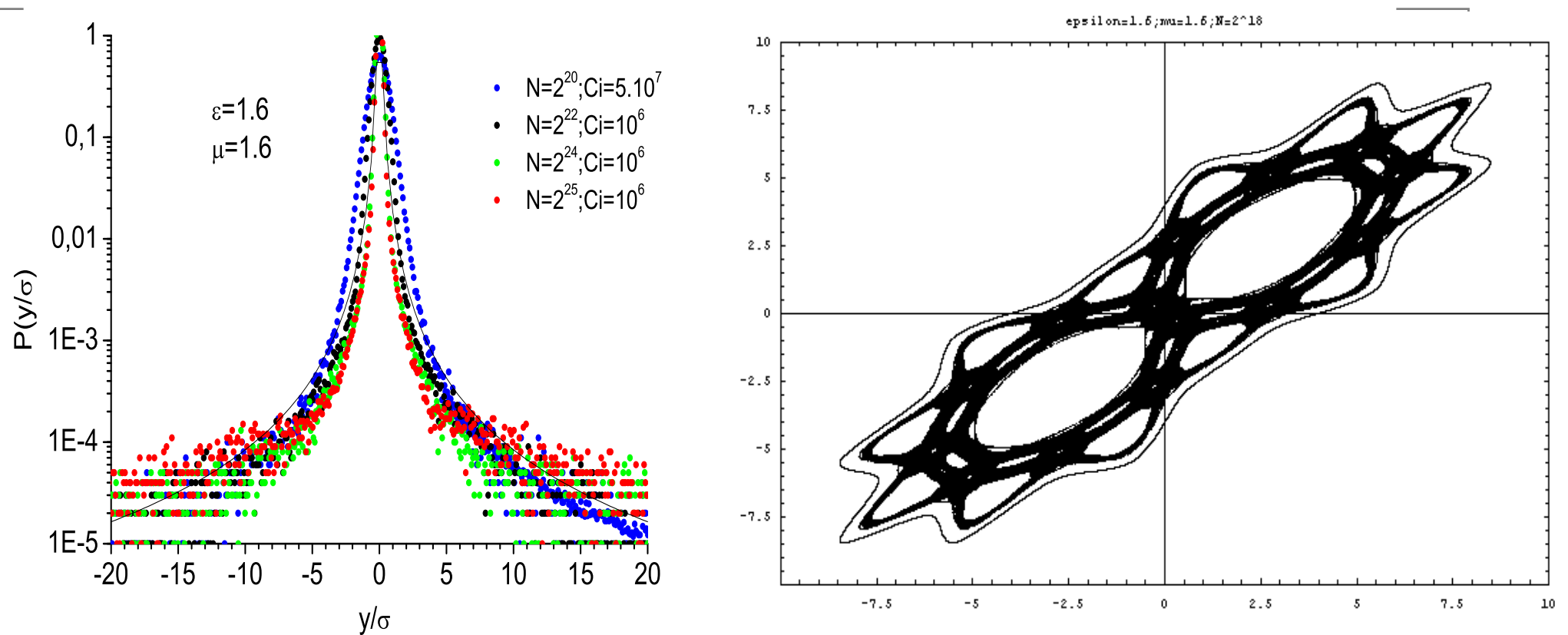
Figure 7. Similar dynamical and statistical behavior of chaotic orbits of the MacMillan map is observed for $\mu = 1.6$, $\epsilon = 1.6$, as in the $\epsilon = 1.2$ case. Orbital diffusion to an outer chain of islands generates pdfs of iterate sums that also converge to a true q–Gaussian as N increases to larger and larger values.

Quasi–stationary Chaotic States in Fermi–Pasta–Ulam Hamiltonians

The FPU $\beta-$ model is a one–dimensional lattice of nonlinear oscillators described by the Hamiltonian

$$H = \frac{1}{2}\sum_{j=1}^{N} p_j^2 + \sum_{j=0}^{N}\left(\frac{1}{2}(q_{j+1} - q_j)^2 + \frac{1}{4}\beta(q_{j+1} - q_j)^4\right) = E \qquad (23)$$

E being its total energy. We shall impose:

1) **fixed boundary conditions (fbc)**: $q_0(t) = q_{N+1}(t) = 0$, or

2) **periodic boundary conditions (pbc)**: $q_j(t) = q_{j+N}(t), \quad p_j(t) = p_{j+N}(t)$, for all $t > 0$.

We focus on **Simple Periodic Orbits (SPOs)**, where all variables return to their initial state after only one maximum and one minimum in their oscillation. Examples of such SPOs are **Nonlinear Normal Modes (NNMs)**, i.e. continuations of linear normal modes of the FPU chain described by the Q_q and P_q variables:

$$Q_q = \sqrt{\frac{2}{N+1}}\sum_{i=1}^{N} q_i \sin\frac{qi\pi}{N+1}, \qquad P_q = \dot{Q}_q \qquad (24)$$

These solutions are:

(a) The FPU π–Mode under pbc with N even

$$\hat{q}_j(t) = -\hat{q}_{j+1}(t) \equiv q(t), \ j = 1, \ldots, N \tag{25}$$

(b) The SPO1 mode under fbc, with N odd,

$$\hat{q}_{2j}(t) = 0, \ \hat{q}_{2j-1}(t) = -\hat{q}_{2j+1}(t) \equiv \hat{q}(t), \ j = 1, \ldots, \frac{N-1}{2}. \tag{26}$$

(c) The SPO2 mode under fbc, with $N = 5 + 3m, \ m = 0, 1, 2, \ldots$

$$\hat{q}_{3j}(t) = 0, \ j = 1, 2, 3 \ldots, \frac{N-2}{3}, \tag{27}$$

$$\hat{q}_j(t) = -\hat{q}_{j+1}(t) = \hat{q}(t), \ j = 1, 4, 7, \ldots, N-1. \tag{28}$$

which are exact continuations of the $q = N/2$, $q = (N+1)/2$ and $q = 2(N+1)/3$ linear modes respectively. Let us see what these solutions look like for some small particle chains.

FPU N=4 OPM with fixed boundary conditions
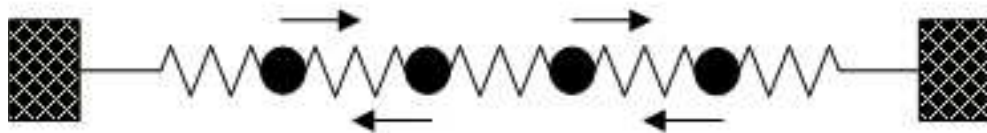
FPU N=7 SPO1 with fixed boundary conditions

FPU N=8 SPO2 with fixed boundary conditions
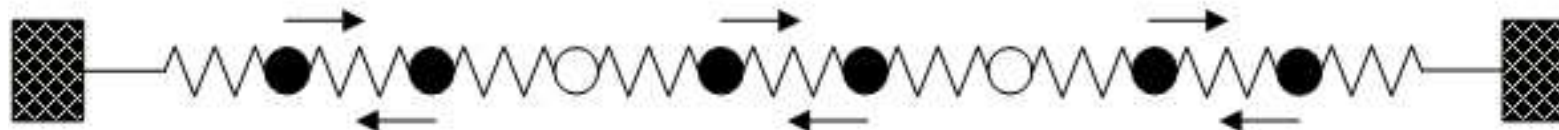
Figure 8: The π−mode of oppositely moving particles, the SPO1 mode with every other particle being stationary and the SPO2 mode, with one stationary particle every other two.

Let us study chaotic regions near these NNM orbits, **at energies where they have just turned unstable**.

(a) The FPU π–Mode for N=128 particles under pbc

Here, we choose as an observable the quantity

$$\eta(t) = q_{\frac{N}{2}}(t) + q_{\frac{N}{2}-1}(t) \tag{29}$$

using the fact that $\eta(t) = 0$ exactly at the π–mode. At energies above its first destabilization threshold, i.e. $E > E_u^1$, $\eta(t)$ deviates from zero and **starts to explore a thin chaotic layer**. We first consider the case of $N = 128$ and $\beta = 1$ and take as our total energy $E = 0.768$, at which the π–mode has just turned unstable.

As we see in Figures 9 and 10, **as we increase the total integration time** of our numerical trajectory, the statistical distributions (red curves) **approach closer and closer to a Gaussian with q tending to 1**.
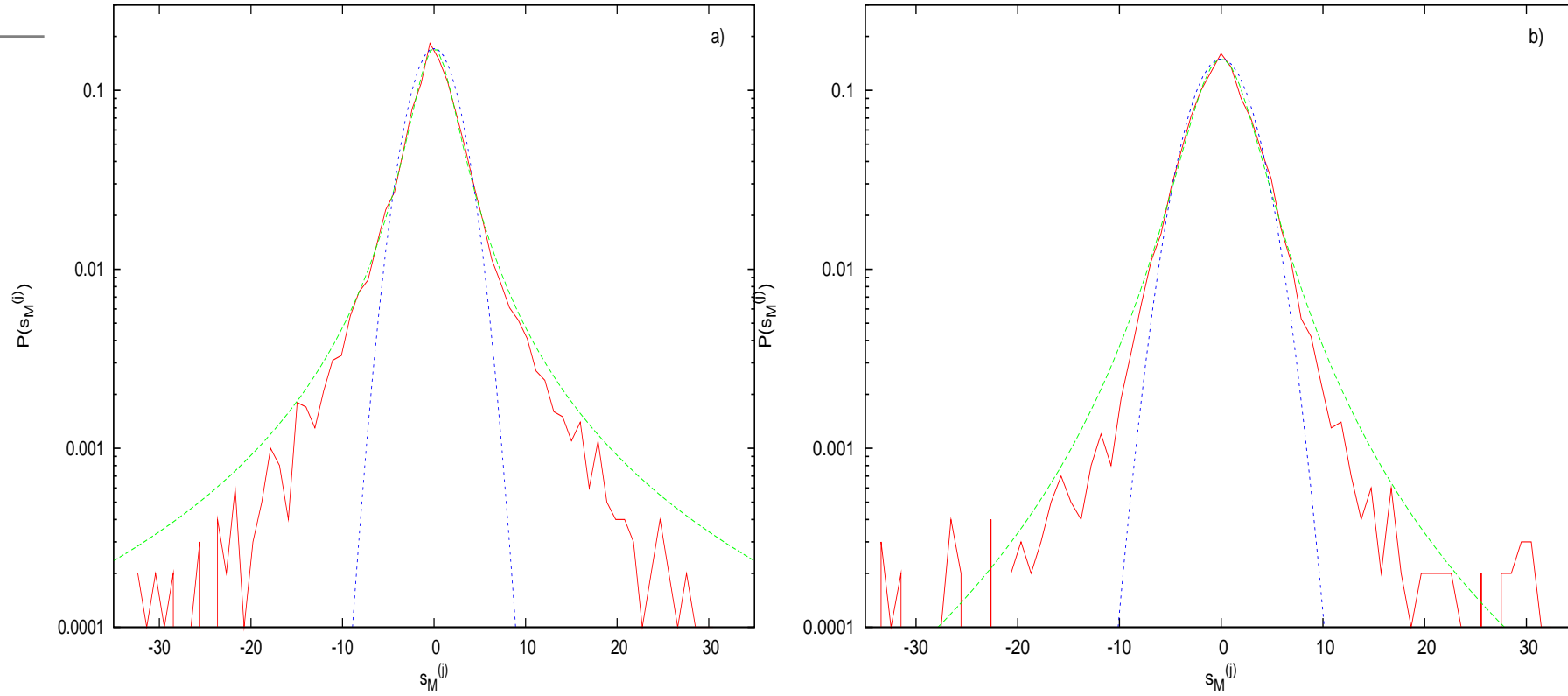
Figure 9: Plot in linear–log scale of numerical (red curve), q–Gaussian (green curve) and Gaussian (blue curve) distributions for the FPU $\pi-$ mode with p.b.c. for $N = 128$ degrees of freedom, $\beta = 1$ and $E = 0.768$. Panel a) corresponds to integration **time** $t_f = 10^5$. The numerical fitting with a q–**Gaussian gives** $q \approx 1.818$. Panel b) corresponds to $t_f = 10^6$ using $N_{\mathsf{ic}} = 100$ and $M = 100$ terms in the sums. Here the fitting is with a q–**Gaussian with** $q \approx 1.531$.
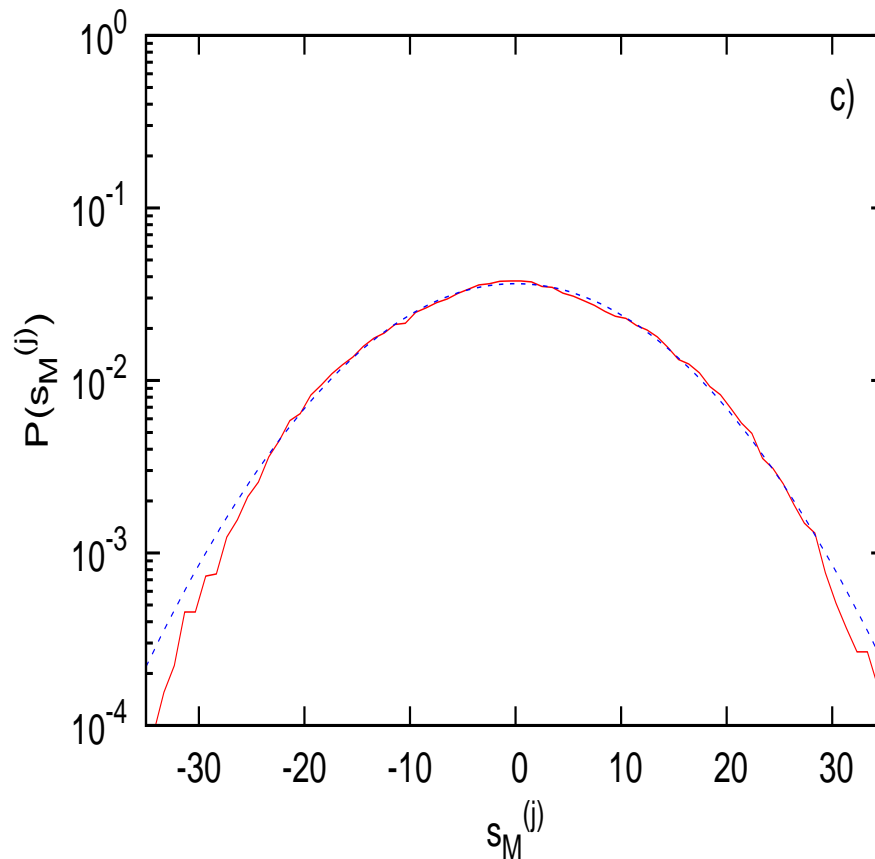
Figure 10: This plot corresponds to final integration time of $t_f = 10^8$ using time windows of length $N_{ic} = 1000$ and $M = 1000$ terms in the computations of the sums. Here the numerical distribution (red curve) has almost converged to a Gaussian (blue curve).

(b) FPU SPO1 mode for N=5 particles under fbc

We now examine the chaotic dynamics and study statistical distributions near the SPO1
nonlinear mode of an FPU–β chain with $N = 5$ particles, under **fixed boundary conditions**.

The chaotic regions near this solution **just above its first destabilization energy** are shown
in Figure 11. At first, **a "figure eight"** appears made by an orbit starting at a distance
$\approx 1 \times 10^{-7}$ from the SPO1 mode, see the surface of section (q_1, p_1) of Figure 11 (at times
when $q_3 = 0$ and $E = 7.4$).

Starting now at a distance of $\approx 1. \times 10^{-2}$ from the saddle point, a **more extended chaotic
region** is observed, **in the form of a green "figure eight cloud"** enveloping the first orbit.

Choosing even more distant initial conditions, e.g. one starting $\approx 3.4 \times 10^{-1}$ from the saddle
point, a **much larger chaotic region** is obtained, which spreads uniformly over a much
larger part of the available energy surface.
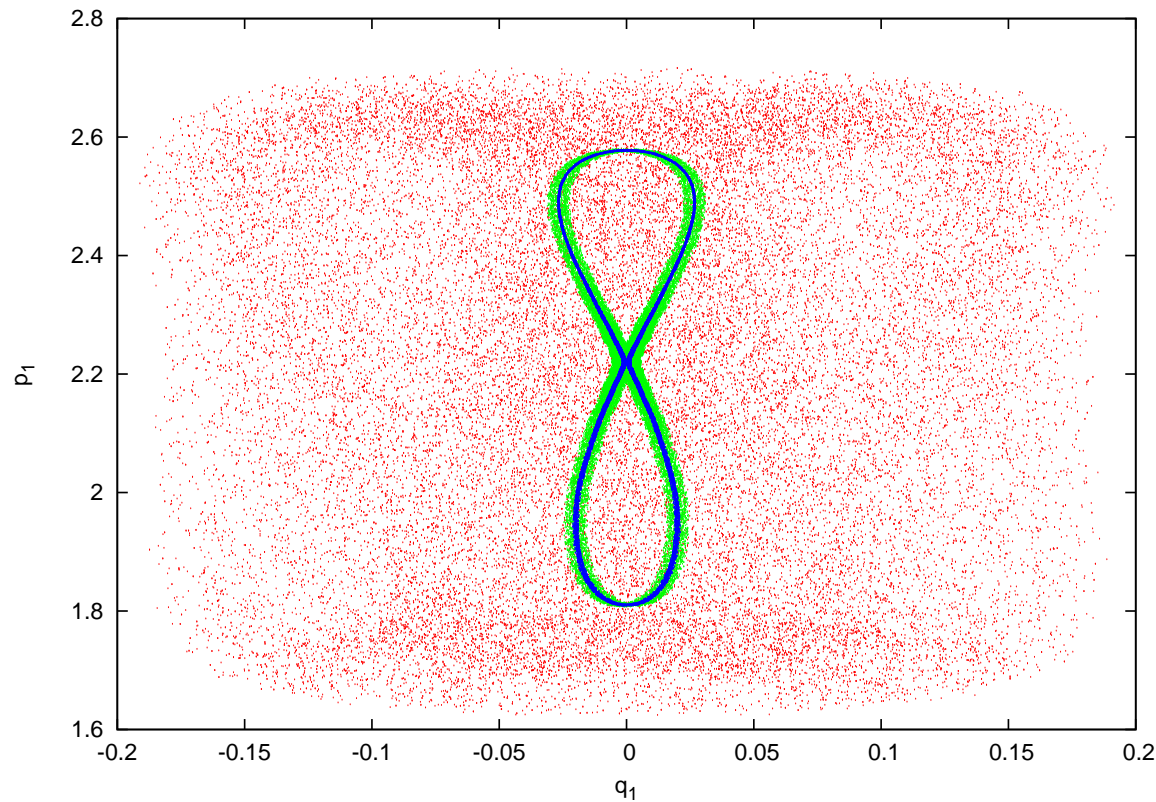
Figure 11: (i) **The "figure eight" chaotic region (blue points)** for an orbit starting at a distance $\approx 1.2 \times 10^{-7}$ from SPO1 mode at the saddle point in the figure), (ii) **a fatter "figure eight cloud" (green points)** is seen starting at ($\approx 1.086 \times 10^{-2}$) and **a much larger chaotic region (red points)** on the energy surface for an initial condition even more distant ($\approx 3.421 \times 10^{-1}$). $N = 5$ and $\beta = 1$, on the surface of section (q_1, p_1) computed at $q_3 = 0$. In this figure, we have integrated our three orbits up to $t_f = 10^5$ on the energy surface $E = 7.4$.

In the present example, we have chosen as an observable the quantity

$$\eta(t) = q_1(t) + q_3(t) \tag{30}$$

which is equal to zero at the SPO1 orbit and becomes nonzero due to numerical errors at energies just above the first destabilization energy E_u^1 of the mode.

Instead of studying 3 different initial conditions as we did in Figure 11, we proceed in Figures 12, 13 and 14 to plot on the left panel the surface of section of a trajectory starting at $\approx 1 \times 10^{-7}$ from the unstable SPO1) **for times** $t_f = 10^5$, $t_f = 10^7$ **and** $t_f = 10^8$ **respectively**, while on the right panels we plot the corresponding pfds of the normalized sums.

Clearly, as the integration time t_f grows, our chaotic orbit eventually wanders over a more extended domain, covering gradually a much larger part of the energy surface when $t_f = 10^8$. This may also be explained by the behavior of the Lyapunov exponents of the orbit (see Figure 15).
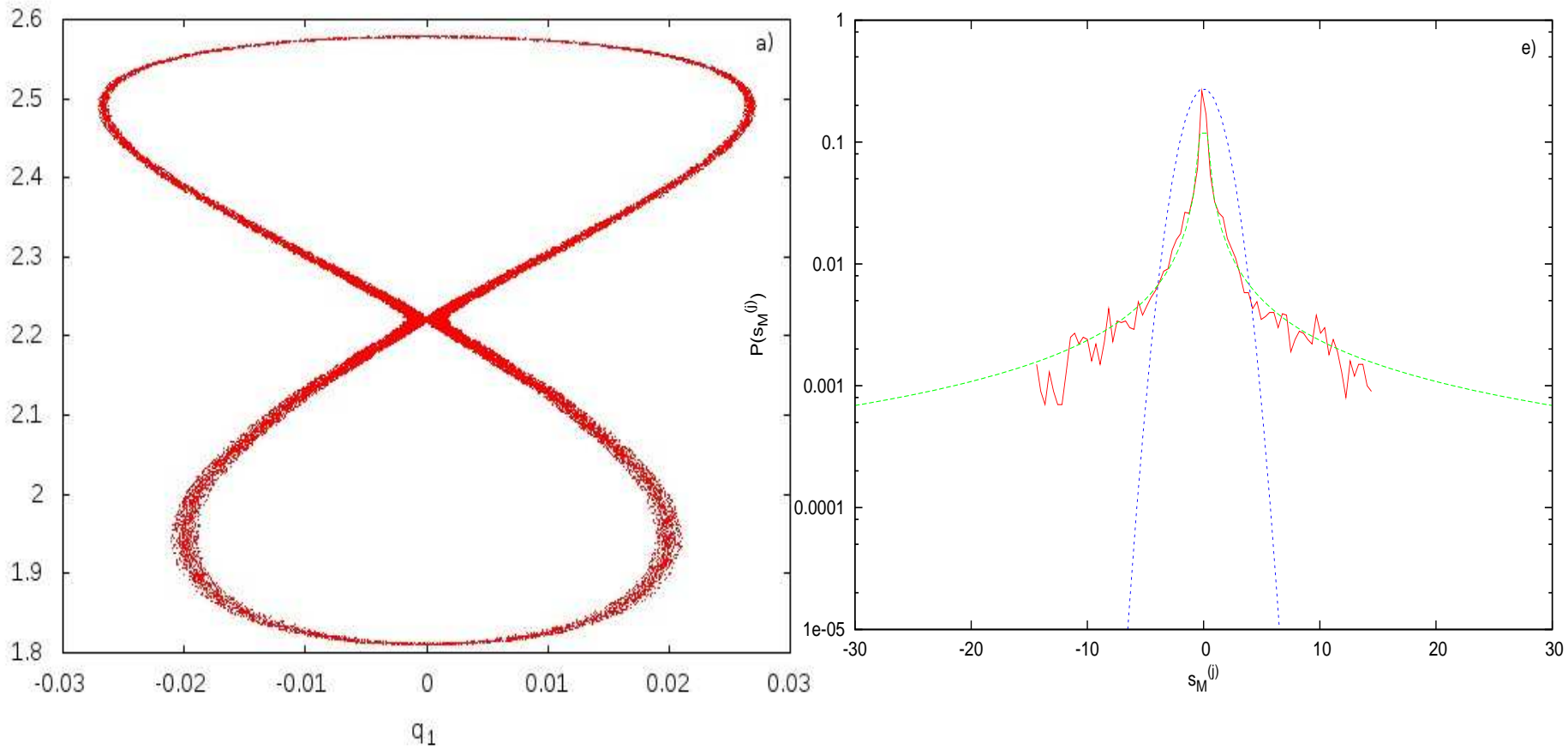
Figure 12. Left: Surface of section of a trajectory starting from a distance of $\approx 1.2 \times 10^{-7}$ from the unstable SPO1 saddle and integrated for **a total time** $t_f = 10^5$. **Right:** For the same integration time, we find that the pdf representing the **distribution of the sums** is well fitted by a q–**Gaussian,** $q \approx 2.785$ with $\chi^2 \approx 4.05 \times 10^{-6}$.
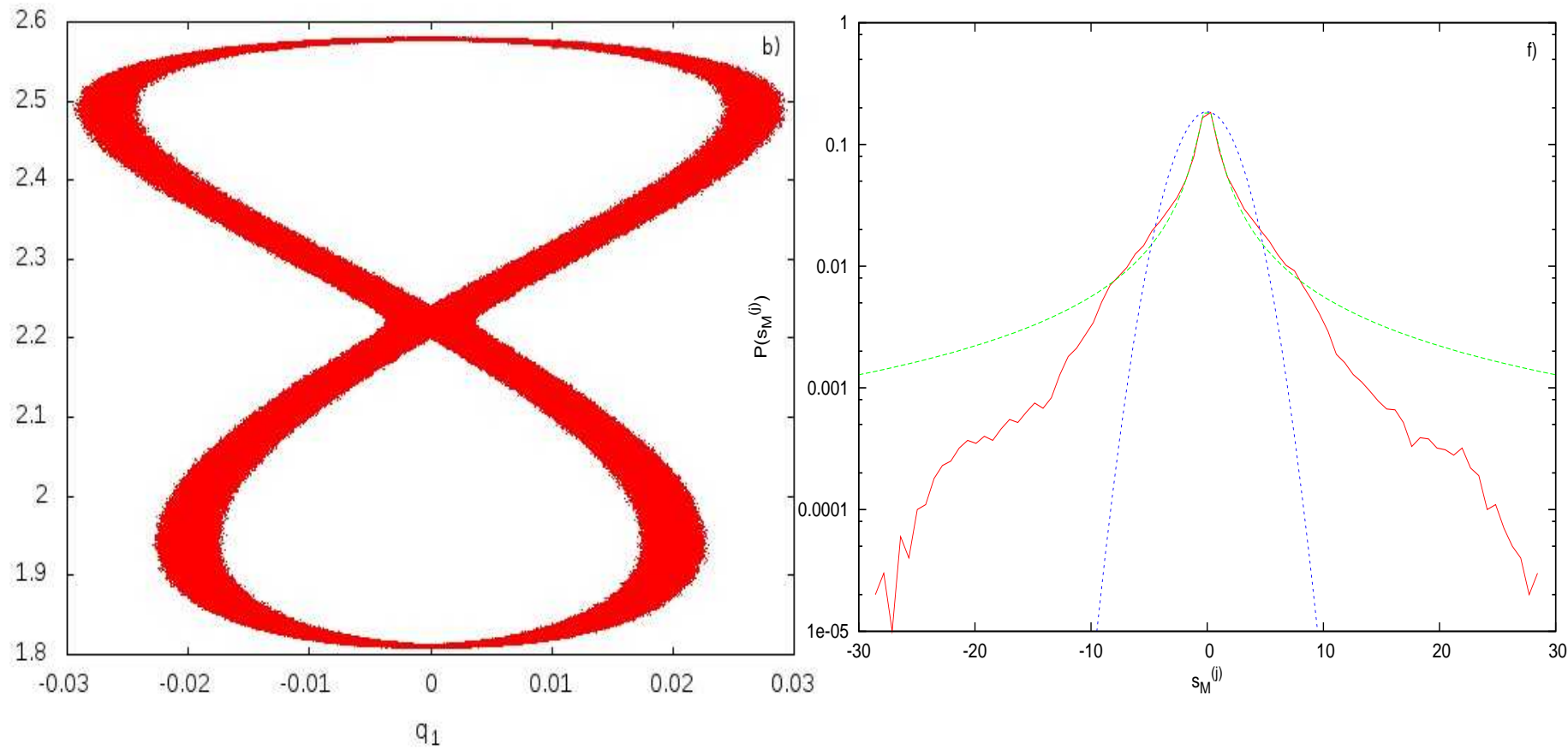
Figure 13: Left: Surface of section of a trajectory starting from a distance $\approx 1.192 \times 10^{-7}$ from the unstable SPO1 saddle point total after time $t_f = 10^7$. **Right:** For the same integration time, the **statistical distribution of the sums** of one chaotic component of the orbit can still be fitted–but not as well–by a q–**Gaussian with** $q \approx 2.483$ with $\chi^2 \approx 6.05 \times 10^{-6}$.
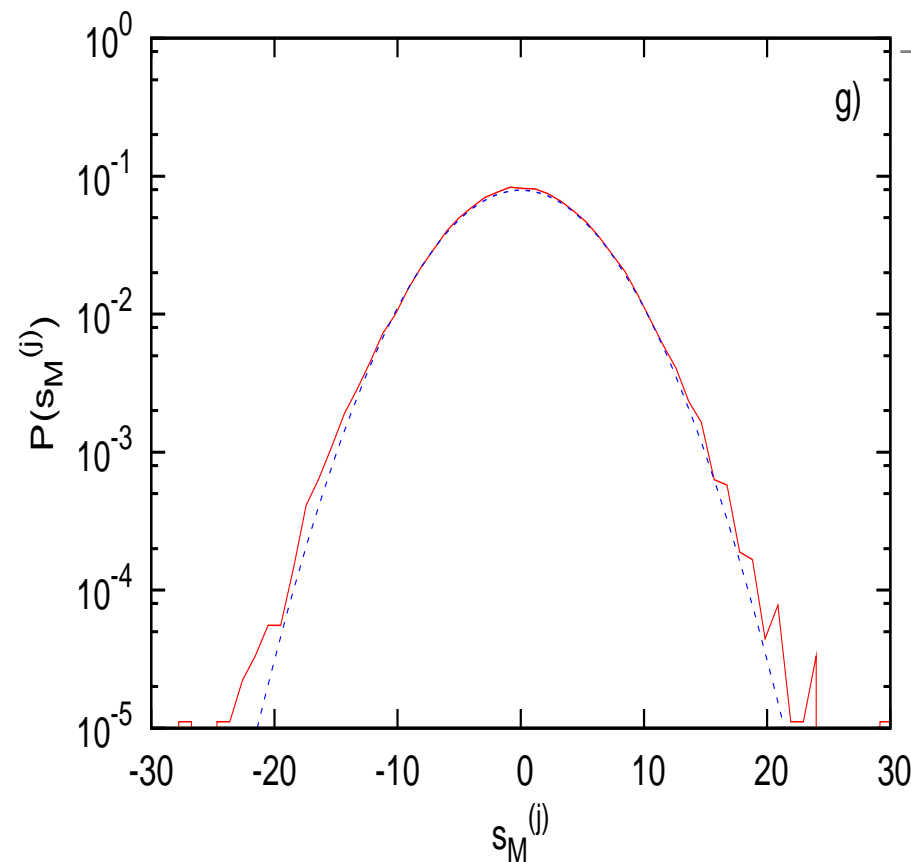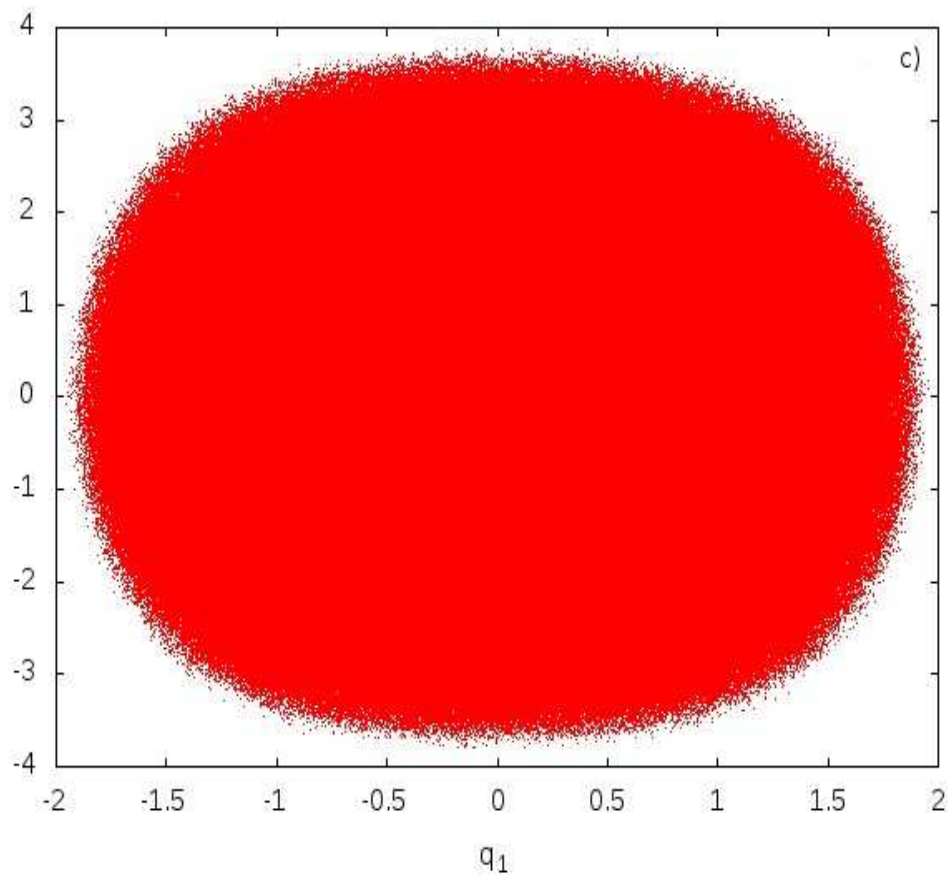
Figure 14: Left: Surface of section of the same trajectory for **total integration time** $t_f = 10^8$. **Right:** Final integration time $t_f = 10^8$ in the computations of the sums. In this case it is evident that **the distribution appears to converge to a Gaussian (q=1)**.
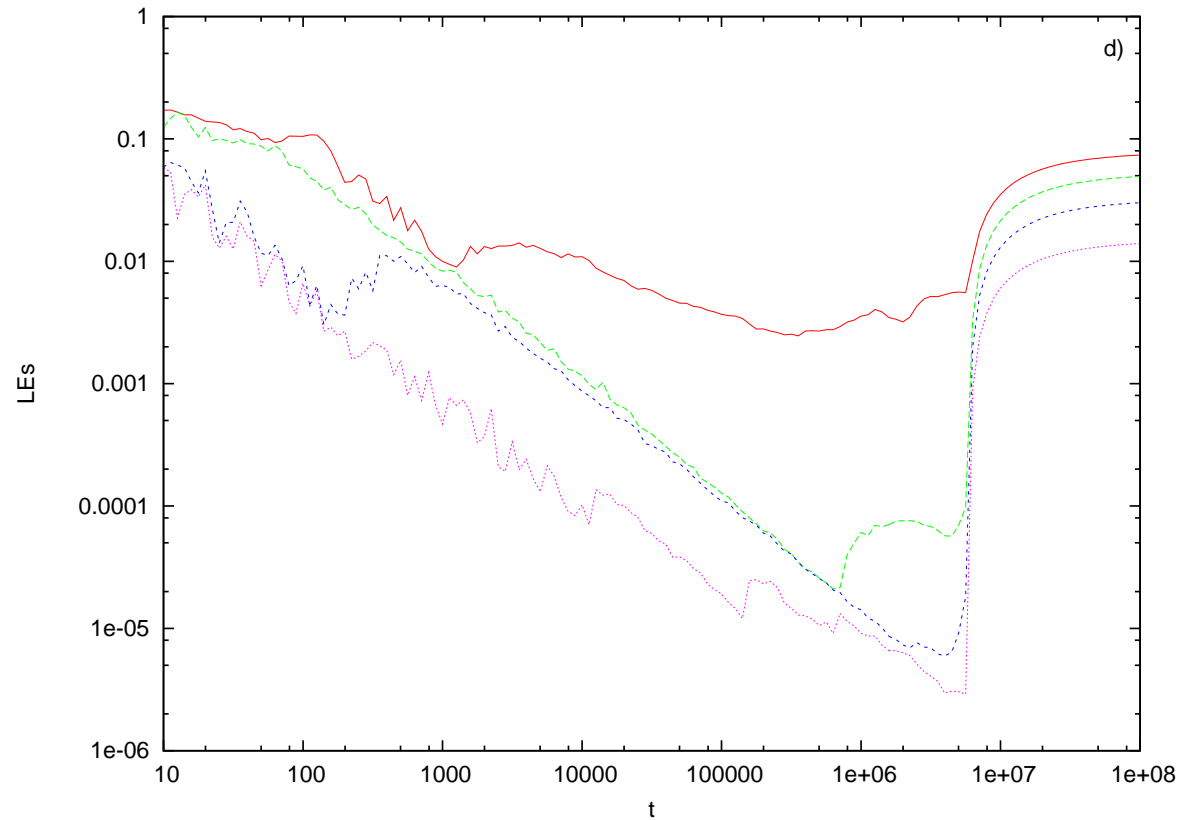
Figure 15: The 4 positive Lyapunov exponents of the previous solution integrated for a total time of $t = 10^8$. Observe the **sudden jump in their magnitude at ($t \simeq 10^7$)**, where the orbit **escapes from the region of "weak chaos" and q–Gaussian distributions** into the wider chaotic domain of **"strong chaos" where the statistics is Gaussian**.

(c) FPU SPO2 mode for N=5 particles under fbc

We also examined the neighborhood of the SPO2 mode, **which becomes unstable at much smaller energies**. Thus, we expect that, near SPO2, orbits will be more weakly chaotic and QSS will persist for longer times.

As Figure 16 shows, orbits now trace out a kind of **"banana" shaped region** (Fig. 16(a)) in a regime of **very small (positive) Lyapunov exponents** (Fig. 16(b)). Here, the normalized sum pdfs, up to $t_f = 10^{10}$!, **converge to a function that is close to a q–Gaussian** and never deviates towards a Gaussian. As we see in Figure 16(a), the dynamics near SPO2 **"sticks" to a type of quasiperiodic torus**, at least up to $t_f = 10^8$.

In Figure 16(b), we have plotted the four positive Lyapunov exponents up to $t_f = 10^9$. Note that, although they are all seen to decrease towards zero, at about $t_f > 10^9$, **the largest exponent shows a tendency to converge to a very small positive value of about 10^{-7}**, indicating that the orbit is "weakly chaotic".
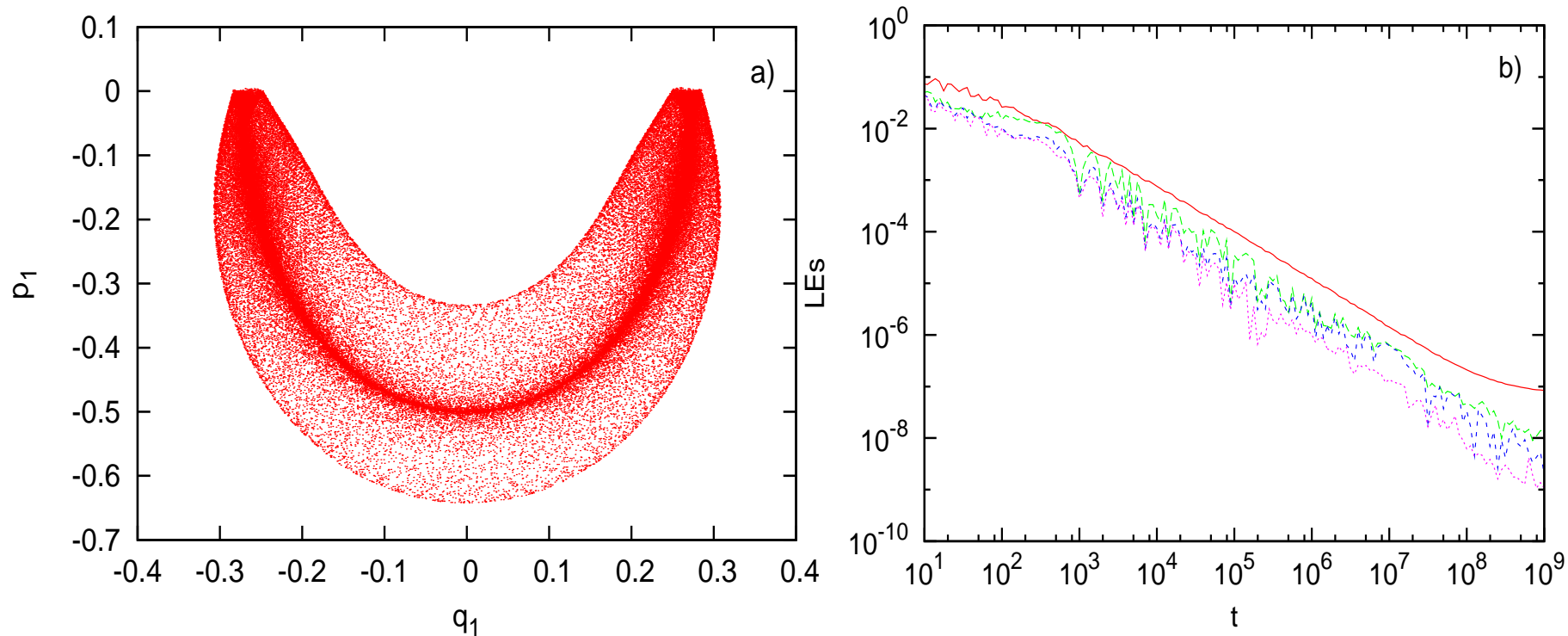
Figure 16: (a) The dynamics near SPO2 "sticks" to a quasiperiodic torus–like structure, at least up to $t_f = 10^8$. The weakly chaotic nature of the motion is shown in (b), where we have plotted the four positive Lyapunov exponents up to $t_f = 10^9$. Note that, although they all decrease towards zero, at about $t_f > 10^9$, **the largest exponent shows a tendency to converge to a very small positive value**.
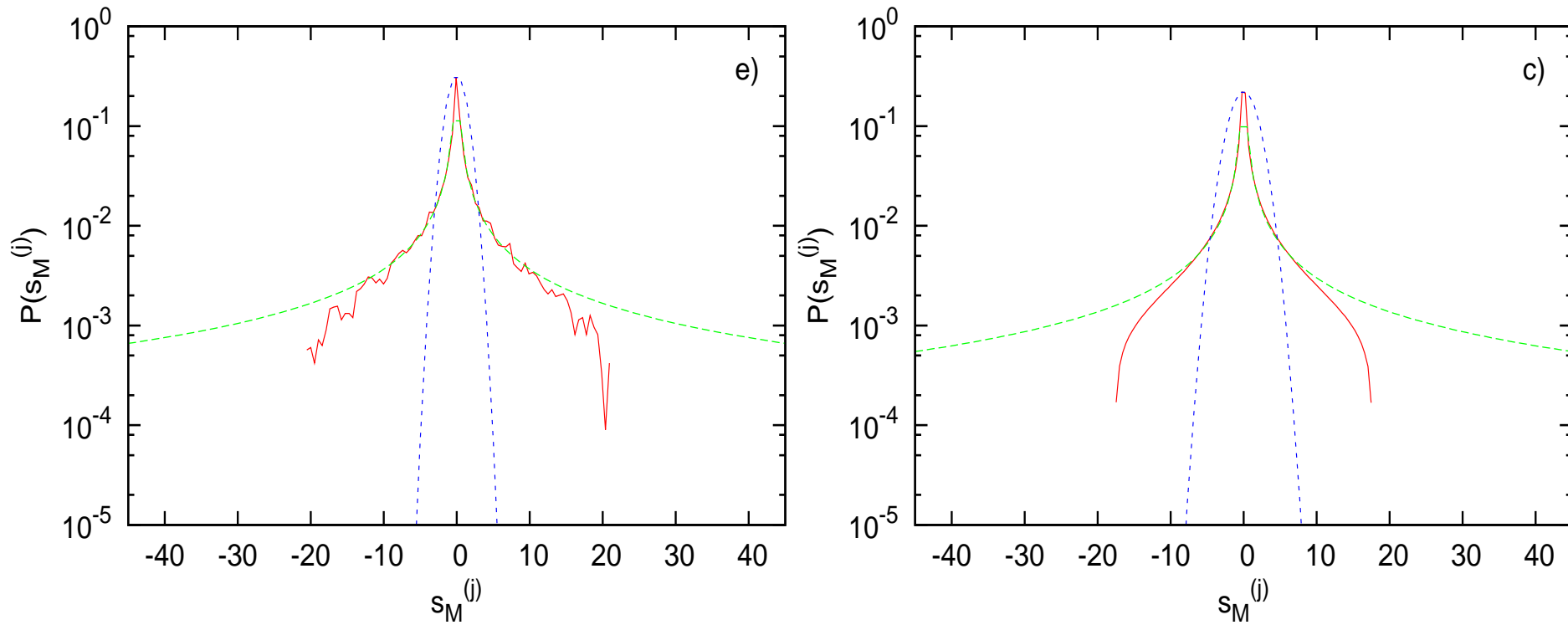
Figure 17: Left panel: The distribution of the normalized sum pdf of the orbit starting near SPO2, for a total integration time $t_f = 10^6$. Right panel: Remarkably at integration time $t_f = 10^{10}$ the pdf has converged to a shape whose central part resembles a q–Gaussian with $q \approx 2.769$, but turns down at the boundaries **having a temptingly smooth form that we have not yet been able to describe analytically**.
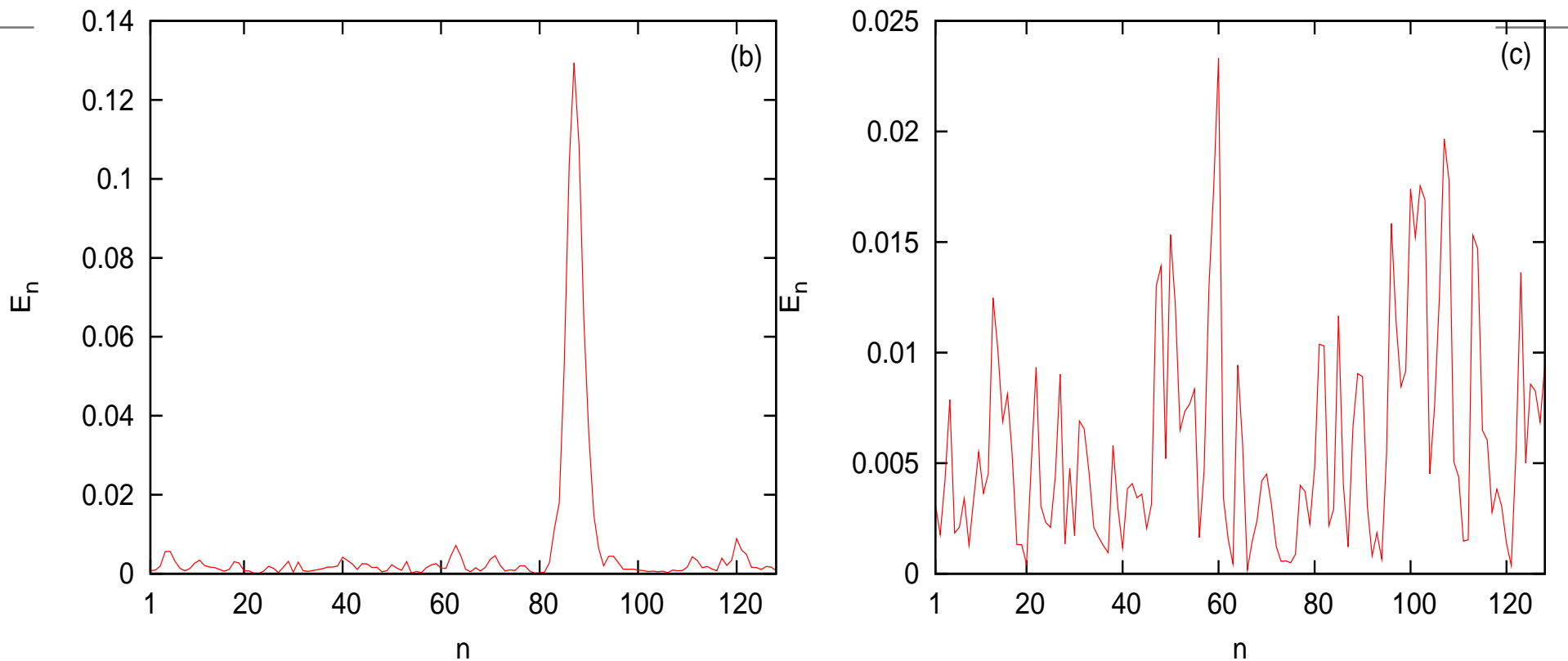
Figure 18: When does energy equipartition occur? Left: Plotting the instantaneous on site energy E_n along an $N = 128$ FPU chain with p.b.c., at $t = 10^7$ we observe a **chaotic breather preventing equipartition**. **Right:** At time $t = 10^8$, **the chaotic breather has collapsed and energy equipartition has set in**. [Cretegny et al., Physica D **121**, 109–126 (1998)].
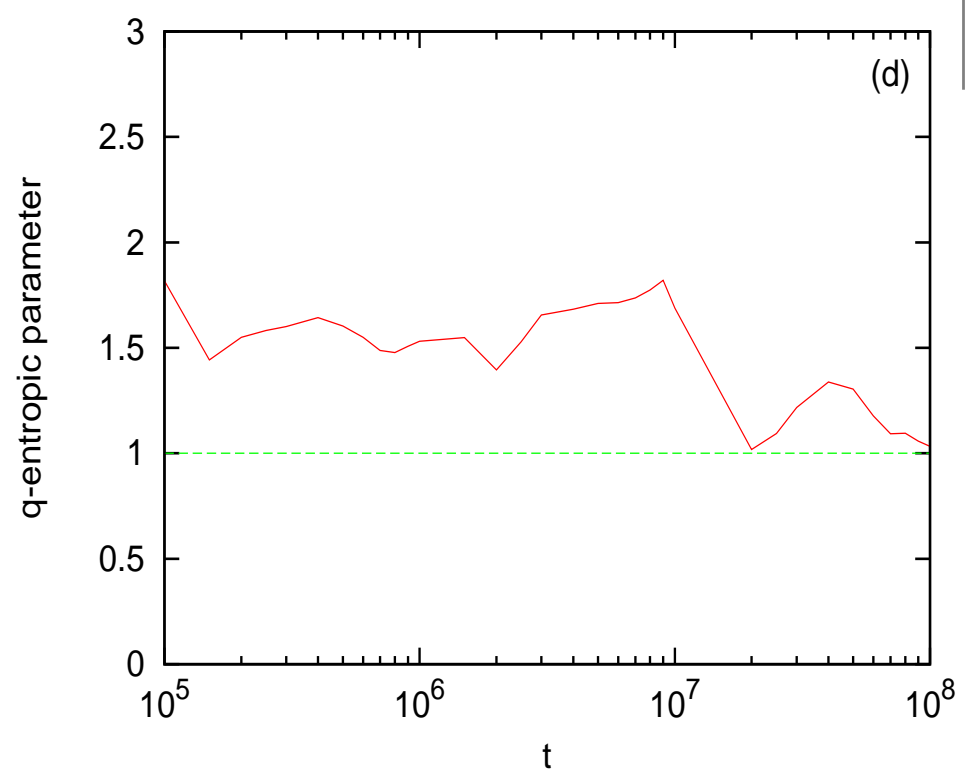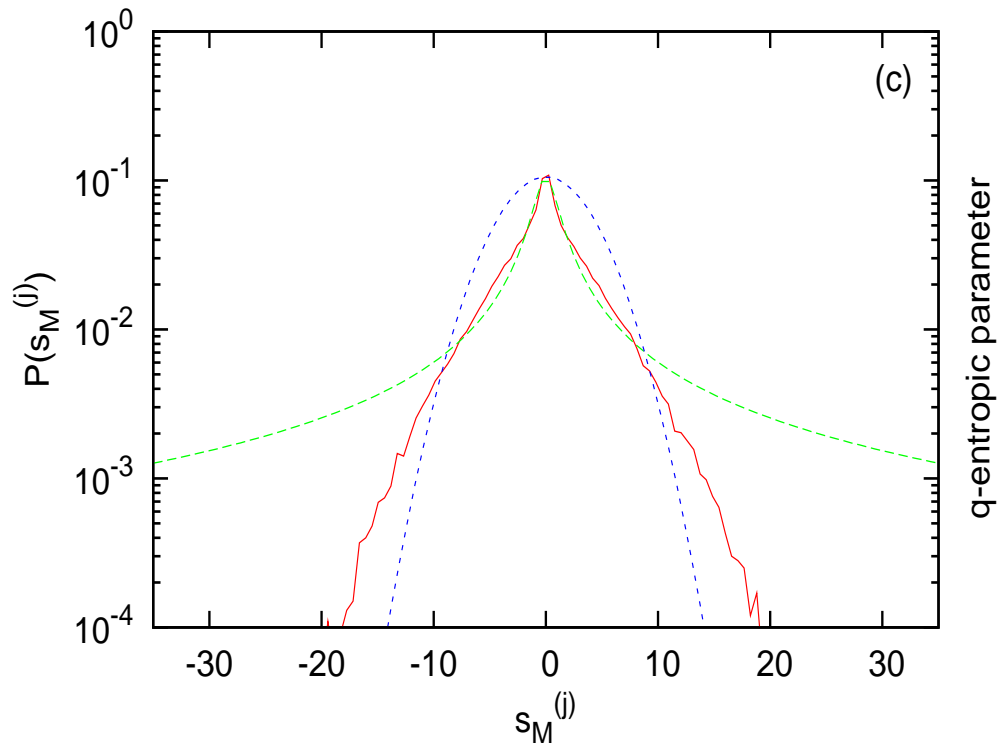
Figure 19: Left Panel: At $t = 10^7$, **the distribution describing the statistics of the chaotic breather is close to a** q-**Gaussian** with $q \approx 1.6$. **Right Panel: The approach to energy equipartition is indicated by the time evolution of the** q **index**, whose values on the average **fall significantly closer to 1 for** $t > 5 \times 10^7$.

Weakly and Strongly Chaotic Orbits in a Barred Galaxy Model

The motion of **a test particle in a 3D rotating model of a barred galaxy** is governed by the Hamiltonian:

$$H = \frac{1}{2}(p_x^2 + p_y^2 + p_z^2) + V(x, y, z) - \Omega_b(xp_y - yp_x). \tag{31}$$

The bar rotates around its z–axis (short axis), while the x–direction is along the major axis and the y along the intermediate axis of the bar. Ω_b **is the pattern speed of the bar and** H **is the total energy** of the orbit in the rotating frame of reference (Jacobi constant). The corresponding equations of motion are:

$$\dot{x} = p_x + \Omega_b y, \qquad\qquad \dot{y} = p_y - \Omega_b x, \qquad\qquad \dot{z} = p_z, \tag{32}$$

$$\dot{p_x} = -\frac{\partial V}{\partial x} + \Omega_b p_y, \qquad\qquad \dot{p_y} = -\frac{\partial V}{\partial y} - \Omega_b p_x, \qquad\qquad \dot{p_z} = -\frac{\partial V}{\partial z}.$$

The potential V of our model consists of three components: (1) A Miyamoto-Nagai disc:

$$V_D = -\frac{GM_D}{\sqrt{x^2 + y^2 + (A + \sqrt{z^2 + B^2})^2}}. \tag{33}$$

(2) A bulge, modeled by a Plummer sphere whose potential is:

$$V_S = -\frac{GM_S}{\sqrt{x^2 + y^2 + z^2 + \epsilon_s^2}}, \qquad (34)$$

where ϵ_s is the scale-length of the bulge and M_S is its total mass.

(3) A triaxial Ferrers bar, with density $\rho(x)$:

$$\rho(x) = \begin{cases} \rho_c(1 - m^2)^2 & , m < 1 \\ 0 & , m \geq 1 \end{cases}, \qquad (35)$$

where $\rho_c = \frac{105}{32\pi} \frac{GM_B}{abc}$ is the central density, M_B the total mass of the bar and

$$m^2 = \frac{x^2}{a^2} + \frac{y^2}{b^2} + \frac{z^2}{c^2}, \qquad a > b > c > 0, \qquad (36)$$

a, b and c being the semi-axes. The corresponding potential is:

$$V_B = -\pi G abc \frac{\rho_c}{n+1} \int_\lambda^\infty \frac{du}{\Delta(u)} (1 - m^2(u))^{n+1}, \qquad (37)$$

where $m^2(u) = \frac{x^2}{a^2+u} + \frac{y^2}{b^2+u} + \frac{z^2}{c^2+u}$, $\Delta^2(u) = (a^2+u)(b^2+u)(c^2+u)$, n is a positive integer (with $n = 2$ for our model) and λ is the unique positive solution of $m^2(\lambda) = 1$, outside of the bar ($m \geq 1$), and $\lambda = 0$ inside the bar. We use the parameter values G=1, Ω_b=0.054 (54 $km \cdot sec^{-1} \cdot kpc^{-1}$), a=6, b=1.5, c=0.6, A=3, B=1, ϵ_s=0.4, M_B=0.1, M_S=0.08, M_D=0.82. The units are: 1 kpc (length), 1000 $km \cdot sec^{-1}$ (velocity), 1 Myr (time), $2 \times 10^{11} M_\odot$ (mass). The total mass $G(M_S + M_D + M_B)$ is set equal to 1.

Realistically, the maximal time of integration of the orbits is T=10000Myr (10 billion yrs), corresponding to a time of the order of one Hubble time. **The question therefore is: Can we use pdfs to identify the " weakly" vs. "strongly" chaotic nature of the orbits based only on the small set of data provided by the integration over only $T = 10000$?**.

We test first **the 2-degree-of-freedom case:**
1) Strongly Chaotic Orbit 1: $H = E = -0.3$, $(x, y, p_x, p_y) = (0, -0.625, -0.314512, -0.24)$
2) Weakly Chaotic Orbit 2: $H = E = -0.36$, $(x, y, p_x, p_y) = (0, -0.625, -0.002, -0.24)$

**and then apply our methods to a more realistic 3-degree-of-freedom example**
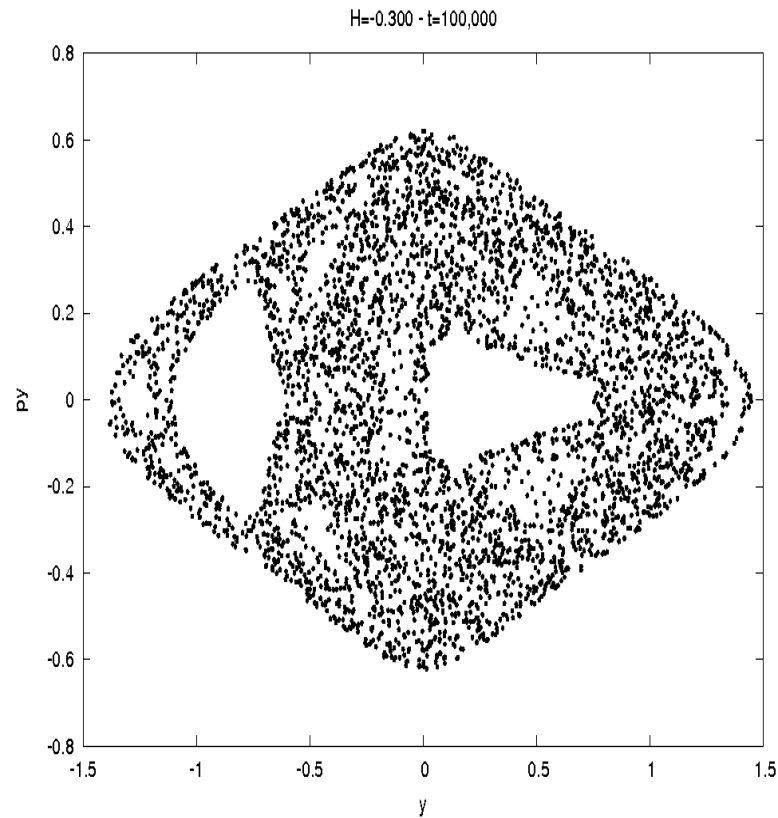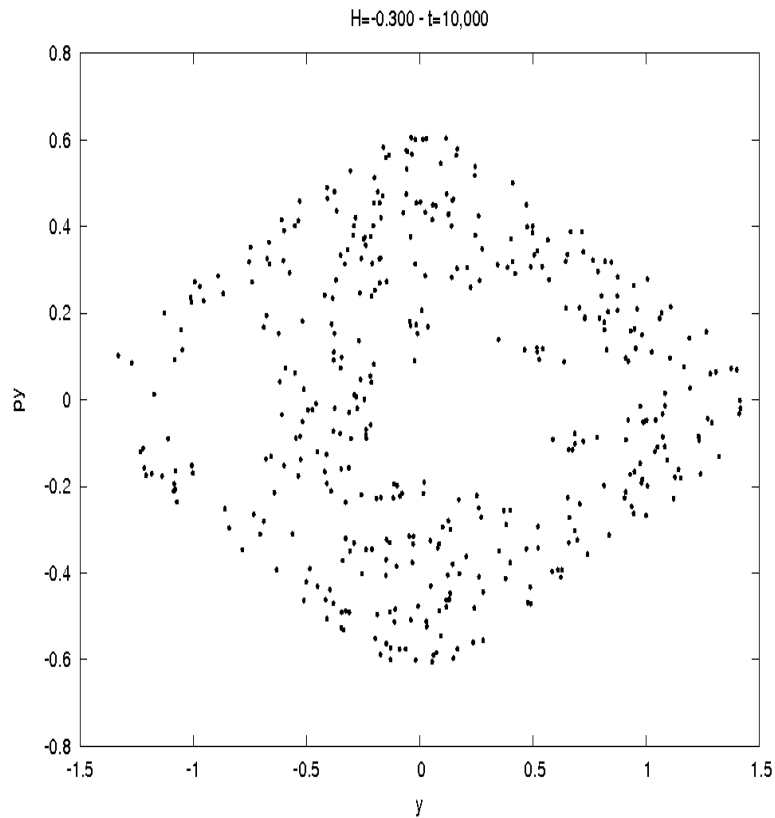
Figure 20: The Poincar$\acute{e}$ Surface of Section (PSS) (y, p_y) with $p_x > 0$, $x = 0$ for **the Chaotic Orbit 1** above of the 2DOF Hamiltonian system for final integration time $t_f = 10000$ (left panel) and $t_f = 100000$ (right panel) for the same data.
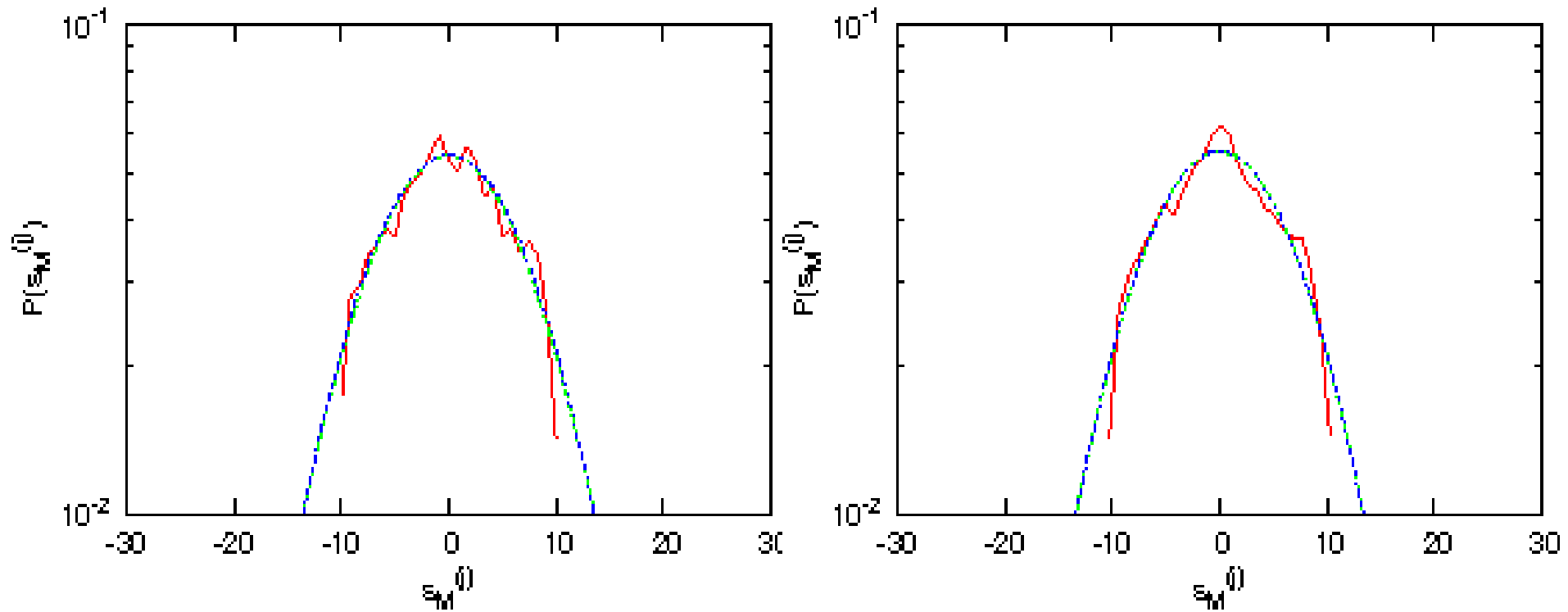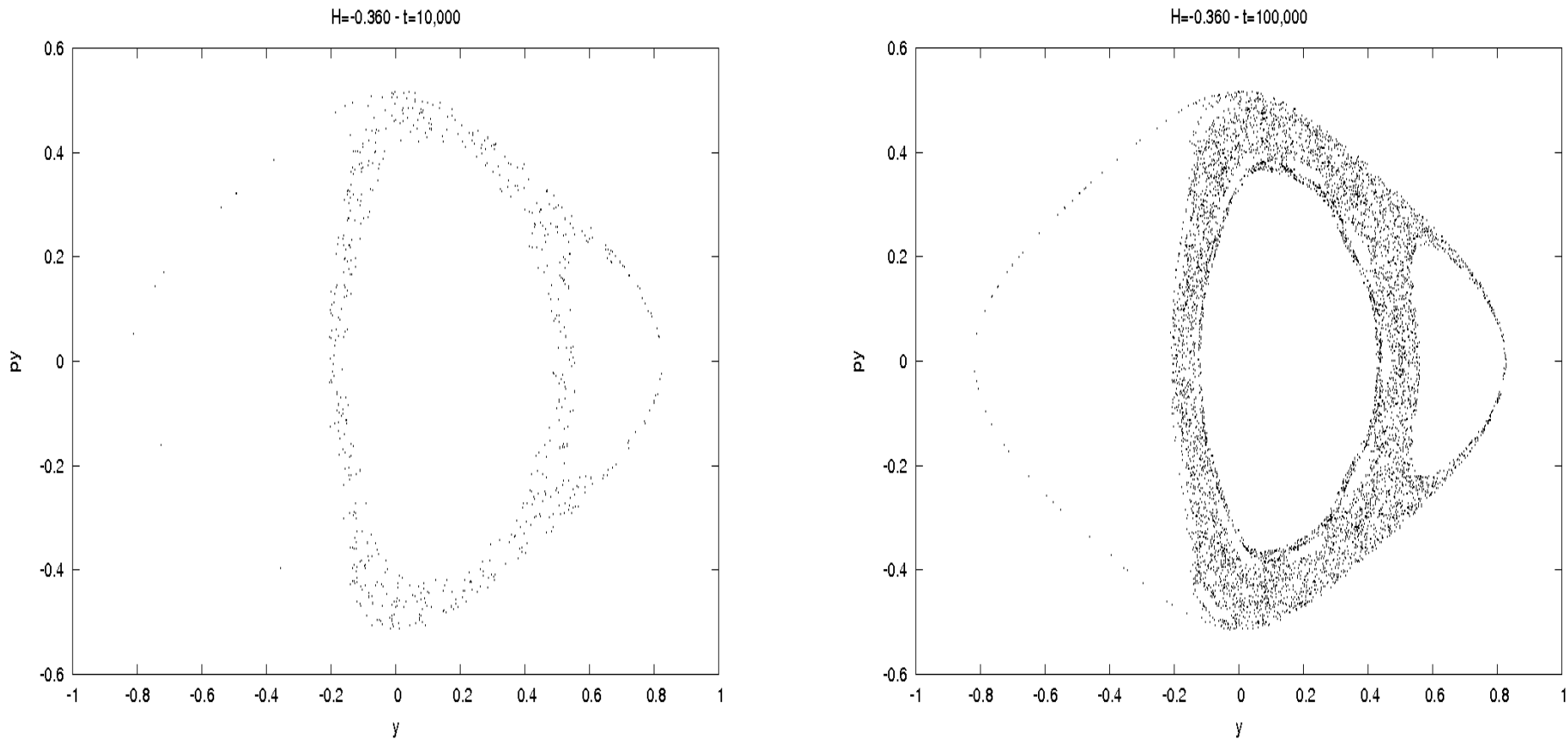
Figure 21: Pdfs of $\eta = x + y$ for the **the Chaotic Orbit 1** above: Plot in linear-log scale of numerical (red curve), q-Gaussian (green curve) and Gaussian (blue curve) distributions.
Left panel: Final integration time $t_f = 10000$, with $N_{ic} = 4000$ time windows and $M = 50$ terms in the sums. Numerical fitting with a q-Gaussian gives $q \approx 1.095$ with $\chi^2 \approx 0.0003$.
**Right panel:** $t_f = 100000$, $N_{ic} = 20000$ and $M = 10$, with $q \approx 0.97$ and $\chi^2 \approx 0.00033$.
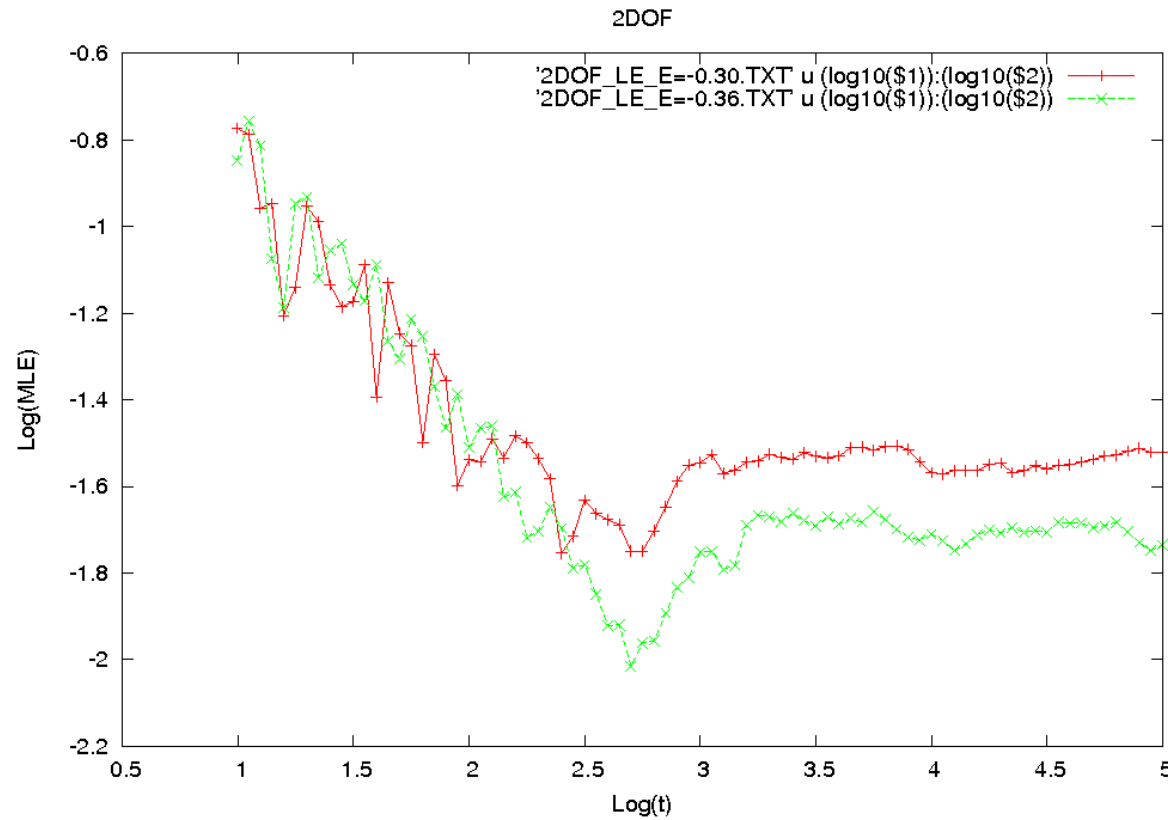
Figure 22: Maximum Lyapunov exponent evolution up to $t_f = 100000$ for the **the Chaotic Orbit 1** of the 2DOF Hamiltonian system (red curve) and for the Weakly Chaotic Orbit 2 of the same system (green curve).

Figure 23: Left panel: The Poincaré Surface of Section (PSS) (y, p_y) with $p_x > 0$, $x = 0$ for the **the Weakly Chaotic Orbit 2** of the 2DOF Hamiltonian system for integration time $t_f = 10000$ **(left panel) and** $t_f = 100000$ **(right panel)** for the same data.
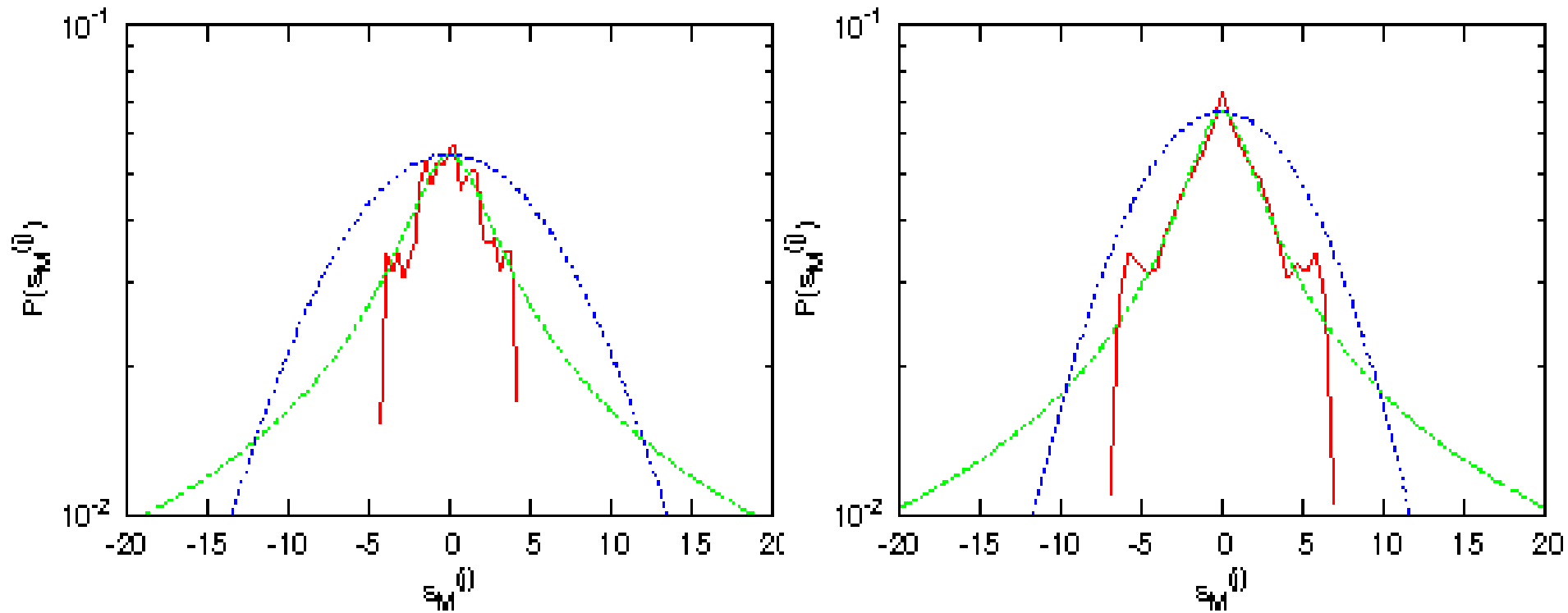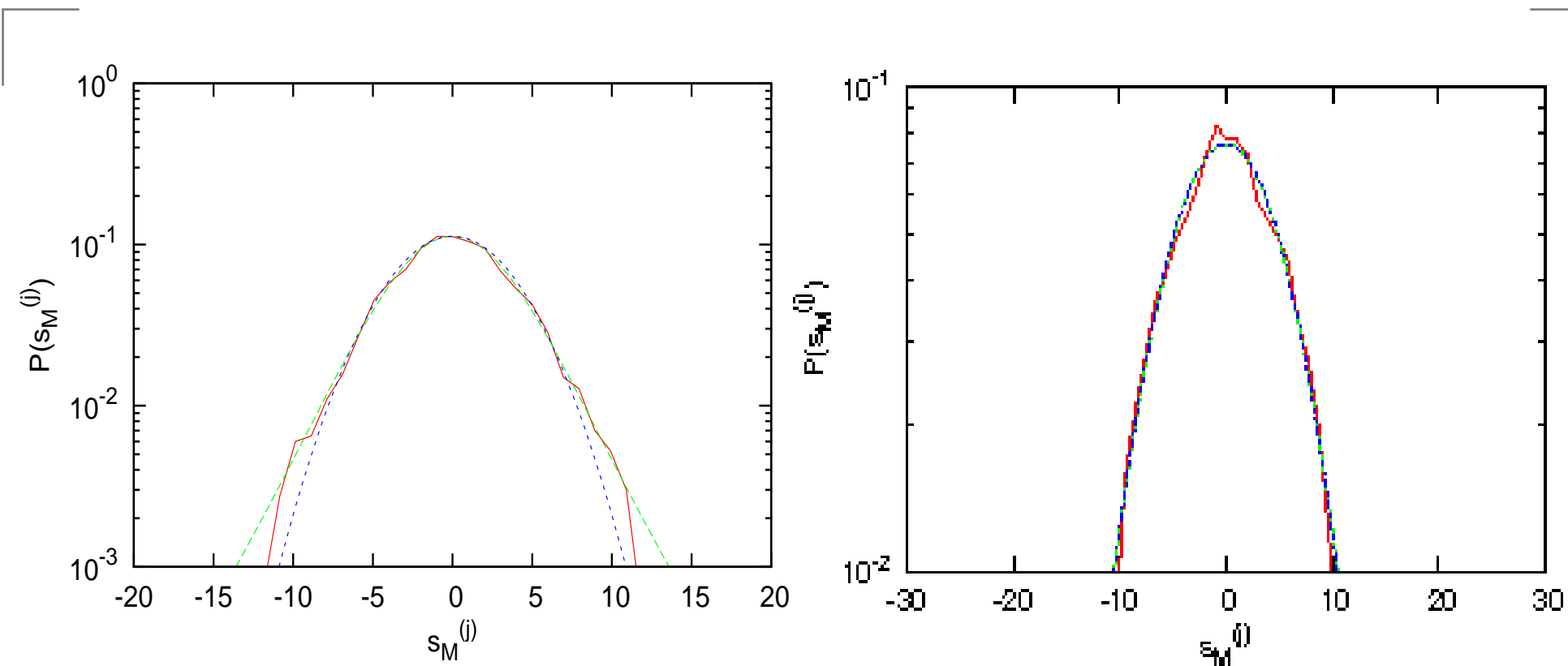
Figure 24: Pdfs of $\eta = x + y$ for the **the Weakly Chaotic Orbit 2**: Plot in linear-log scale of numerical (red curve), q-Gaussian (green curve) and Gaussian (blue curve) distributions.**Left panel: Final integration time** $t_f = 10000$, $N_{\mathsf{ic}} = 4000$ and $M = 50$ terms. Fitting with a q-Gaussian gives $q \approx 3.52$ with $\chi^2 \approx 0.00074$. **Right panel:** $t_f = 100000$, $N_{\mathsf{ic}} = 25000$ and $M = 50$. Here, the numerical fitting gives $q \approx 3.539$ with $\chi^2 \approx 0.00057$.
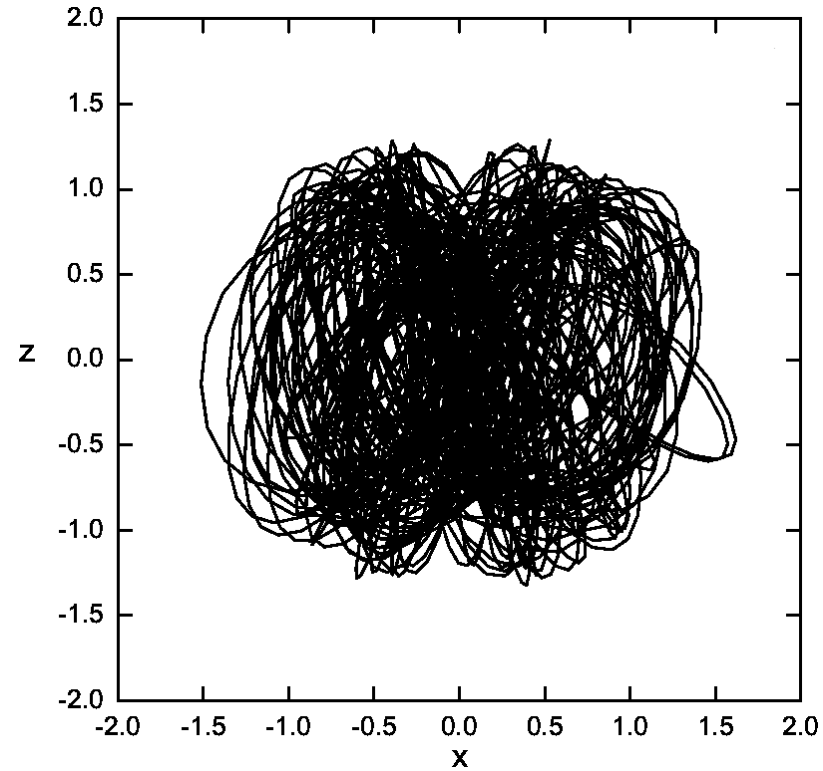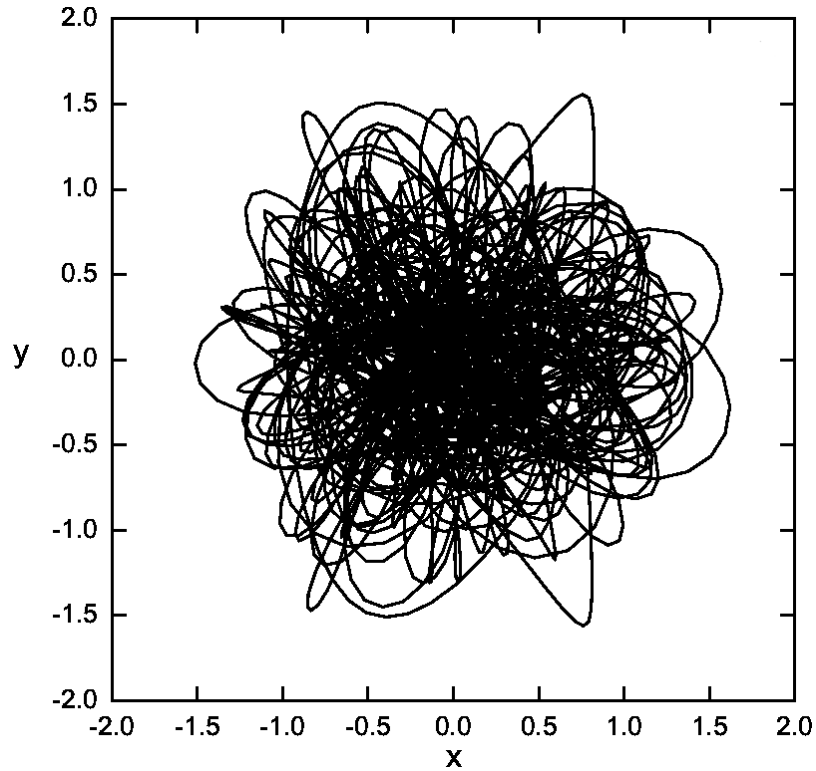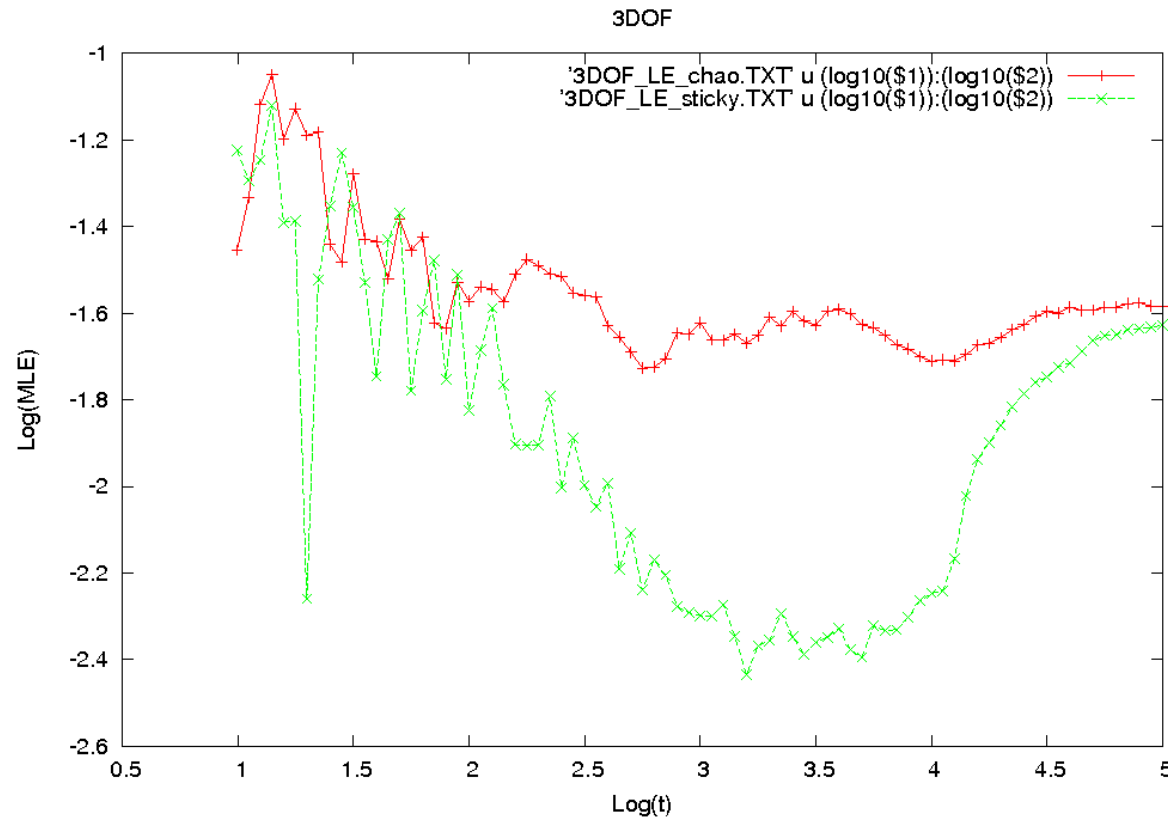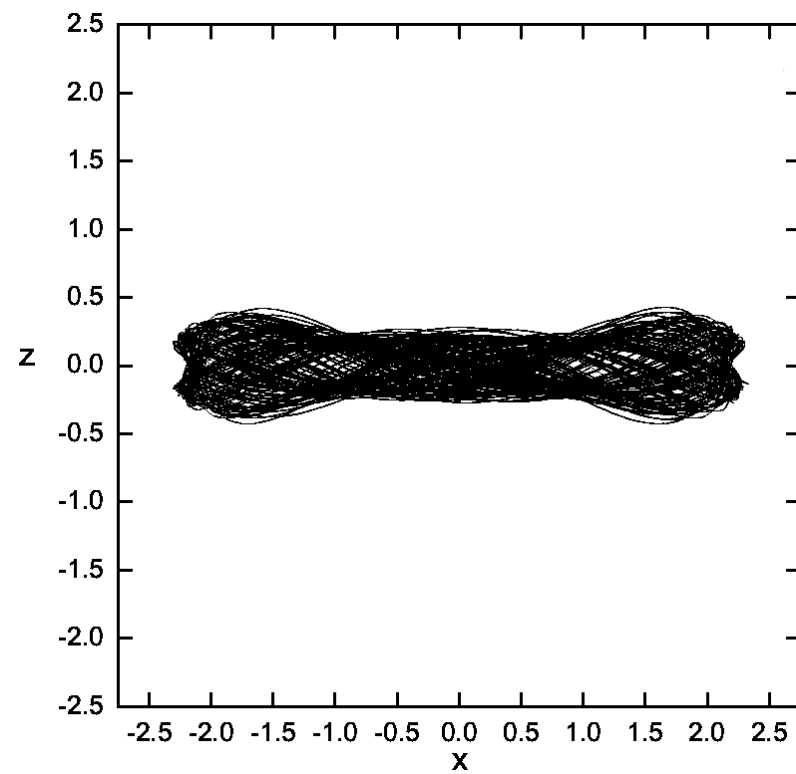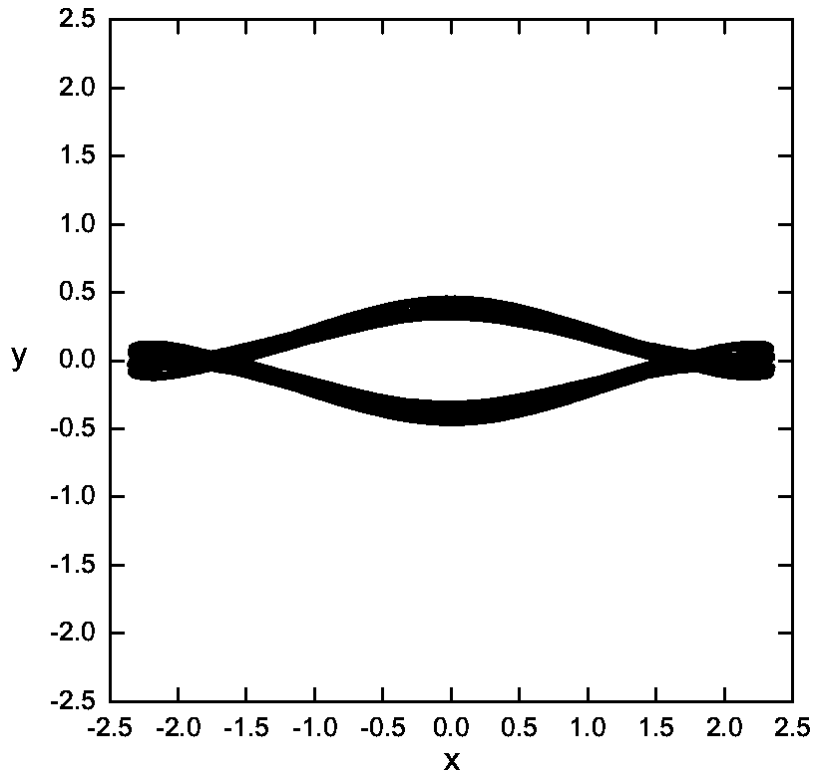
Figure 25: Left panel: Projections for the Chaotic Orbit 1 of the **3DOF Hamiltonian system** for **final integration time** $t_f = 10000$ in x, y and x, z **(right panel)**. Initial conditions: $(x, y, z, p_x, p_y, p_z) = (0.5875, 0, 1.291670, 0, 0, 0)$. $H = E = -0.2852654501087481$.

Figure 26: Pdf plots for the **Chaotic Orbit 1** of the 3DOF Hamiltonian system in linear-log scale of numerical (red curve), q-Gaussian (green curve) and Gaussian (blue curve) distributions. **Left panel:** $\eta = z$ **and** $t_f = 10000$ using $N_{\text{ic}} = 4000$ and $M = 50$ terms. Here, the numerical fitting gives $q \approx 1.25$ with $\chi^2 \approx 0.00017$. **Right panel:** $\eta = x + y$, $t_f = 100000$, $N_{\text{ic}} = 10000$ and $M = 100$ and fitting gives $q \approx 0.95$ with $\chi^2 \approx 0.00029$.

Figure 27: Maximum Lyapunov exponent evolution up to $t_f = 100000$ for the **Weakly Chaotic Orbit 2** of the **3DOF Hamiltonian system** (green curve) and **the Chaotic Orbit 1** of the same system (red curve).
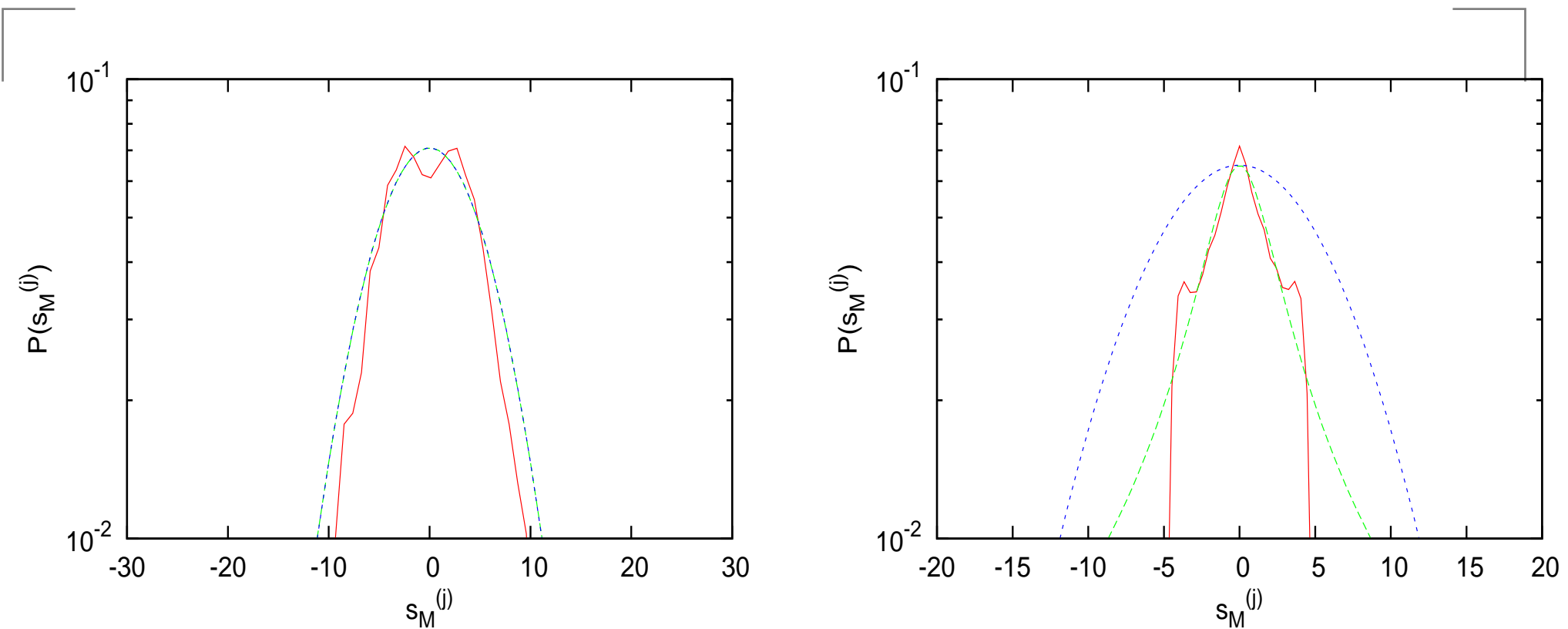
**Figure 28: Projections for the Weakly Chaotic Orbit 2** of the **3DOF Hamiltonian system** for **final integration time** $t_f = 10000$ in x, y (left panel) and x, z (right panel). Initial conditions: $H = E = -0.2792149022676664$, $(x, y, z, p_x, p_y, p_z) = (2.35, 0, 0.08883, 0, 0.133330, 0)$.

Figure 29: Pdf plots for the **Weakly Chaotic Orbit 2** of the **3DOF Hamiltonian system** in linear-log scale of numerical (red curve), q-Gaussian (green curve) and Gaussian (blue curve) distributions. **Left panel:** $\eta = z$ **and** $t_f = 10000$, with $N_{\text{ic}} = 4000$, $M = 50$ terms. **Right panel:** $\eta = x + y$, $t_f = 100000$, $N_{\text{ic}} = 10000$ and $M = 100$. In this case the numerical fitting with a q-Gaussian gives $q \approx 2.464$ with $\chi^2 \approx 0.00101$.
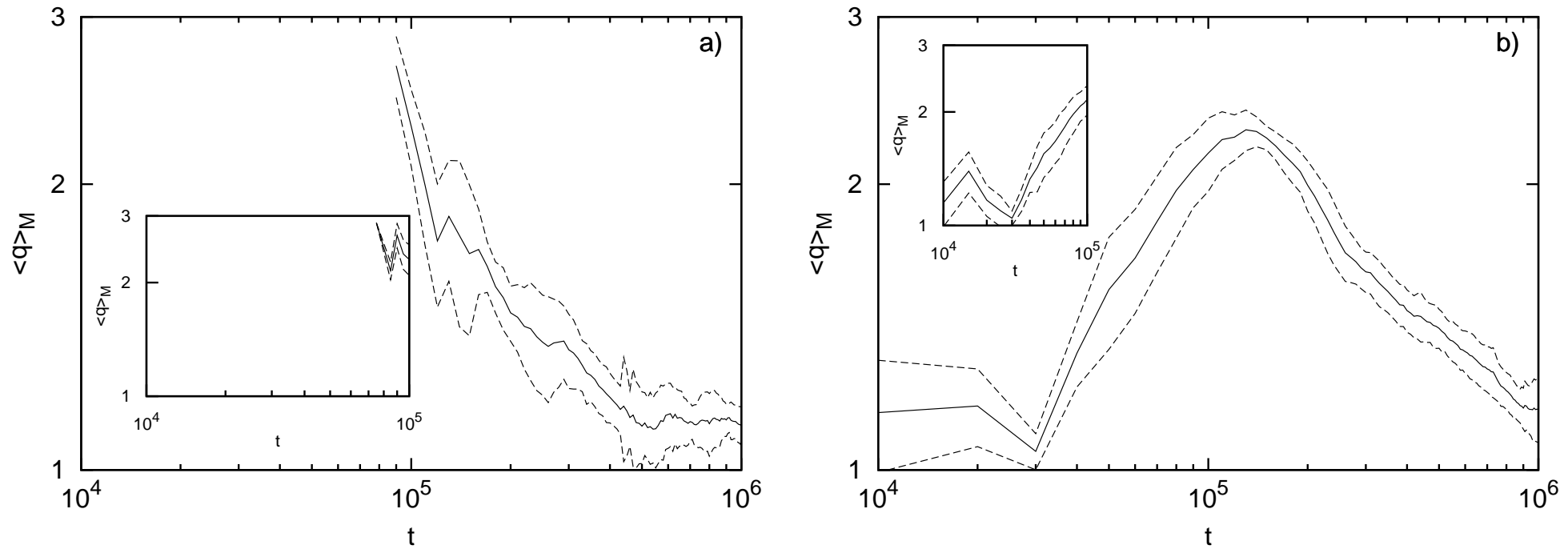
Figure 30: The time evolution of the $\langle q \rangle_M$-entropic parameter of the **Weakly Chaotic Orbit 2** of the 3DOF system (31) for $\eta = x + y$, $N_{ic} = 20000$ and $M = 50, 100, \ldots, 450, 500$. The dashed lines corresponds to one standard deviation from the average entropic parameter. The inset is a zoom-in up to $t_f = 10^5$. Panel b): Same as in panel a) but for $\eta = z$. These results have been verified by Fourier spectra calculations.

QSS and Dynamical Phase Transitions in a Microplasma System

We now turn our attention to another N degree of freedom Hamiltonian system of very different type than the FPU models, as **it is characterized by long range interactions of the Coulomb type** and study statistically the dynamics during the transition **from "crystalline–like" to "liquid–like"** phase (the so called "melting transition") for small energies and also **from "liquid–like" to "gas–like"** phase at higher energies. We consider a microplasma of N ions of equal mass $m = 1$ and electric charge Q in a Penning trap with electrostatic potential

$$\Phi(x, y, z) = V_0 \frac{2z^2 - x^2 - y^2}{r_0^2 + 2z_0^2} \tag{38}$$

and constant magnetic field along the z direction with a vector potential of the form

$$\mathbf{A}(x, y, z) = \frac{1}{2}(-By, Bx, 0). \tag{39}$$

The system is described by the Hamiltonian

$$\mathcal{H} = \sum_{i=1}^{N} \left\{ \frac{1}{2m}(\mathbf{p}_i - q\mathbf{A}(\mathbf{r}_i))^2) + Q\Phi(\mathbf{r}_i) \right\} + \sum_{1 \leq i < j \leq N} \frac{Q^2}{4\pi\epsilon_0 r_{ij}} \tag{40}$$

Here $\mathbf{r_i}$ is the position of the ith ion, r_{ij} is the Euclidean distance between the ith and jth ions and ϵ_0 is the vacuum permittivity. The ions are subjected to a **harmonic confinement in the z direction** with frequency

$$\omega_z = \sqrt{\frac{4QV_0}{m(r_0^2 + 2z_0^2)}} \tag{41}$$

while, in the perpendicular direction, they rotate with frequency $\omega_c = QB/m$. Thus, in a frame rotating around the z axis with Larmor frequency $\omega_L = \omega_c/2$, the ions are subjected to a **harmonic confinement** with frequency $\omega_x = \omega_y = \sqrt{\frac{\omega_c^2}{4} - \frac{\omega_z^2}{2}}$ in the direction perpendicular to the magnetic field. In the rescaled time $\tau = \omega_c t$, position $\mathbf{R} = \mathbf{r}/a$ and energy $H = \frac{\mathcal{H}}{m\omega_c^2 a^2}$ with $a = \left(\frac{Q^2}{4\pi\epsilon_0 m \omega_c^2}\right)^{\frac{1}{3}}$, the Hamiltonian (40) describing the motion of the N ions takes the form

$$H = \sum_{i=1}^{N}\left[\frac{1}{2}\mathbf{P}_i^2\right] + \sum_{i=1}^{N}\left[\left(\frac{1}{8} - \frac{\gamma^2}{4}\right)(X_i^2 + Y_i^2) + \frac{\gamma^2}{2}Z_i^2\right] + \sum_{i<j}\frac{1}{R_{ij}} = E \tag{42}$$

where E is the total conserved energy of the system, $\mathbf{R}_i = (X_i, Y_i, Z_i)$ and $\mathbf{P}_i = (P_{X_i}, P_{Y_i}, P_{Z_i})$ are the positions and momenta in $\mathbb{R}^3$, R_{ij} is the Euclidean distance between different ions i, j given by

$$R_{ij} = \sqrt{(X_i - X_j)^2 + (Y_i - Y_j)^2 + (Z_i - Z_j)^2} \tag{43}$$

and $\gamma = \omega_z/\omega_c$. The ions perform **bounded motion under the condition**

$$0 < |\gamma| < \frac{1}{\sqrt{2}}. \tag{44}$$

The trap is called prolate if $0 < |\gamma| < \frac{1}{\sqrt{6}}$, isotropic if $|\gamma| = \frac{1}{\sqrt{6}}$ and oblate if $\frac{1}{\sqrt{6}} < |\gamma| < \frac{1}{\sqrt{2}}$. Thus, **the motion is quasi 1–dimensional in the limit** $\gamma \to 0$ and quasi 2–dimensional in the limit $\gamma \to 1/\sqrt{2}$. The Z direction is a symmetry axis and hence, the Z component of the angular momentum $L_Z = \sum_{i=1}^{N} X_i P_{Y_i} - Y_i P_{X_i}$ is conserved. We suppose, from now on $L_Z = 0$) and that the motion is studied in the Larmor rotating frame.

Recent results demonstrate **the occurrence of dynamical regime changes** when the system is in a prolate **quasi 1–dimensional configuration ($\gamma = 0.07$)**. More specifically, in the **lower energy regime**, a transition from a "crystalline–like" to a "liquid–like" behavior is observed, **called the "melting phase"**. It appears that there is no clear "macroscopic" approach for identifying and studying the "melting" process of the microplasma system in detail.

However, using the **Smaller Alignment Index (SALI) method** to study the local dynamics, we discovered that **there exists an energy range E_{mt} of weakly chaotic behavior**, i.e. $E \in E_{\mathsf{mt}} = (2, 2.5)$, where **the positive Lyapunov exponents are very small** and SALI exhibits a stair–like decay to zero with varying decay rates, due to the presence of long lived "sticky" orbits near the boundaries of resonance islands.

Thus, we set $\gamma = 0.07$ and consider a prolate trap giving rise to **quasi 1–dimensional motion** for the case of $N = 5$ **ions**. For these parameters, the minimum energy for the ions to start moving around their equilibrium positions is $E_0 \approx 1.8922$.

We first study **the "melting transition"**, as the energy of the Hamiltonian (42) increases above E_0, from the viewpoint of probability distributions associated with chaotic trajectories. Based on the results of the previous sections, we expect to find q–Gaussians with $1 < q < 3$ in the vicinity of E_{mt} where the positive Lyapunov exponents $\lambda_i, \ i = 1, \ldots, 3N$ are quite small compared to the maximum values they can attain. This is also expected since in the interval E_{mt} the orbits stick to the boundaries of islands, at the so called **"edge of chaos"** [Tsallis, 2009].

Indeed, in Figure 31, we apply our statistical analysis to the microplasma system, taking $N_{ic} = 1000, M = 1000, t_f = 2 \times 10^7$ as integration time for our orbits and **using as an observable the quantity** $\eta(t) = X_1(t)$, i.e. the first component of the position $\mathbf{R}_1$ of the first ion. We find that, in the energy range of the "melting transition", the values of the entropic parameter of the q–Gaussian distribution (14) exhibiit **a maximum well above** $q = 1$, indicating that the statistics is not Gaussian. Rather, a q–Gaussian is detected, which persists up to about $E = 4.5$.
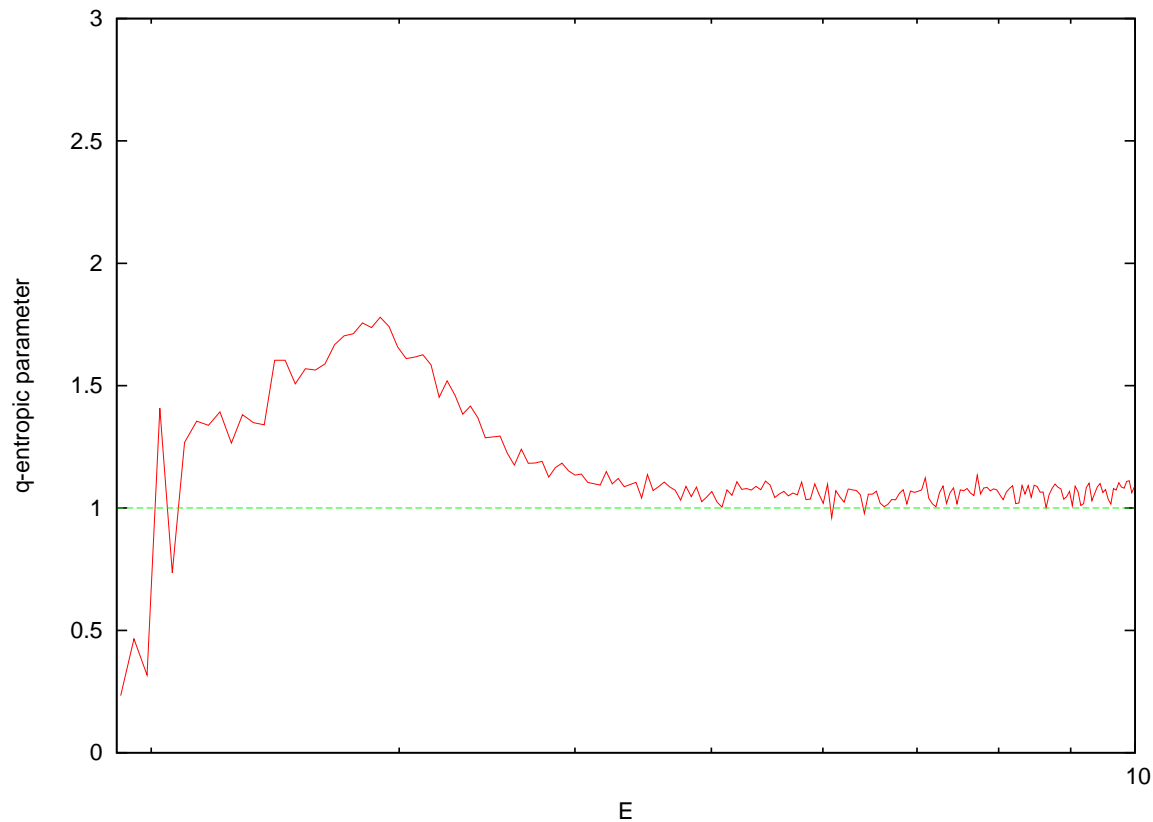
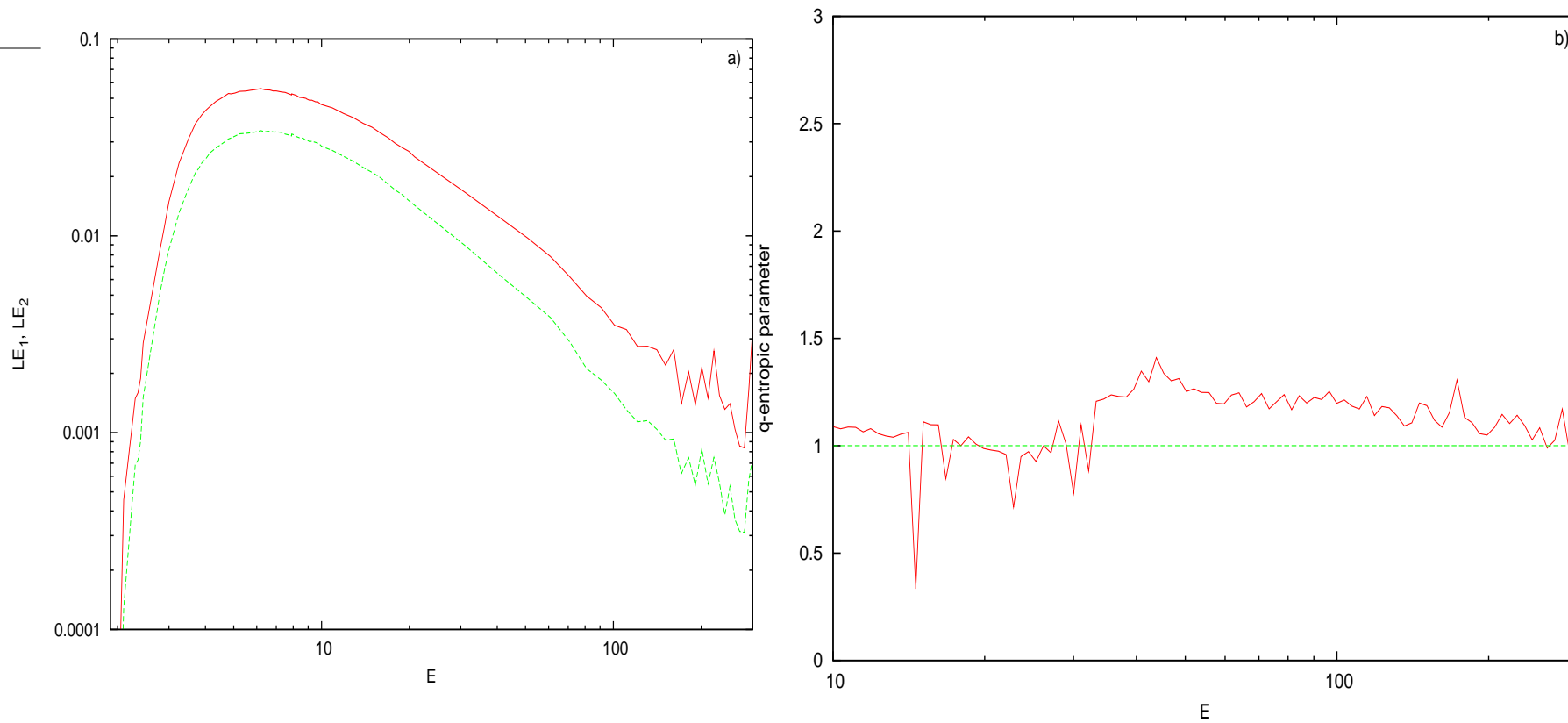**Figure 31:** Plot of the q–entropic parameter as a function of the energy E of the microplasma Hamiltonian (42) for $\gamma = 0.07$ (prolate trap) and $N = 5$ ions. In this plot, we have used $N_{\mathsf{ic}} = 1000$ and $M = 1000$. We have also plotted the line at $q = 1$ for reference to the entropic parameter of the Gaussian distribution.

Finally, we study a **second transition from "liquid–like" to "gas–like"** behavior, where the system is "weakly chaotic" at higher energies, where the biggest Lyapunov exponents decrease towards zero according to the equation [see Gaspard, 2003]

$$\mathsf{LE}_1 \sim \left\langle \frac{N^2}{R_{ij}^3} \right\rangle \sim N \frac{(\ln T)^{1/2}}{T^{3/4}} \tag{45}$$

where T is defined as $T = \frac{k_B \mathcal{T}}{m \omega_c^2 a^2}$, with $\mathcal{T}$ being the temperature of the system. This formula represents the asymptotic power law decay of the biggest Lyapunov exponent for sufficiently high energies (well above its peak at $E \approx 6$), see Figure 32(a).

As Figure 32(b) shows, **the q indices are well above unity for 30<E<200** indicating that in this range a significant dynamical change occurs. The energy increase drives the system to a more organized state favoring the kinetic part rather than the Coulomb part and leading to a regime characterized by few rare particle encounters, much like in an "ideal gas".

Figure 32: Panel a) Plot of the two biggest positive Lyapunov exponents (LE_1 with red color and LE_2 with green color) as a function of the energy E in log–log scales. We observe that, after their peak values at $E \approx 6$, both of them decay to zero according to the formula (45). Panel b) Plot in log–linear scales of the q–entropic parameter as a function of E for $\gamma = 0.07$ (prolate trap) and $N = 5$ ions. In this plot, we have used $N_{\text{ic}} = 1000$ and $M = 1000$.

Conclusions

1. At **"weakly chaotic regimes"** located at the boundaries of islands of quasiperiodic motion of **Hamiltonian systems**, probability density functions (pdfs) of sums of chaotic variables, are **well approximated by q–Gaussians**.

2. These q–Gaussians are in fact **Quasi–Stationary States** (QSS) which **last for long times** and often pass through **different stages** to **exponential and finally to Gaussian form**.

3. In some cases, however, it is possible to find that the orbits **converge to a specific QSS**, whose pdf is **close to a q–Gaussian**, at least over its central part.

4. QSS approximated by q–Gaussians can be used to **identify weakly from strongly chaotic orbits** in **models of barred galaxies** over realistically **short time intervals**, where other methods, like Fourier analysis and Lyapunov exponents are not very helpful.

5. These results are also observed in **low–dimensional conservative maps** and multi-dimensional Hamiltonian systems **independent of the number of degrees of freedom**.

References

1. Tsallis, C. [2009], "Introduction to Nonextensive Statistical Mechanics: Approaching a Complex World", *Springer, New York*.

2. Antonopoulos, C., **Bountis, T.** and Basios, V. [2010], "Quasi–Stationary States in Multidimensional Hamiltonian Systems", PRE **81**, 016211.

3. Ruiz Lopez G., **Bountis, T.** and Tsallis, C. [2011], "Time–Evolving Stastistics of Chaotic Orbits in Conservative Maps in the Spirit of the Central Limit Theorem", Intern. J. Bifurc. Chaos, Vol. **22** (9), pp. 12502.

4. Bountis, T. and Skokos, H. [2012], *Complex Hamiltonian Dynamics*, Springer Verlag Synergetics Series, Springer Verlag, Berlin.

5. Bountis, T., Manos, Th. and Antonopoulos Ch [2012], "Complex Statistics in Hamiltonian Barred Galaxy Models", Celestial Mechanics and Dynamical Astronomy, **113**, Issue 1 (2012), Page 63-80.

6. Leo, M. and Leo, R. A. and Tempesta, P. [2010], "Thermostatistics in the Neighborhood of the π–mode Solution for the Fermi–Pasta–Ulam β System: From Weak to Strong Chaos", *J. of Stat. Mech.: Th. & Exp.*, **04**, pp. 04021.

7. Antonopoulos, Ch., **Bountis, T.** and Skokos, Ch., [2006],"Chaotic Dynamics of N–Degree–of–Freedom Hamiltonian Systems", *International Journal of Bifurcation and Chaos*, vol.**16**(6), 1777-1793 , June 2006.

8. Antonopoulos, Ch. and **Bountis, T.**, [2006], "Stability of Simple Periodic Orbits and Chaos in an FPU Lattice", PRE**73**, 056206, 1-8 (2006).

COMPLEX HAMILTONIAN DYNAMICS AND STATISTICS

T. Bountis[1], Ch. Antonopoulos[2], H. Skokos[3], H. Christodoulidi[1] and C. Tsallis[4]

[1]Department of Mathematics, University of Patras, Patras, Greece
[2]Institute for Complex Systems and Mathematical Biology, University of Aberdeen
[3]Department of Physics, University of Thessaloniki, Greece
[4]Centro Brasileiro de Pesquisas Fisicas, Rio de Janeiro-RJ, Brazil

Lecture 4:

Chaotic Diffusion and the Role of Long Range Interactions

Workshop and Latin–American School on "Foundations of Complexity"

Rio de Janeiro, Brasil, October 4–30, 2015

Contents

Complex Dynamics and Statistics in a Disordered KG Chain

One fundamental issue in condensed matter physics is the study of **conductivity of electrons in solids**. What happens in realistic situations when **disorder is present** in the crystal due to **impurities or defects?**

How does disorder affect conductivity? This question was first answered by Philip Anderson, who showed that **if disorder is large enough the diffusive motion of the electrons will eventually stop (Anderson localization)**.

Anderson's analysis, however, is based on a linear model that can be represented in one dimension by the time-dependent Schrödinger equation

$$i\frac{\partial \psi_l}{\partial t} = \epsilon_l \psi_l - \psi_{l+1} - \psi_{l-1}, \tag{1}$$

where ϵ_l are **the random on-site energies, drawn from an uncorrelated uniform distribution in** $[-W/2, W/2]$, W parametrizes the disorder strength and ψ_l is the complex wave function associated with lattice site l.

So what is the effect of nonlinearity on the localization properties of wave packets in disordered systems?

Many studies have shown that an initially localized wave packet spreads subdiffusively and chaotically for moderate nonlinearities. **For weak nonlinearities, on the other hand, wave packets have been shown to "freeze"** over the available integration time, thereby resembling Anderson localization.

In fact, it was conjectured by Johansson, Aubry et al. 2010 that these states **will be localized for long enough times on some Kolmogorov-Arnold-Moser (KAM) torus**, since every particle's motion tends to become linear in that limit.

Based on our statistical analysis, we will argue that **KAM localization does not occur and chaotic diffusion persists for infinitely long times.**

In particular, **we study statistically diffusive motion** in a **disordered Klein Gordon (KG) one–dimensional lattice** of $N = 1000$ particles, treated extensively in the literature, with Hamiltonian

$$H_{KG} = \sum_{l=1}^{N} \frac{p_l^2}{2} + \frac{\tilde{\epsilon}_l}{2} x_l^2 + \frac{1}{4} x_l^4 + \frac{1}{2W} (x_{l+1} - x_l)^2 = E, \qquad (2)$$

where x_l and p_l are the positions and momenta on site l, and $\tilde{\epsilon}_l$ are chosen uniformly from the interval $\left[\frac{1}{2}, \frac{3}{2}\right]$.

We examined two different regimes:

1) **The low energy (sub–diffusive regime)**

2) **The higher energy (self–trapping regime)**,

using **two representative examples of energies,** $E = 0.4$ **and** $E = 1.5$ **and integrated the KG chain using a fourth order Yoshida's symplectic integrator**.

We analyze normalized energy distributions $z_\nu \geq 0$ defined by

$$z_\nu \equiv E_\nu / \sum_\mu E_\mu \qquad (3)$$

where $\bar{\nu} = \sum_\nu \nu z_\nu$ and E_ν is the νth normal mode energy. **We then compute the time evolution of the second moment**

$$m_2 = \sum_\nu (\nu - \bar{\nu})^2 z_\nu, \qquad (4)$$

and the participation number

$$P = 1 / \sum_\nu z_\nu^2, \qquad (5)$$

Starting with very narrow packets, the wave diffuses **always chaotically**, both in the low energy (diffusive) regime, as well as in the higher energy (self–trapping) regime, with **the second moment following the law** $m_2 \sim t^\alpha$ **with** $\alpha \approx 1/3$ **for long times**.

Our statistical analysis showed that **weak chaos converges quickly to strong chaos**, for times up to 10^9 and thus we conclude that the dynamics does **not relax onto a quasiperiodic KAM torus** and **diffusion spreads chaotically for arbitrarily long times**.

We plot the q-Gaussian pdfs and focus on the **time evolution of the q entropic parameter for a class of observables**, starting from the central particle (i.e. $\eta_1 = x_{500}$) and **taking into account more and more sites**, i.e.:

- $\eta_1 = x_{500}$

- $\eta_5 = x_{498} + \ldots + x_{502}$

- $\eta_9 = x_{496} + \ldots + x_{504}$

- $\eta_{19} = x_{491} + \ldots + x_{509}$

- $\eta_{29} = x_{486} + \ldots + x_{514}$

- $\eta_{39} = x_{481} + \ldots + x_{519}$

- $\eta_{1000} = x_1 + \ldots + x_{1000}$

In Figure 1 we show two representative examples of pdfs with different q entropic indices for **the low energy subdiffusive case, i.e.** $E = 0.4$. In panel (a) we plot the numerical distribution (dashed curve) for the observable η_1 computed in the time interval $[0, 10^8]$ and find that **it is well fitted by a q-Gaussian distribution** (solid thick curve) with $q_1 = 0.993 \pm 0.009$.

On the other hand, panel (b) which is the same plot as a), **for the observable η_{29}**, reveals a clear q-**Gaussian distribution, over nearly four decades** on the vertical axis, with $q_{29} = 1.22 \pm 0.01$.

Next, we present the pdfs **for the self-trapping case** $E = 1.5$ in Figure 2 keeping everything else the same as in Figure 1. We see that in this case not only **the entropic index q_1 but also q_{29} is even closer to the** $q = 1$ value of a Gaussian compared to that of Figure 1.
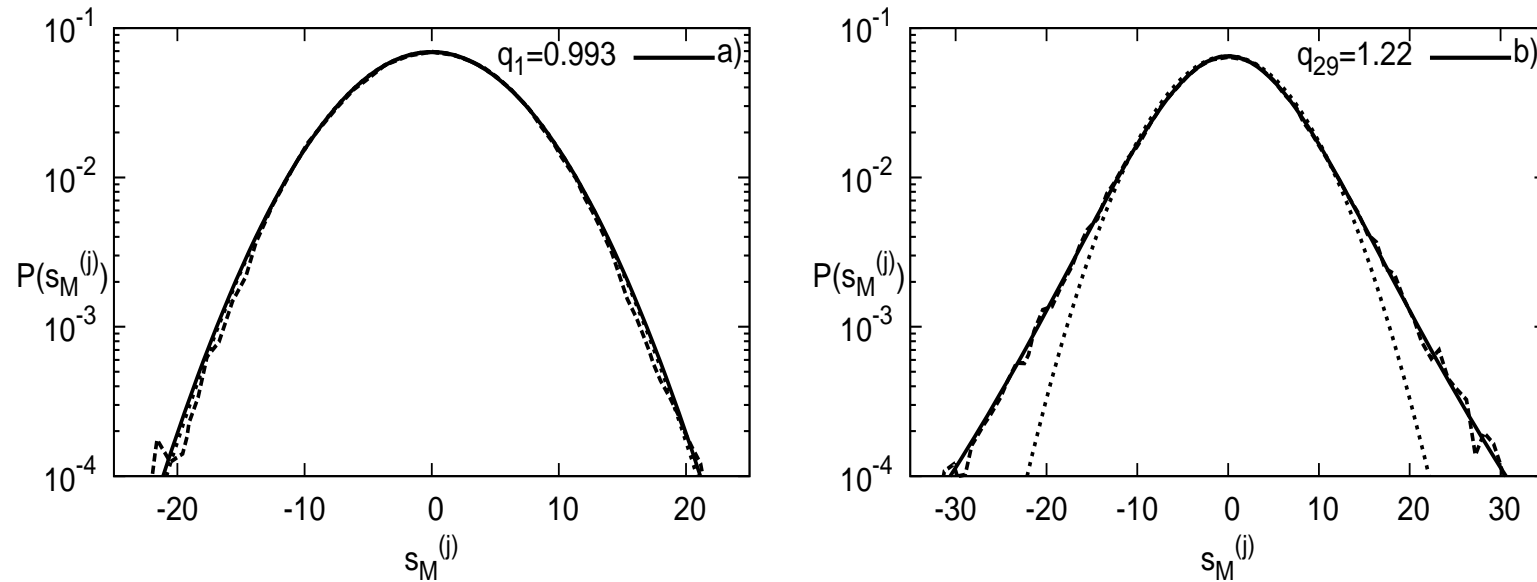
Figure 1. Panel a: Plot of the numerically computed pdf (dashed curve) for the observable η_1 **in the time interval** $[0, 10^8]$ **with** $q_1 = 0.993 \pm 0.009$ taken from fitting with a q-Gaussian distribution in solid thick. **Panel b**: Similar plot of the numerically computed pdf (dashed) for the observable η_{29} **and a time interval** $[0, 10^8]$ **with** $q_{29} = 1.22 \pm 0.01$. In both panels, $N = 1000$ and $E = 0.4$ **that corresponds to the subdiffusive case**.
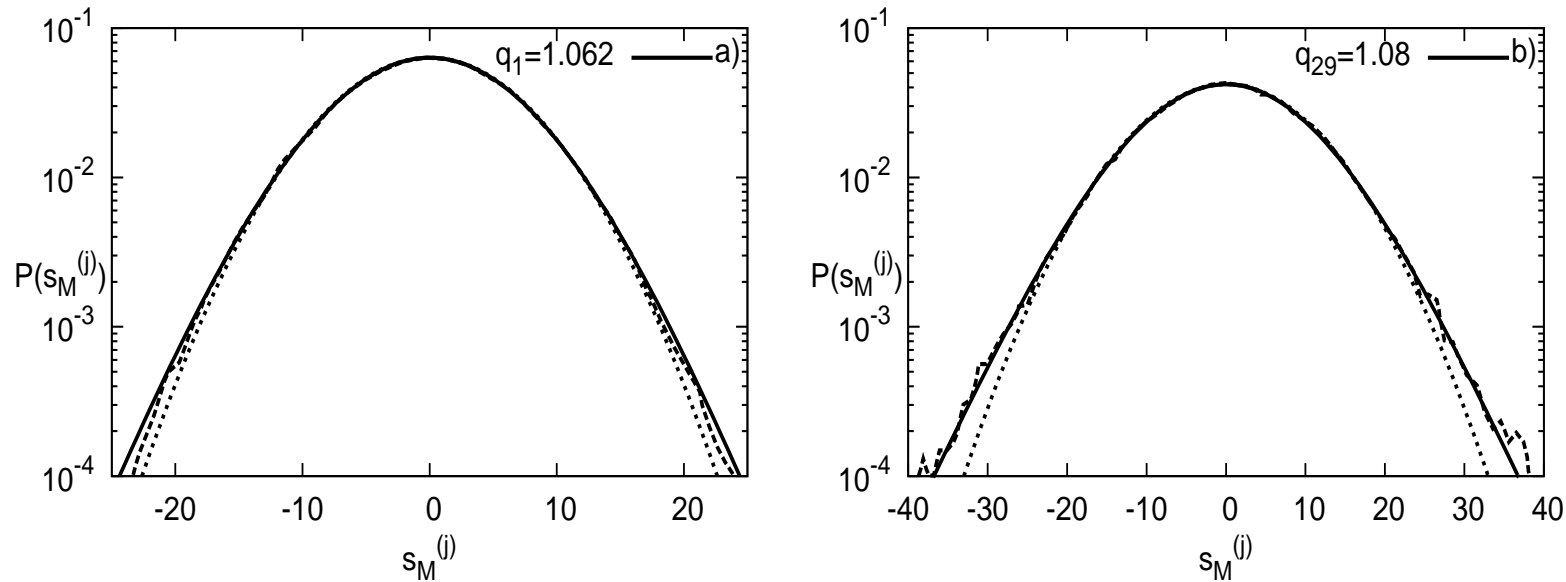
Figure 2. Panel a: Plot of the numerically computed pdf (dashed curve) **for η_1 in the time interval** $[0, 10^8]$ with $q_1 = 1.062 \pm 0.008$ fitted by a q-Gaussian distribution (solid thick curve). **Panel b**: Plot of the pdf (dashed curve) **for η_{29} and the time interval** $[0, 10^8]$ fitted by a q-Gaussian distribution (solid thick curve), with $q_{29} \approx 1.08 \pm 0.01$. In both panels, we use $N = 1000$ **and** $E = 1.5$ **belongs to the self-trapping regime**.

Next, in panel a) of Figure 3, **in the subdiffusive case ($E = 0.4$)**, the central 5 to 29 particles **initially perform a weakly chaotic motion** (although the q_1-q_{29} later decay towards 1). On the other hand, **if we study more particles with η_{39}, the motion is more chaotic** since the q index now tends more quickly to 1 at $t = 10^9$, while **for all particles (i.e. for η_{1000}) strong chaos becomes even clearer** as q_{1000} tends to 1 even more rapidly.

These results suggest that the behavior of **the central part of the lattice is more weakly chaotic**, while **the whole lattice behaves in a strongly chaotic way**. This is also shown in panel b) of Figure 3, where the three largest Lyapunov exponents initially decrease towards zero, but after $t = 10^5$ they jump to higher values and then decrease with a slope smaller than 1. Recently it was found that the maximum Lyapunov exponent λ_1 decreases as $\lambda_1 \propto t^{-0.25}$. This behavior is also seen in Figure 3 b).

From the results of Figure 3 b) it is evident that the evolution of these exponents is determined by the maximum Lyapunov exponent λ_1, as all of them show similar behaviors. As we see from panel c) of Figure 3, **the expected behavior of the second moment, i.e. $m_2 \propto t^{1/3}$, is also well reproduced** by our numerical results.
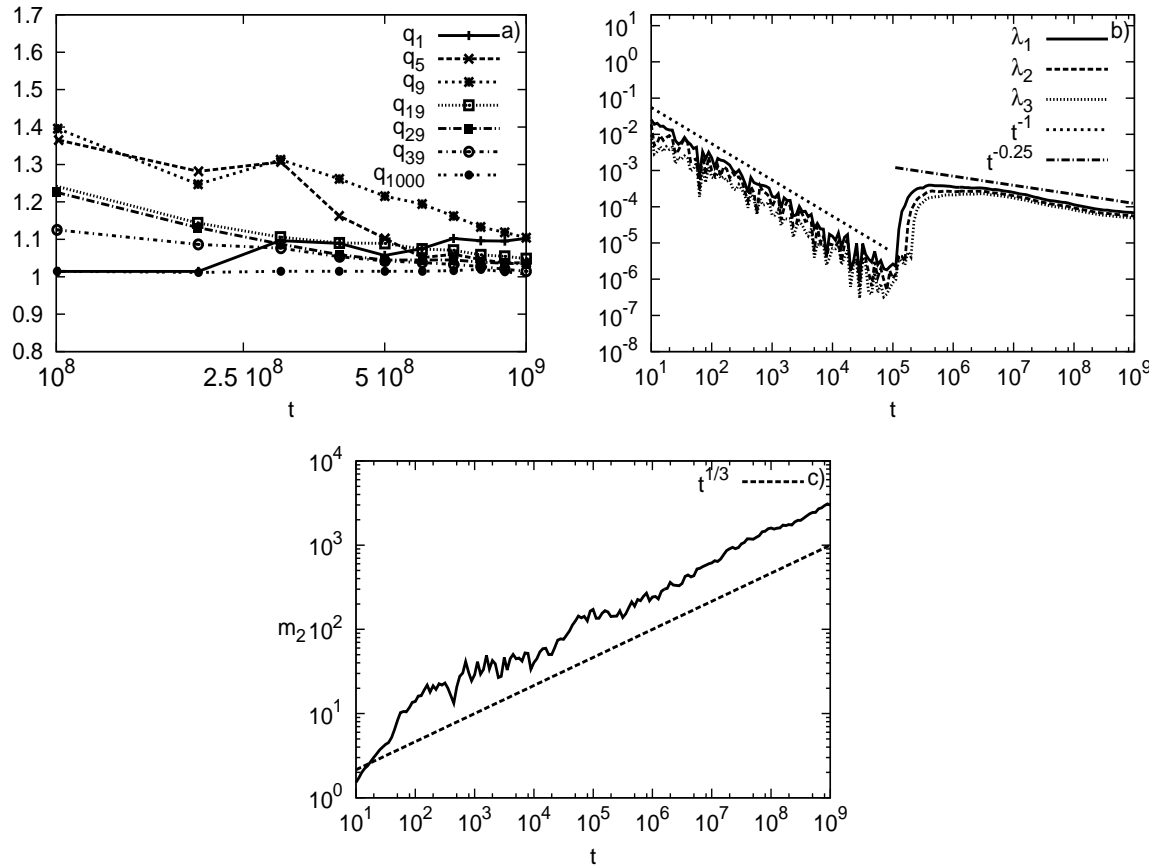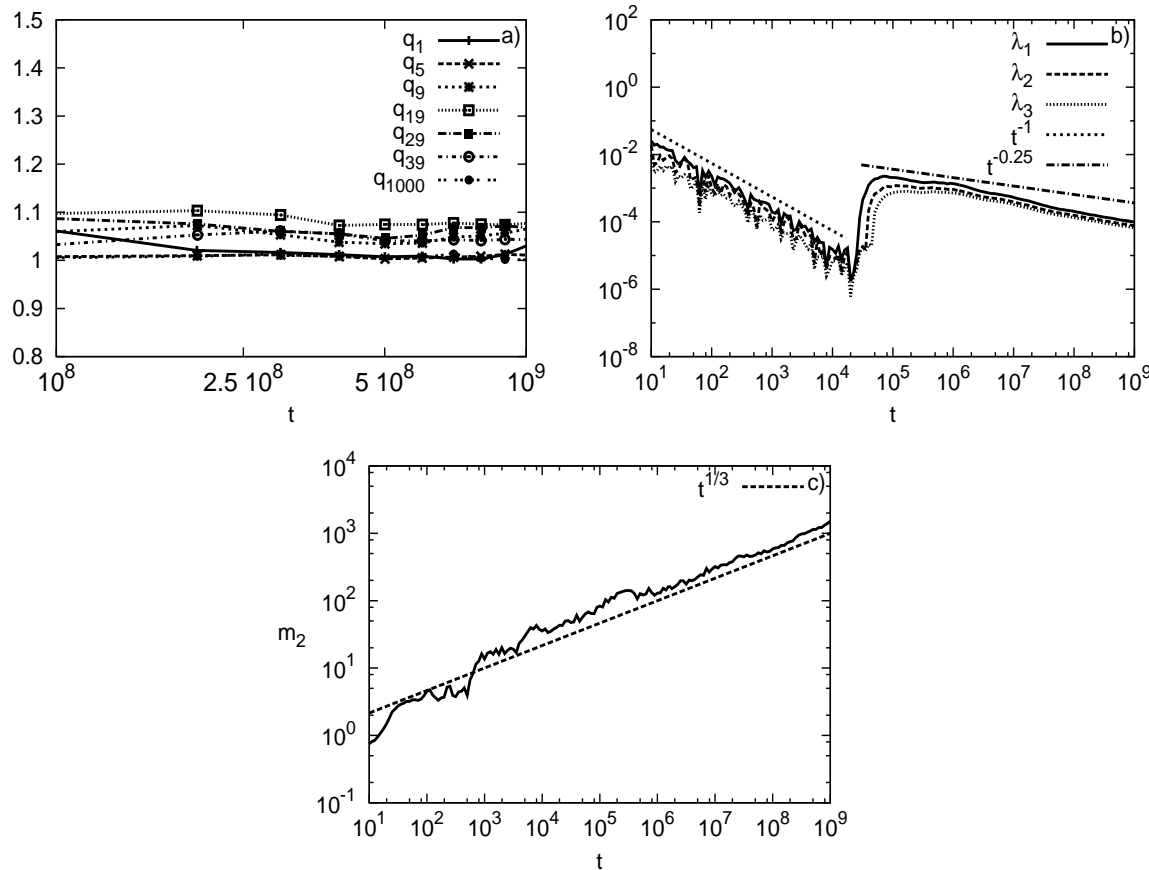
Figure 3. Panel a: Plot of the q entropic indices q_1, q_5, q_9, q_{19}, q_{29}, q_{39} and q_{1000} for $N = 1000$ and $E = 0.4$ **for the subdiffusive case**. **Panel b**: Plot of the corresponding three largest Lyapunov exponents λ_1, λ_2, λ_3, and of t^{-1}, $t^{-0.25}$ to guide the eye. **Panel c**: Plot of the second moment m_2 in time together with $t^{1/3}$ to guide the eye.

By contrast, **in Figure 4, where the same study is repeated for the higher energy $E = 1.5$ of the self-trapping case, the dynamics is somewhat different**. Panel a) shows that **all q entropic indices of Figure 3 are now much closer to 1**, even those of the central particles.

Comparing the three largest Lyapunov exponents in the two cases, we see that at the higher energy of the self-trapping case (which corresponds to stronger nonlinearity) they jump to higher values at about $t = 10^4$, i.e. one order of magnitude, and do so earlier than in the case of the lower energy of the subdiffusive case.

After that point, the Lyapunov exponents start decaying to zero but a bit faster than the one ($\propto t^{-0.25}$) observed in the subdiffusive case of Figure 3. We note again that m_2 **grows again in time as** $t^{1/3}$ as can be evidenced in panel c) of Figure 4.

Figure 4. Panel a: Plot of the q entropic indices q_1, q_5, q_9, q_{19}, q_{29}, q_{39} and q_{1000} **for** $E = 1.5$ **of the self-trapping**. **Panel b**: Time plot of the three largest Lyapunov exponents λ_1, λ_2, λ_3, and of t^{-1}, $t^{-0.25}$ to guide the eye. **Panel c)**: Plot of the corresponding second moment m_2 in time together with $t^{1/3}$ to guide the eye.

The FPU $\beta-$ Model With $1/r^\alpha$ Long Range Interactions

Let us now focus on the importance of introducing **long range interactions to a class of Fermi-Pasta-Ulam (FPU) $\beta-$models**, whose Hamiltonian is given by

$$\mathcal{H} = \frac{1}{2} \sum_{n=1}^{N} p_n^2 + \frac{1}{2} \sum_{n=0}^{N} (x_{n+1} - x_n)^2 +$$

$$+ \frac{b}{4\widetilde{N}} \sum_{n=0}^{N} \sum_{m=n+1}^{N+1} \frac{(x_n - x_m)^4}{|n - m|^\alpha} = U(N) \quad (b > 0; \; \alpha \geq 0), \quad (6)$$

with **fixed boundary conditions**, i.e. $x_0 = x_{N+1} = p_0 = p_{N+1} = 0$. **The quartic part of the potential energy scales with N as follows**

$$\widetilde{N}(N, \alpha) \equiv \frac{1}{N} \sum_{i=0}^{N} \sum_{j=i+1}^{N+1} \frac{1}{(j - i)^\alpha} = \frac{1}{N} \sum_{i=0}^{N} \frac{N + 1 - i}{(i + 1)^\alpha} \quad (7)$$

The $\widetilde{N}$ scaling is introduced in the Hamiltonian so as to make **the kinetic as well as both parts of the potential energy extensive (i.e. proportional to N)** for all values of α.

There are two important limits in the extremal cases:

(i) **The long range limit** $\alpha \to 0$: Each particle interacts equally with all others independently of the distance between them and

(ii) **The short range limit** $\alpha \to \infty$: Only interactions with nearest neighbors apply, recovering exactly the Hamiltonian of the FPU-β model.

In the present study **we have implemented** **long range interactions only in the quartic part of the potential** in (6).We have found, however, that if this type of scaling **is also introduced in the quadratic terms the results are very similar**.

As initial conditions for integrating our trajectories, we always take zero positions and momenta drawn randomly from a uniform distribution.

Different Dynamics for $0 < \alpha < 1$ and $\alpha > 1$

We begin by computing **the largest Lyapunov exponent** λ_{max} for different values of α, N and specific energies $u = U(N)/N$. In Figure 5 we have plotted the λ_{max} versus the system size N for different α values, ranging from 0 to 10. **The critical value $\alpha = 1$**, as found by other researchers, clearly distinguishes between two different regimes:

i) **For $\alpha \geq 1$** the Lyapunov exponent λ_{max} **tends to stabilize at a finite and positive value** as N increases. So, for the system with short–range interactions in the thermodynamic limit λ_{max} depends only on ϵ and α.

ii) **For $\alpha < 1$** the Lyapunov exponent **is observed to decrease with system size as** $N^{-\kappa(\alpha)}$, where the dependence of the exponent $\kappa(\alpha)$ on α is shown in the inserted panel of Figure 5.

We therefore expect that the system **with short–range interactions tends to a BG equilibrium in the thermodynamic limit**, while **long–range dynamics is associated with a weaker form of chaos**.
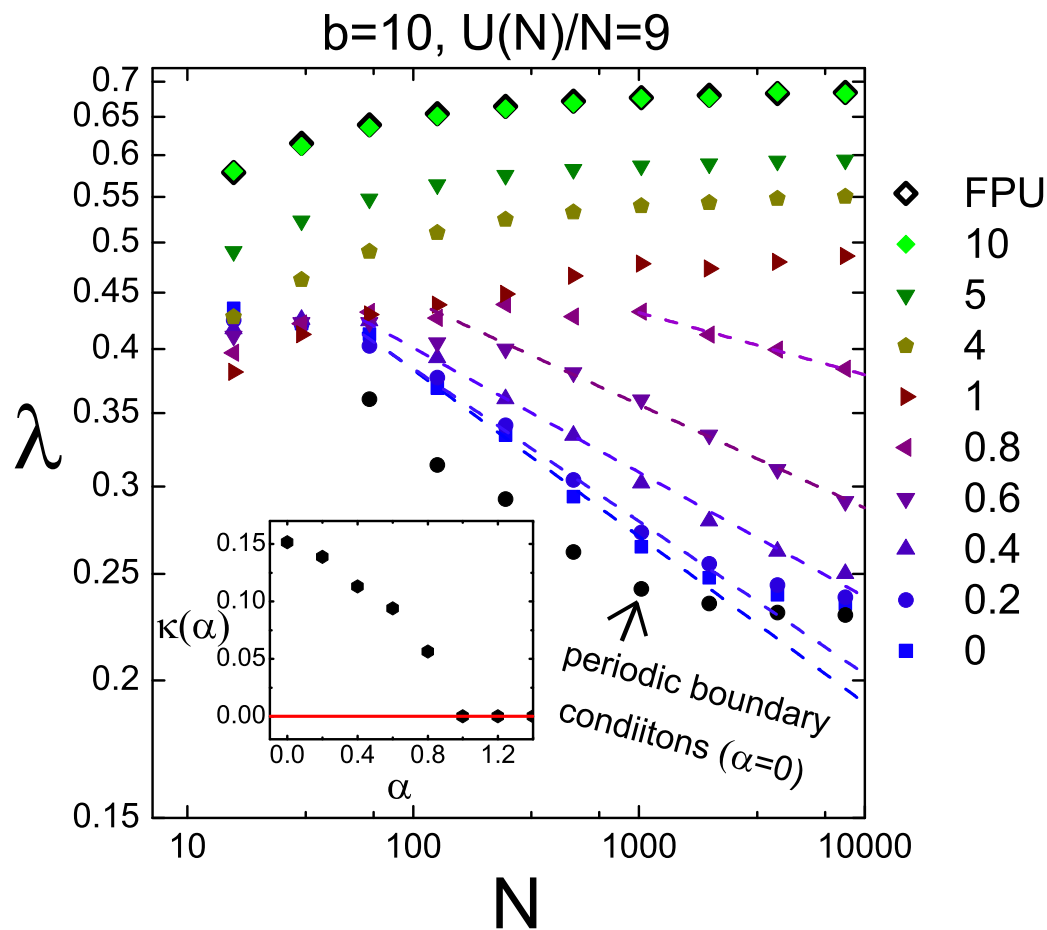
Figure 5: Maximal Lyapunov exponent for increasing N and various values of α, when $U(N)/N = 9$, and $b = 10$ calculated at $t = 10^6$ for fixed boundary conditions. Note, as shown in the insert, that $\lambda_{max} \propto N^{-\kappa(\alpha)}$.

# Different Statistics for $0 < \alpha < 1$ and $\alpha > 1$

Plotting now momentum distributions of orbits, we find **in the case of long–range interactions a quasi–stationary state (QSS) is formed** **with a q–Gaussian probability density function (pdf) of the momenta**, with $1 < q < 3$.

The histograms shown on the left panel of Figure 6, **for $\alpha = 0.7$ are well fitted by the q–Gaussian pdf**:

$$P(p) = P(0)[1 + \beta(1 - q)(pP(0))^2]^{1/(1-q)}, q \geq 1. \tag{8}$$

with $q = 1.249$. This figure was produced for two time intervals $(10^5 - 5 \times 10^5)$ and $(4 \times 10^5 - 8 \times 10^5)$, for which q is nearly constant.

For times longer than $t = 10^6$, q **slowly decreases as a power law in time and tends to the value 1, which explains why this is a QSS**. In Figure 6(b), on the other hand, **the distribution for the interaction with $\alpha = 1.4$ follows from the beginning a pure Gaussian pdf** ($q \to 1$ in (8)) with $\beta = 0.043$.
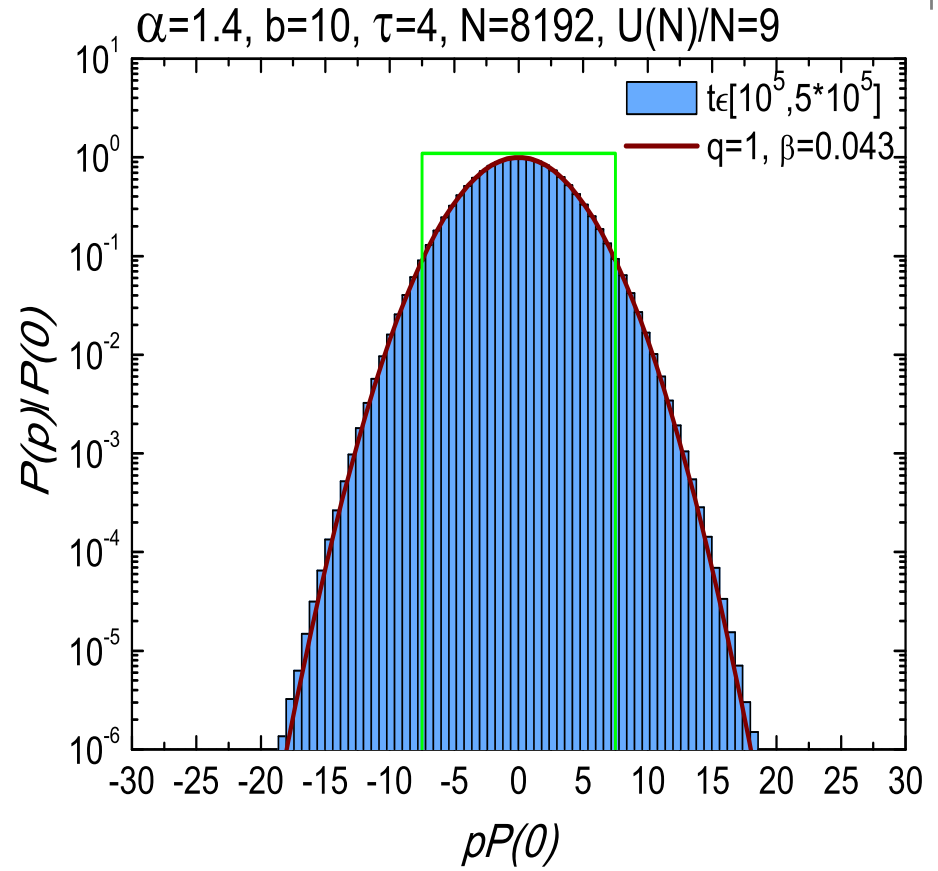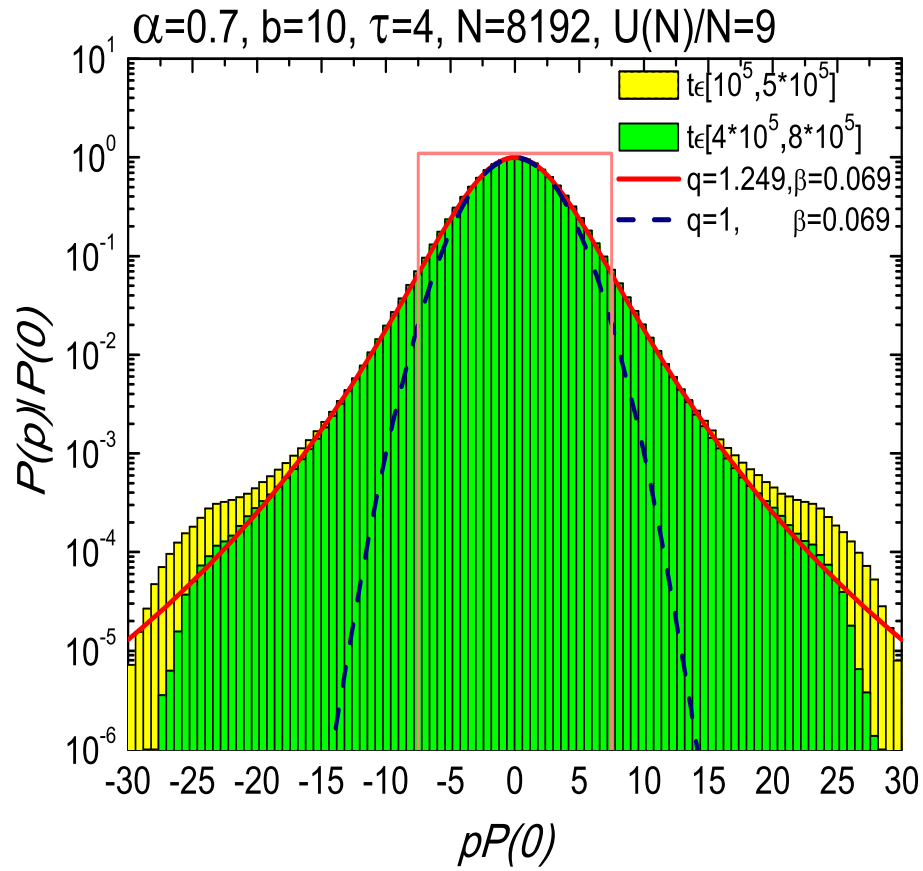
Figure 6: Momentum distributions for the system with $N = 8192$ and: (a) $\alpha = 0.7$ in two time intervals, (b) $\alpha = 1.4$.

The q–dependence on α in Figure 7 clearly shows that **the transition from q–statistics to BG–statistics is evident as α exceeds 1**. The data of Figure 7 is averaged over several realizations. Increasing N we observe that the q values shift upward somewhat but the overall qualitative picture remains the same.

To check the robustness of our results, **we have computed the q-generalized kurtosis of the distribution** defined as follows:

$$\kappa_q(q) = \frac{\int_{-\infty}^{\infty} dp \, p^4 [P(p)]^{2q-1} / \int_{-\infty}^{\infty} dp \, [P(p)]^{2q-1}}{3 \left[\int_{-\infty}^{\infty} dp \, p^2 [P(p)]^q / \int_{-\infty}^{\infty} dp \, [P(p)]^q \right]^2} \tag{9}$$

Using the q values found in Figure 7, we show in Figure 8 that **the numerical dependence of q-kurtosis on q compares very well with the analytical curve $\kappa_q(q) = (3-q)/(1+q)$** obtained by substituting the q-Gaussian pdf (8) in Eq. (9).
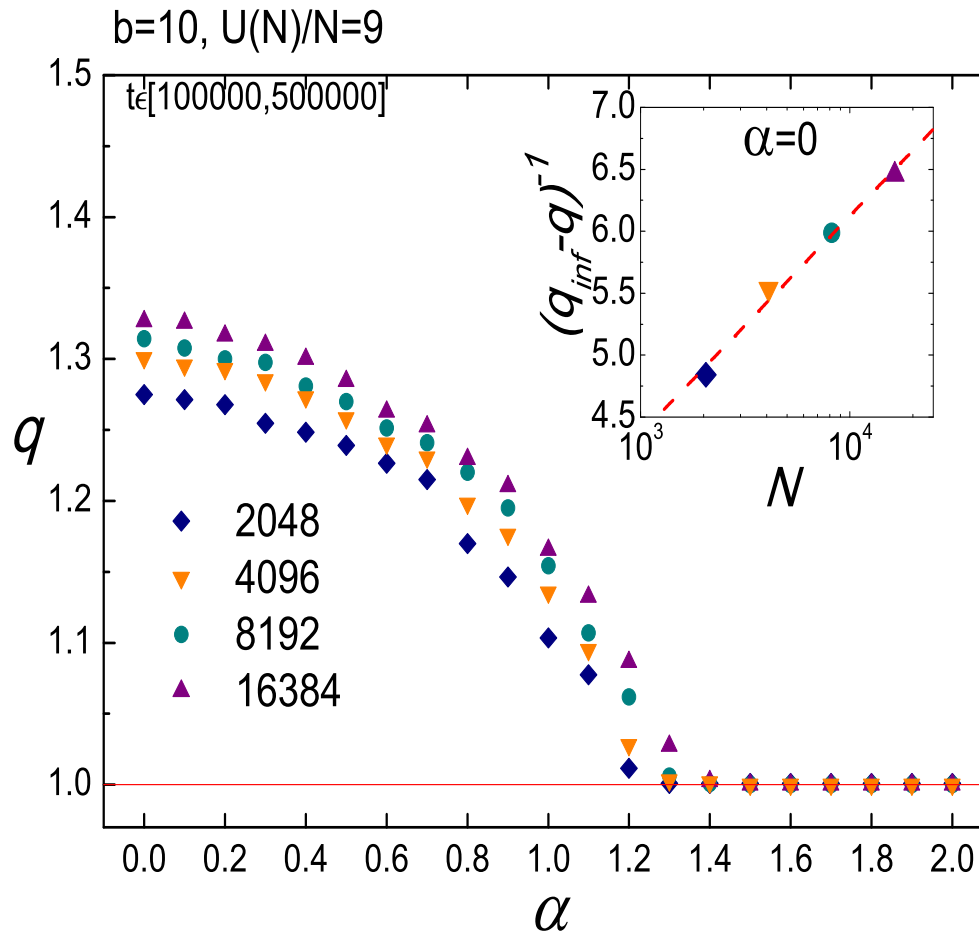
Figure 7: α-**dependence of the index** q **for** $b = 10$ **and** $U(N)/N = 9$ averaged over 4 independent realizations when N is 2048, 4096, 8192 and 2 realizations for $N = 16384$, all taken in the time interval $t \in [5 \cdot 10^5, 9 \cdot 10^5]$. Inserted panel shows the line $(q_\infty - q)^{-1} = 1.76 \log N - 0.9$, for the data of the main figure with $\alpha = 0$.
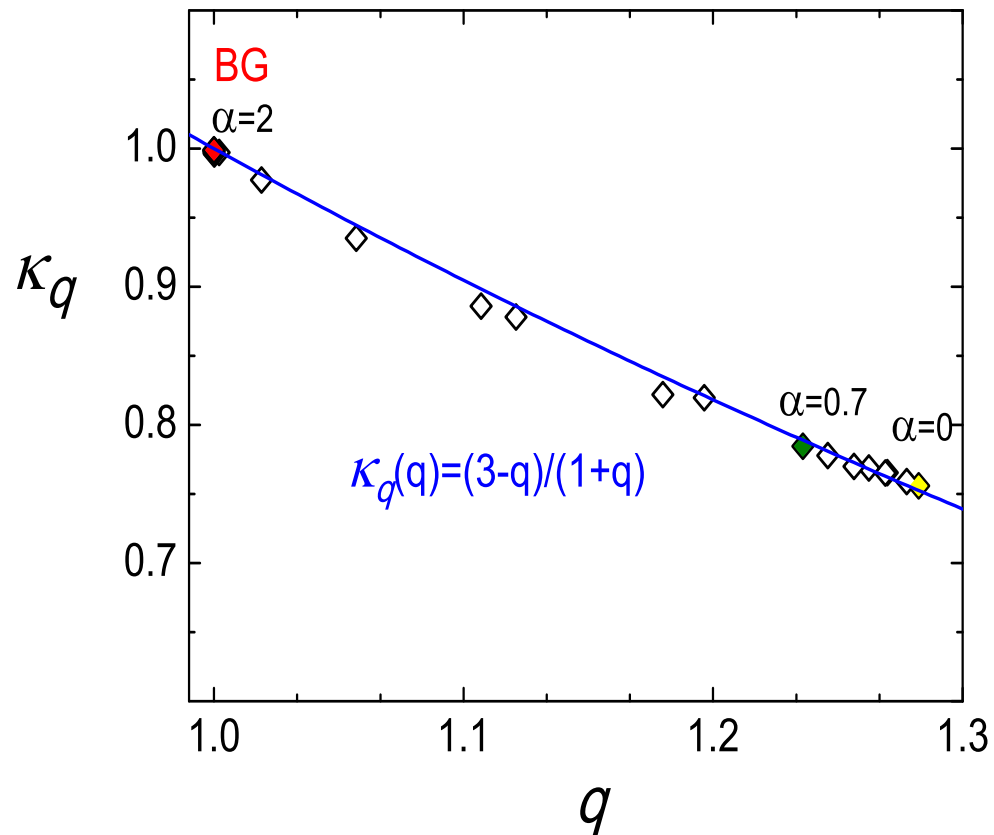
Figure 8: q-**dependence of the** q-**kurtosis** κ_q for typical values of α, together with the analytical prediction $\kappa_q = (3-q)/(1+q)$ (blue curve) for the data of Figure 7 and $N = 8192$.

A "Phase Diagram" Separating BG from q-Statistics

Figure 9(b) displays the **crossover between the two regimes in the form of a "phase diagram"**, in which a straight line fit of the data separates the two "phases" in the $1/N$ vs. $1/t_c^\gamma$ plane. Each point in the graph of Figure 9(b) corresponds to a value of $t = t_c$ representing the maximum time that q remains constant, after which q tends to the BG value $q = 1$ following a power law, as shown in Figure 9(a).

For high nonlinearity strength $b = 10$ the line separating the two domains has a big slope and **the region of BG statistics is rather limited** in the upper part of the diagram. However, **when we decrease the nonlinearity to** $b = 2$ the slope of the boundary decreases and **the BG domain becomes wider**.

As a final remark, we point out the **nonuniformity of the** $(N, t) \to (\infty, \infty)$ **limit** implied by the diagram of Figure 9(b). Clearly, in the $\lim_{N \to \infty} \lim_{t \to \infty}$ ordering it is the $q = 1$ behavior that prevails, while in the $\lim_{t \to \infty} \lim_{N \to \infty}$ ordering it is the $q > 1$) statistics that becomes dominant.
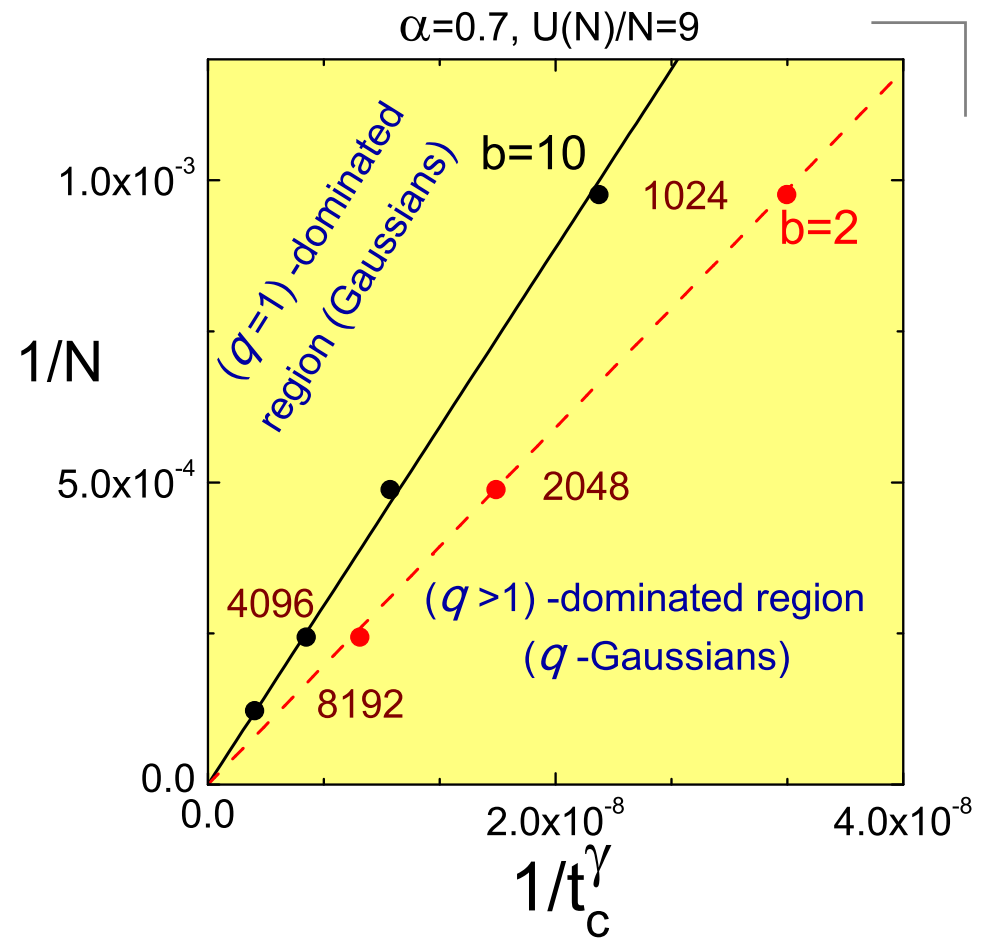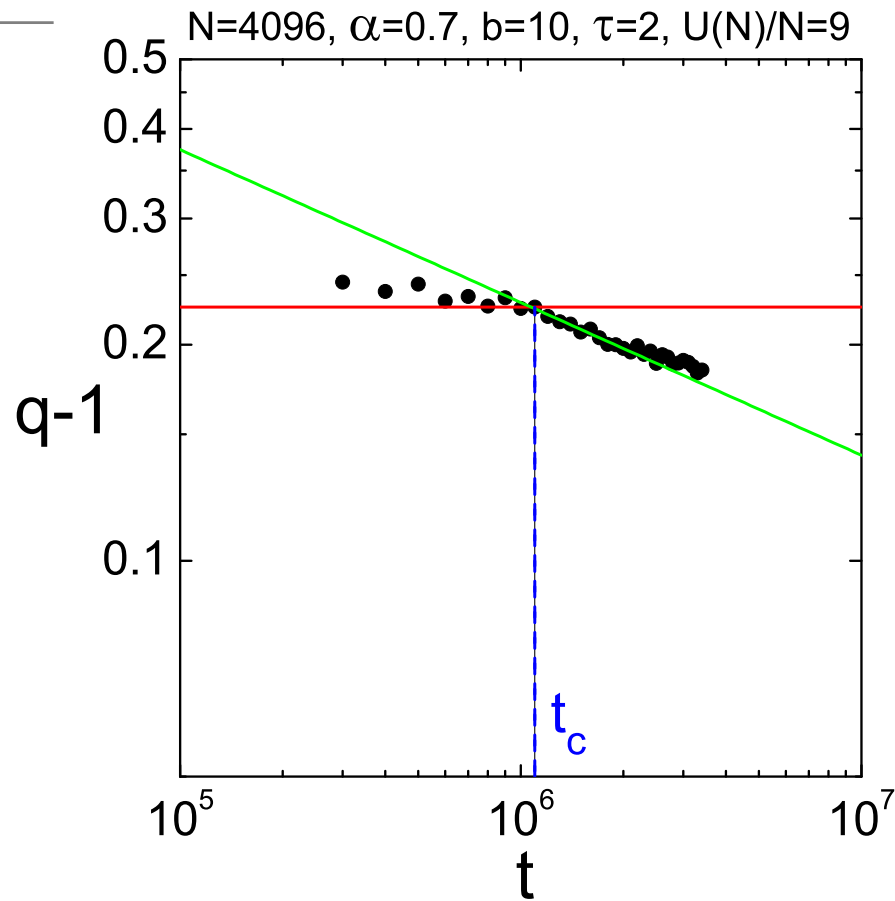
Figure 9: (a) **Evolution of $q - 1$ in double logarithmic scale**. Each point corresponds to time averaged results over a window $2 \cdot 10^5$. **Note that the QSS lasts for times up to t_c.** (b) Crossover frontiers between Gaussian and q-Gaussian thermostatistics.

A "Universal" Picture?

As we saw in Fig. 17(b), **for high nonlinearity strength** $b = 10$ the line separating the two domains has a large slope and the region of BG statistics is somewhat limited. However, **when we decrease the nonlinearity to** $b = 2$ **the slope of the boundary decreases** and the BG domain prevails over q-statistics.

The **crossover frontier** is approximatively given by

$$\frac{1}{N} \sim D(\alpha, u) \frac{b^{\delta}}{t_c^{\gamma}} \tag{10}$$

and may be plotted **as a single straight line**, yielding a "universal picture" of the nonextensive statistics valid for $alpha < 1$ (see Figure 10 below), with $D = 2.3818 \times 10^4$, $\delta = 0.27048$, and $\gamma = 1.365$.

Thus, for $\alpha < 1$, our evidence suggests that the system follows q-**statistics and forms quasi-stationary states (QSS)**, in a "weakly" (non–uniformly ergodic) subspace of the full phase space, where it lives for a very long time, **until it eventually enters a domain of "strong" chaos and uniform ergodicity**.
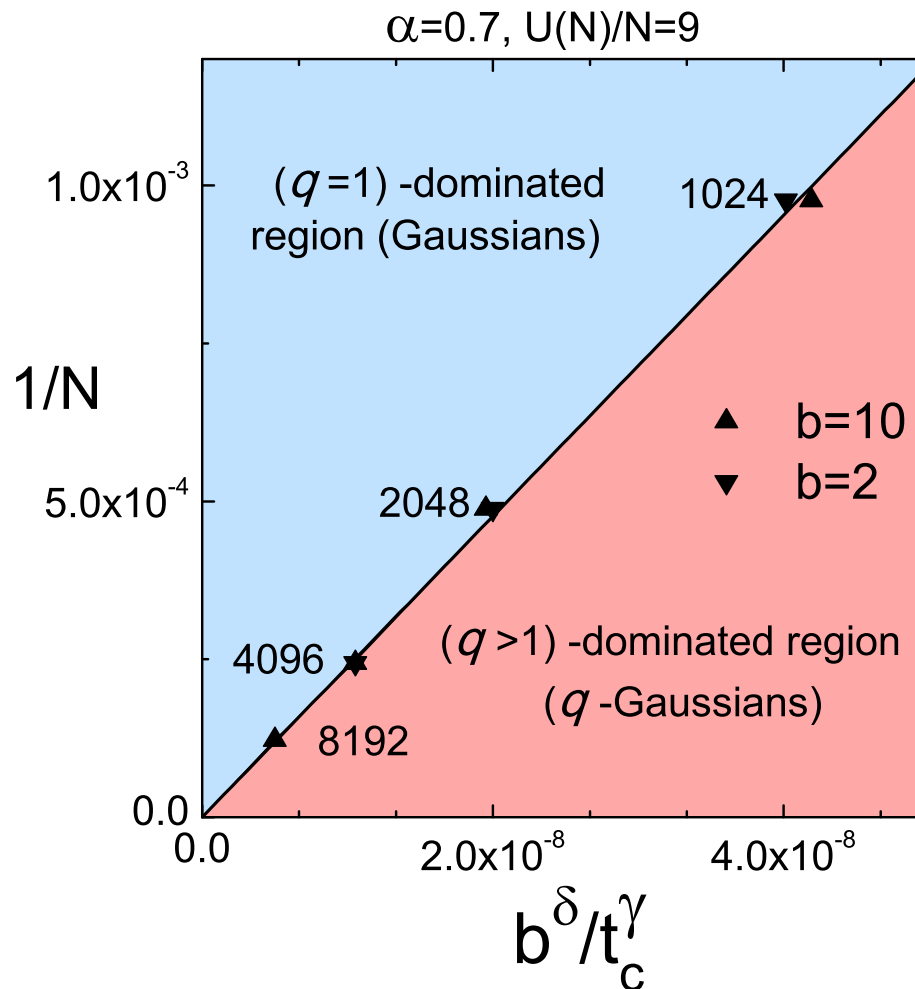
Figure 10: The crossover frontier for $\alpha < 1$ may be plotted by **a single straight line** $1/N = D(\alpha, u)b^\delta/t_c^\gamma$. It divides quasi-stationary states (QSS) that live for long times in "weakly" chaotic (non–uniformly ergodic) subspaces and obey nonextensive statistics, until they eventually enter a domain of "strong" chaos (uniform ergodicity) and BG statistics.

Conclusions

1. In **the subdiffusive case ($E = 0.4$)**, the central particles **initially perform weakly chaotic motion**. On the other hand, **if we study more particles, the motion is more chaotic** since the q index now tends more quickly to 1 at $t = 10^9$. **The expected behavior of the second moment, i.e. $m_2 \propto t^{1/3}$, is well reproduced** by our numerical results.

2. **For the higher energy $E = 1.5$ of the self-trapping case**, the dynamics is somewhat different. **All q entropic indices are now much closer to 1**, even those of the central particles. Here also m_2 **in time as** $t^{1/3}$

3. In the presence of **all to all interactions of the form $1/r^\alpha$**, the **long range case with** $0 < \alpha < 1$ is characterized by **QSS with decaying Lyapunov exponents and q–statistics**. For **the short range $\alpha > 1$ Lyapunov exponents converge to positive values and BG statistics sets in**.

4. There appears to be a **"phase diagram"** separating the two thermostatistics in a $1/N, \propto 1/t^\gamma$ plane, with a **"universal" boundary** for fixed α and energy density. In the $\lim_{N \to \infty} \lim_{t \to \infty}$ **ordering we find BG statistics**, while **in the $\lim_{t \to \infty} \lim_{N \to \infty}$ ordering it is the $q > 1$ statistics that prevails**.

References

1. **Antonopoulos, Ch., Bountis, T., Skokos, Ch. and Drossos, L. [2014]**,"Complex Statistics and Diffusion in Nonlinear Disordered Particle Chains", to appear in special issue of Chaos, ed. by Georg Gottwald.

2. **Christodoulidi, H., Tsallis, C. and Bountis, T. [2014]** "Fermi-Pasta-Ulam model with long-range interactions: Dynamics and thermostatistics", submitted to PRL.

3. **Bountis, T. and Skokos, H. [2012]**, "Complex Hamiltonian Dynamics", Springer Synergetics series, Springer Verlag, Berlin.

4. **Tsallis, C. [2009]**, "Introduction to Nonextensive Statistical Mechanics: Approaching a Complex World", *Springer, New York*.

6. **Anteneodo C. and Tsallis C. [1998]**, "Breakdown of the exponential sensitivity to the initial conditions: Role of the range of the interaction", *Phys. Rev. Lett.* **80**, 5313.

5. **Tsallis, C. [2014]**, "An introduction to nonadditive entropies and a thermostatistical approach to inanimate and living matter", *Contemporary Physics*, published online: 30 April 2014.